



## THE DELPHI DETECTOR AT LEP

DELPHI Collaboration

### ABSTRACT

DELPHI is a  $4\pi$  detector with emphasis on particle identification, three-dimensional information, high granularity and precise vertex determination. The design criteria, the construction of the detector and the performance during the first year of operation at the Large Electron Positron collider (LEP) at CERN are described.

Submitted to Nuclear Instruments and Methods

P.Araucio<sup>11</sup>, H.Abie<sup>24</sup>, P.Abreu<sup>16</sup>, W.Adam<sup>37</sup>, P.Adrianos<sup>3</sup>, T.Adye<sup>27</sup>, G.Akopdzhyanov<sup>31</sup>,  
 G.D.Alekseev<sup>12</sup>, G.Aigostino<sup>33</sup>, J.V.Aitaby<sup>7</sup>, P.Allen<sup>36</sup>, P.Allport<sup>27</sup>, S.Almehed<sup>19</sup>, T.Almeida<sup>16</sup>,  
 S.J.Alvsvaag<sup>4</sup>, U.Amaldi<sup>7</sup>, I.Ambec<sup>35</sup>, A.Amery<sup>17</sup>, E.Anassontzis<sup>3</sup>, P.Antilogus<sup>15</sup>, W.-D.Apel<sup>13</sup>,  
 E.Aria<sup>8</sup>, F.Astesan<sup>18</sup>, C.Aubret<sup>6</sup>, J.-E.Augustin<sup>15</sup>, A.Augustinus<sup>7</sup>, P.Bailion<sup>7</sup>, F.Barao<sup>16</sup>,  
 G.Barbiellini<sup>34</sup>, G.Baricheilo<sup>26</sup>, S.Barlag<sup>15</sup>, J.Barlow<sup>27</sup>, A.Baroncelli<sup>29</sup>, M.Barranco-Luque<sup>7</sup>,  
 G.Barreira<sup>16</sup>, O.Barring<sup>19</sup>, W.Barti<sup>37</sup>, P.Battaiotto<sup>34</sup>, M.Baubillier<sup>18</sup>, C.Baudoin<sup>22</sup>, N.Beadie<sup>27</sup>,  
 K.-H.Becks<sup>39</sup>, W.Bell<sup>7</sup>, P.Beltran<sup>9</sup>, J.M.Beniloch<sup>36</sup>, M.Berggren<sup>32</sup>, S.Berglund<sup>32</sup>, J.-D.Berst<sup>8</sup>,  
 F.Bertolino<sup>33</sup>, S.Biagi<sup>17</sup>, F.Bianchi<sup>33</sup>, J.H.Bibby<sup>25</sup>, N.Bingefors<sup>35</sup>, J.Bjarne<sup>19</sup>, D.Bioch<sup>8</sup>,  
 P.N.Bogolubov<sup>12</sup>, D.Bollini<sup>5</sup>, T.Bolognese<sup>28</sup>, P.Bonierbale<sup>6</sup>, P.S.L.Booth<sup>17</sup>, M.Boratav<sup>18</sup>, P.Borgeand<sup>28</sup>,  
 H.Borner<sup>25</sup>, C.Bosio<sup>29</sup>, O.Botner<sup>35</sup>, B.Bouquet<sup>15</sup>, C.Boutonnet<sup>6</sup>, G.Bovo<sup>26</sup>, M.Bozzo<sup>10</sup>, P.Branchini<sup>29</sup>,  
 C.Brand<sup>7</sup>, K.D.Brand<sup>39</sup>, C.Bricman<sup>2</sup>, R.C.A.Brown<sup>7</sup>, J.-M.Brunet<sup>6</sup>, L.Bugge<sup>24</sup>, T.Buran<sup>24</sup>,  
 H.Burnmeister<sup>7</sup>, C.Buttar<sup>25</sup>, J.A.M.A.Buytaert<sup>2</sup>, G.Cabras<sup>34</sup>, M.Caccia<sup>20</sup>, S.Cairani<sup>7</sup>, M.Calvi<sup>20</sup>,  
 A.J.Camacho Rozas<sup>30</sup>, J.-E.Campagne<sup>7</sup>, A.Campion<sup>17</sup>, T.Camporesi<sup>7</sup>, V.Canale<sup>29</sup>, H.Carling<sup>19</sup>,  
 L.Carroll<sup>17</sup>, C.Caso<sup>10</sup>, E.Castelli<sup>34</sup>, M.V.Castillo Gimenez<sup>36</sup>, F.Cataneo<sup>7</sup>, A.Cattai<sup>7</sup>, F.R.Cavallo<sup>5</sup>,  
 L.Cerrito<sup>29</sup>, G.Chadwick<sup>7</sup>, P.Charpentier<sup>7</sup>, P.Checchia<sup>26</sup>, G.A.Chelkov<sup>12</sup>, L.Chevalier<sup>28</sup>, C.Chiccoli<sup>5</sup>,  
 F.Chignoli<sup>20</sup>, P.Chliapnikov<sup>31</sup>, V.Chorowicz<sup>18</sup>, E.Christophel<sup>8</sup>, R.Cirio<sup>33</sup>, S.Colilli<sup>29</sup>, C.Colledani<sup>8</sup>,  
 F.Conforti<sup>10</sup>, R.Contri<sup>10</sup>, P.A.Cooke<sup>17</sup>, F.Couchot<sup>15</sup>, P.Courty<sup>6</sup>, C.Cozza<sup>26</sup>, H.B.Crawley<sup>1</sup>,  
 D.Crenneli<sup>27</sup>, M.Cresti<sup>26</sup>, M.Croissiaux<sup>8</sup>, G.Crosetti<sup>10</sup>, D.Crosetto<sup>33</sup>, N.Crosland<sup>25</sup>, M.Crozon<sup>6</sup>,  
 J.Cuevas Maestro<sup>30</sup>, L.S.Curwen<sup>17</sup>, S.Czellar<sup>11</sup>, E.Dahl-Jensen<sup>21</sup>, B.Dalmagne<sup>15</sup>, M.Dam<sup>7</sup>, P.Dam<sup>21</sup>,  
 G.Damgaard<sup>21</sup>, G.Darbo<sup>10</sup>, E.Daubie<sup>2</sup>, A.Dauni<sup>13</sup>, M.Davenport<sup>7</sup>, A.De Angelis<sup>34</sup>, M.De Beer<sup>28</sup>,  
 C.De Clercq<sup>2</sup>, N.De Koning<sup>22</sup>, C.De La Vaissiere<sup>18</sup>, F.Defontaines<sup>2</sup>, F.Degli Esposti<sup>5</sup>, D.Delikaris<sup>7</sup>,  
 P.Delpierre<sup>6</sup>, Y.N.Denisov<sup>12</sup>, L.Di Ciaccio<sup>29</sup>, S.Di Pietro<sup>7</sup>, A.Diaczek<sup>6</sup>, A.N.Diddens<sup>22</sup>, H.Dijkstra<sup>7</sup>,  
 N.Dimitriou<sup>9</sup>, J.Dolbeau<sup>6</sup>, M.Donszelmann<sup>22</sup>, K.Doroba<sup>38</sup>, R.Downs<sup>27</sup>, M.Dracos<sup>8</sup>, J.Drees<sup>39</sup>,  
 M.Dris<sup>23</sup>, S.Du<sup>15</sup>, N.Dudragne<sup>7</sup>, W.Dulinski<sup>8</sup>, R.Dzhelyadin<sup>31</sup>, L.-O.Eek<sup>35</sup>, P.A.-M.Eerola<sup>11</sup>,  
 K.Eilertsen<sup>24</sup>, T.Ekelot<sup>35</sup>, M.Ellila<sup>11</sup>, J.-P.Engel<sup>8</sup>, L.Etienne<sup>2</sup>, G.J.Evers<sup>22</sup>, R.Every<sup>25</sup>, V.Falaleev<sup>31</sup>,  
 A.Fenyuk<sup>31</sup>, M.Fernandez Aionso<sup>30</sup>, A.Ferrer<sup>36</sup>, I.Ferrer<sup>36</sup>, S.Ferroni<sup>10</sup>, B.Fialovski<sup>12</sup>, T.A.Filippas<sup>23</sup>,  
 A.Firestone<sup>1</sup>, H.G.Fischer<sup>7</sup>, R.Fischer<sup>8</sup>, B.Fjeld<sup>24</sup>, M.Flinn<sup>35</sup>, G.Floom<sup>32</sup>, H.Foeth<sup>7</sup>, E.Fokitis<sup>23</sup>,  
 P.Folegati<sup>19</sup>, F.Fontanelli<sup>10</sup>, H.Forsbach<sup>39</sup>, D.Fraissard<sup>7</sup>, B.Franek<sup>27</sup>, K.E.Fransson<sup>35</sup>, F.Fratnik<sup>34</sup>,  
 D.C.Fries<sup>13</sup>, J.-P.Froberger<sup>8</sup>, A.G.Frodesen<sup>4</sup>, R.Fruhworth<sup>37</sup>, F.Fulda-Quenzer<sup>15</sup>, J.Fuster<sup>7</sup>, J.M.Gago<sup>16</sup>,  
 M.Gaillard<sup>15</sup>, G.Galeazzi<sup>26</sup>, D.Gamba<sup>33</sup>, C.Garat<sup>18</sup>, J.Garcia<sup>30</sup>, C.Gaspar<sup>7</sup>, U.Gasparini<sup>26</sup>, P.Gavillet<sup>7</sup>,  
 S.Gawne<sup>17</sup>, E.N.Gazis<sup>23</sup>, J.-F.Genat<sup>18</sup>, L.Gerdyukov<sup>31</sup>, V.Giordano<sup>5</sup>, K.-W.Glitza<sup>39</sup>, R.Gokiel<sup>18</sup>,  
 V.M.Golovatyuk<sup>12</sup>, P.Gomes<sup>16</sup>, A.Goobar<sup>32</sup>, R.Goorens<sup>2</sup>, G.Gopal<sup>27</sup>, M.Gorbics<sup>1</sup>, B.Goret<sup>7</sup>,  
 M.Gorski<sup>38</sup>, G.Goujon<sup>28</sup>, V.Gracco<sup>10</sup>, A.Grant<sup>7</sup>, F.Giard<sup>2</sup>, E.Graziani<sup>29</sup>, G.Greggio<sup>26</sup>, J.-P.Grillet<sup>7</sup>,  
 M.-H.Gros<sup>15</sup>, M.Gros<sup>38</sup>, G.Grosdidier<sup>15</sup>, B.Grossetete<sup>18</sup>, B.Grung<sup>4</sup>, L.Guglielmi<sup>6</sup>, J.Guy<sup>27</sup>, Z.Guzik<sup>12</sup>,  
 E.Gygi<sup>7</sup>, F.Hahn<sup>39</sup>, M.Hahn<sup>13</sup>, S.Haider<sup>7</sup>, J.Haissinski<sup>15</sup>, Z.Hajduk<sup>22</sup>, A.Hakansson<sup>19</sup>, A.Hallgren<sup>35</sup>,  
 K.Hamacher<sup>39</sup>, G.Hamei De Monchenault<sup>28</sup>, F.J.Harris<sup>25</sup>, F.Hartjes<sup>22</sup>, B.Heck<sup>7</sup>, K.Hellberg<sup>11</sup>,  
 I.Herbst<sup>39</sup>, H.Herr<sup>7</sup>, E.Higon<sup>36</sup>, H.J.Hilke<sup>7</sup>, H.Hofmann<sup>7</sup>, T.Hofnoki<sup>38</sup>, R.Holm<sup>24</sup>, R.Holmes<sup>1</sup>,  
 S.-O.Holmgren<sup>32</sup>, J.Homer<sup>1</sup>, J.E.Hooper<sup>21</sup>, R.Horisberger<sup>7</sup>, M.Houlden<sup>17</sup>, A.Hrisoho<sup>15</sup>, J.Hrubec<sup>37</sup>,  
 L.Hubbeling<sup>7</sup>, K.Huitu<sup>11</sup>, K.Hultqvist<sup>32</sup>, D.Husson<sup>8</sup>, B.D.Hyams<sup>7</sup>, C.Illinger<sup>8</sup>, D.Imbault<sup>18</sup>,  
 P.Ioannou<sup>3</sup>, P.-S.Iversen<sup>4</sup>, J.N.Jackson<sup>17</sup>, F.Jacob<sup>27</sup>, J.-J.Jaeger<sup>6</sup>, P.Jalocka<sup>14</sup>, W.Janczur<sup>14</sup>,  
 H.Jansen<sup>22</sup>, G.Jarlskog<sup>19</sup>, P.Jarry<sup>28</sup>, B.Jean-Marie<sup>15</sup>, J.Joensuu<sup>11</sup>, E.K.Johansson<sup>32</sup>, H.Johansson<sup>35</sup>,  
 M.Jonker<sup>7</sup>, P.Juillot<sup>8</sup>, R.B.Kadyrov<sup>121</sup>, S.Kaeck<sup>19</sup>, M.Kajetanowicz<sup>14</sup>, G.Kalkanis<sup>3</sup>, G.Kalmus<sup>27</sup>,  
 G.Kantardjian<sup>7</sup>, P.Kapusta<sup>14</sup>, S.Katsanevas<sup>3</sup>, E.C.Katsoufis<sup>23</sup>, R.Keranen<sup>11</sup>, S.Kersten<sup>39</sup>,  
 J.Kesteman<sup>2</sup>, B.A.Khomenko<sup>12</sup>, N.N.Khovansky<sup>12</sup>, P.Kindblom<sup>35</sup>, B.King<sup>17</sup>, B.Kisielewski<sup>14</sup>,  
 W.Klempt<sup>7</sup>, A.Klovning<sup>4</sup>, B.Koene<sup>22</sup>, J.Kok<sup>22</sup>, P.Kokkinias<sup>9</sup>, I.Kontaxis<sup>3</sup>, M.Kopf<sup>13</sup>, J.Koponen<sup>11</sup>,  
 K.Korcyi<sup>14</sup>, Y.Kornelis<sup>7</sup>, A.Korporaal<sup>22</sup>, A.V.Korytov<sup>12</sup>, P.Kostarakis<sup>9</sup>, C.Kourkoumelis<sup>3</sup>,  
 T.Kreuzberger<sup>37</sup>, J.Krolikowski<sup>38</sup>, W.Kucewicz<sup>20</sup>, G.Kuhn<sup>7</sup>, P.Kulinich<sup>12</sup>, K.Kulka<sup>19</sup>, K.Kurvinen<sup>11</sup>,  
 M.I.Laakso<sup>11</sup>, C.Lambropoulos<sup>9</sup>, J.W.Lamsa<sup>1</sup>, L.Lanceri<sup>34</sup>, D.Langerveld<sup>22</sup>, V.Lapin<sup>31</sup>, J.-P.Laugier<sup>28</sup>,  
 R.Lauhakangas<sup>11</sup>, G.Laurenti<sup>5</sup>, P.Laurikainen<sup>11</sup>, B.Lavigne<sup>15</sup>, J.-C.Le Grand<sup>7</sup>, H.Lebbo<sup>18</sup>, G.Leder<sup>37</sup>,  
 J.Lemonne<sup>2</sup>, G.Lenzen<sup>39</sup>, R.Leoni<sup>20</sup>, V.Lepeltier<sup>15</sup>, M.Lewandowski<sup>38</sup>, J.A.Lidbury<sup>27</sup>, E.Lillestol<sup>17</sup>,  
 E.Lillethun<sup>4</sup>, L.-E.Lindqvist<sup>35</sup>, I.Lippi<sup>26</sup>, M.Lokajicek<sup>12</sup>, J.G.Loken<sup>25</sup>, R.Lomoro<sup>29</sup>,  
 M.A.Lopez Aguera<sup>30</sup>, P.Lorenz<sup>39</sup>, D.Loukas<sup>9</sup>, R.Lucocock<sup>27</sup>, B.Lund-Jensen<sup>35</sup>, B.Lundberg<sup>19</sup>, L.Lyons<sup>25</sup>,  
 G.Maehlum<sup>7</sup>, O.Maeland<sup>4</sup>, C.Maillet<sup>28</sup>, S.Maltezos<sup>23</sup>, F.Mandi<sup>37</sup>, J.Marco<sup>30</sup>, A.Markou<sup>9</sup>, I.Martinez<sup>30</sup>,  
 J.Mas<sup>6</sup>, L.Mathis<sup>6</sup>, C.Matteuzzi<sup>20</sup>, G.Matthiae<sup>29</sup>, L.Mattsson<sup>35</sup>, E.A.Matyushevski<sup>12</sup>, N.Mayet<sup>8</sup>,  
 R.Mazza<sup>20</sup>, M.Mazzucato<sup>26</sup>, M.Mc Cubbin<sup>17</sup>, R.Mc Kay<sup>1</sup>, E.Menichetti<sup>33</sup>, C.Meroni<sup>20</sup>, W.T.Meyer<sup>1</sup>,  
 J.Michalowski<sup>14</sup>, H.-H.Mielke<sup>13</sup>, W.A.Mitaroff<sup>37</sup>, G.V.Mitselmakher<sup>12</sup>, U.Mjoernmark<sup>19</sup>, R.Moeller<sup>21</sup>,

<sup>1</sup>deceased

K.Moenig<sup>39</sup>, G.Molinari<sup>5</sup>, M.R.Monge<sup>10</sup>, F.Montano<sup>10</sup>, A.Morelli<sup>10</sup>, P.Morettini<sup>10</sup>, P.G.Moyssides<sup>9</sup>,  
 H.Mueller<sup>13</sup>, H.Muller<sup>7</sup>, M.Mur<sup>28</sup>, G.Myatt<sup>25</sup>, F.L.Navarria<sup>5</sup>, A.Nawrot<sup>38</sup>, P.Negri<sup>20</sup>, B.S.Nielsen<sup>21</sup>,  
 M.Nigro<sup>26</sup>, M.Nonni<sup>29</sup>, J-M.Noppe<sup>15</sup>, M.Nordberg<sup>11</sup>, S.Nounos<sup>3</sup>, V.Obraztsov<sup>31</sup>, T.Odegaard<sup>24</sup>,  
 A.Olchevski<sup>12</sup>, M.Oppermann<sup>39</sup>, R.Orava<sup>11</sup>, E.Orme<sup>17</sup>, R.Oswald<sup>8</sup>, A.Ouraou<sup>28</sup>, G.Paccagnella<sup>26</sup>,  
 J.Pagot<sup>15</sup>, R.Pain<sup>18</sup>, K.Pakonski<sup>14</sup>, L.Palermo<sup>16</sup>, S.Palermo<sup>16</sup>, S.Palma Lopes<sup>18</sup>, T.Papadopoulou<sup>23</sup>,  
 L.Pape<sup>7</sup>, P.Pasini<sup>5</sup>, J.Passeneau<sup>18</sup>, M.Passeneau<sup>18</sup>, A.Passeri<sup>29</sup>, J.B.Pattison<sup>7</sup>, B.Paul<sup>28</sup>, M.Pegoraro<sup>26</sup>,  
 J.Perez<sup>7</sup>, M.Pernicka<sup>37</sup>, G.Petrucci<sup>7</sup>, T.Pettersen<sup>4</sup>, M.Pimenta<sup>16</sup>, O.Pingot<sup>2</sup>, C.Pinori<sup>26</sup>, A.Pinsent<sup>25</sup>,  
 O.Piovan<sup>26</sup>, C.Poiet<sup>2</sup>, M.E.Pol<sup>16</sup>, B.Poliakov<sup>31</sup>, G.Polok<sup>14</sup>, P.Poropat<sup>34</sup>, D.Poutot<sup>6</sup>, P.Privitera<sup>5</sup>,  
 A.Pullia<sup>20</sup>, J.Pyyhtia<sup>11</sup>, P.Queru<sup>7</sup>, S.Quinton<sup>27</sup>, D.Radojicic<sup>25</sup>, S.Ragazzi<sup>20</sup>, R.Ragazzon<sup>34</sup>,  
 G.Rampazzo<sup>26</sup>, G.Ranelli<sup>29</sup>, W.H.Range<sup>17</sup>, J-C.Raoul<sup>28</sup>, P.N.Ratoff<sup>25</sup>, A.L.Read<sup>24</sup>, N.G.Redaeli<sup>20</sup>,  
 M.Regler<sup>37</sup>, D.Reid<sup>17</sup>, M.V.Reis<sup>16</sup>, P.B.Renton<sup>25</sup>, L.K.Resvanis<sup>3</sup>, P.Rewiersma<sup>22</sup>, V.Riadovikov<sup>31</sup>,  
 F.Richard<sup>15</sup>, J.Ridky<sup>12</sup>, G.Rinaudo<sup>33</sup>, I.Roditi<sup>7</sup>, A.M.Romaya<sup>25</sup>, A.Romero<sup>33</sup>, P.Ronchese<sup>26</sup>,  
 R.Rongved<sup>4</sup>, E.I.Rosenberg<sup>1</sup>, F.Rossel<sup>18</sup>, S.Rossi<sup>20</sup>, E.Rosso<sup>7</sup>, P.Roudeau<sup>15</sup>, T.Rovelli<sup>5</sup>, V.Ruhlmann<sup>28</sup>,  
 A.Ruiz<sup>30</sup>, V.I.Ryabtsov<sup>121</sup>, J.Rypko<sup>15</sup>, V.N.Ryzhov<sup>12</sup>, H.Saarikko<sup>11</sup>, D.Sacco<sup>29</sup>, Y.Sacquin<sup>28</sup>,  
 A.B.Sadovsky<sup>12</sup>, G.Saget<sup>6</sup>, J.Salt<sup>36</sup>, E.Sanchez<sup>36</sup>, E.Sanchis<sup>36</sup>, M.Sannino<sup>10</sup>, B.Sanny<sup>39</sup>, E.Saragas<sup>9</sup>,  
 M.Schaeffer<sup>8</sup>, F.Schneider<sup>71</sup>, H.Schneider<sup>13</sup>, F.Scuri<sup>34</sup>, A.Sebastia<sup>36</sup>, Y.V.Sedykh<sup>12</sup>, A.M.Segar<sup>25</sup>,  
 R.Sekulin<sup>27</sup>, P.Seller<sup>27</sup>, M.Sessa<sup>34</sup>, G.Sette<sup>10</sup>, R.Seufert<sup>13</sup>, P.Siegrist<sup>28</sup>, C.Silva<sup>16</sup>, E.Silvestre<sup>36</sup>,  
 S.Simonetti<sup>10</sup>, F.Simonetto<sup>26</sup>, T.B.Skaali<sup>24</sup>, J.Skeens<sup>1</sup>, G.Smadja<sup>28</sup>, G.R.Smith<sup>27</sup>, N.A.Smith<sup>17</sup>,  
 A.Sokos<sup>9</sup>, R.Sosnowski<sup>38</sup>, K.Spang<sup>21</sup>, T.S.Spassoff<sup>12</sup>, M.Spedini<sup>33</sup>, P.Spentzouris<sup>3</sup>, E.Spiriti<sup>29</sup>,  
 S.Squarcia<sup>10</sup>, C.Stanescu<sup>29</sup>, G.Stavropoulos<sup>9</sup>, R.Stevens<sup>25</sup>, F.Stichelbaut<sup>2</sup>, A.Stocchi<sup>20</sup>, J.Strauss<sup>37</sup>,  
 S.Strom<sup>24</sup>, E.Sundell<sup>11</sup>, M.Szczekowski<sup>38</sup>, M.Szeptycka<sup>38</sup>, P.Szymanski<sup>38</sup>, J.Tarjan<sup>12</sup>, S.Tavernier<sup>2</sup>,  
 J.Thadome<sup>39</sup>, G.Theodosiou<sup>9</sup>, L.Thollander<sup>32</sup>, W.D.Thomas<sup>1</sup>, J.Thornhill<sup>17</sup>, P.Thorsteinsen<sup>24</sup>,  
 A.Tilquin<sup>6</sup>, J.Timmermans<sup>22</sup>, V.G.Timofeev<sup>12</sup>, L.G.Tkatchev<sup>12</sup>, T.Todorov<sup>12</sup>, D.Z.Toet<sup>22</sup>,  
 V.Tokmenin<sup>12</sup>, S.Topp-Jorgensen<sup>25</sup>, A.K.Toppol<sup>4</sup>, L.Tortora<sup>29</sup>, P.Trapani<sup>33</sup>, L.Traspedini<sup>10</sup>,  
 D.Treille<sup>7</sup>, U.Trevisan<sup>10</sup>, G.Tripodi<sup>10</sup>, G.Tristram<sup>6</sup>, C.Troncon<sup>20</sup>, T.K.Truong<sup>15</sup>, E.N.Tsyganov<sup>12</sup>,  
 M.Turala<sup>14</sup>, R.Turchetta<sup>8</sup>, J-P.Turlot<sup>6</sup>, M-L.Turluer<sup>28</sup>, P.Turner<sup>17</sup>, T.Tuuva<sup>11</sup>, I.A.Tyapkin<sup>12</sup>,  
 M.Tyndel<sup>27</sup>, F.Udo<sup>22</sup>, O.Ullaland<sup>7</sup>, G.Valenti<sup>5</sup>, G.W.Van Apeldoorn<sup>22</sup>, G.Van Beek<sup>2</sup>, P.Van Dam<sup>22</sup>,  
 W.K.Van Doninck<sup>2</sup>, B.Van Eijk<sup>7</sup>, N.Van Eijndhoven<sup>7</sup>, L.Van Lancker<sup>2</sup>, C.Vander Velde<sup>2</sup>,  
 J-P.Vanuxem<sup>7</sup>, J.Varela<sup>16</sup>, A.T.Vasilenko<sup>12</sup>, P.Vaz<sup>16</sup>, C.Veccia<sup>10</sup>, G.Vegni<sup>20</sup>, T.Vehvilainen<sup>11</sup>,  
 M.E.Veitch<sup>25</sup>, J.Velasco<sup>36</sup>, P.Veneroni<sup>29</sup>, L.Ventura<sup>26</sup>, W.Venus<sup>27</sup>, P.Vergezac<sup>6</sup>, J.Vergne<sup>6</sup>,  
 F.Vernocchi<sup>10</sup>, L.S.Vertogradov<sup>12</sup>, D.Vilanova<sup>28</sup>, H.Vink<sup>22</sup>, L.Visen Melo<sup>16</sup>, A.S.Vodopyanov<sup>12</sup>,  
 M.Vollmer<sup>39</sup>, G.Voulgaris<sup>3</sup>, M.Voutilainen<sup>11</sup>, V.Vrba<sup>12</sup>, H.Wahlen<sup>39</sup>, F.Waldner<sup>34</sup>, M.Wayne<sup>1</sup>,  
 P.Weilhammer<sup>7</sup>, C.Werner<sup>16</sup>, J.Werner<sup>39</sup>, A.M.Wetherell<sup>7</sup>, J.H.Wickens<sup>2</sup>, J.Wikne<sup>24</sup>, E.Wilhelmsen<sup>24</sup>,  
 L.Wilkinson<sup>17</sup>, M.T.Williams<sup>25</sup>, W.S.C.Williams<sup>25</sup>, B-H.Witt<sup>39</sup>, D.Wormald<sup>24</sup>, G.Wormser<sup>15</sup>,  
 K.Woschnagg<sup>35</sup>, S.Xyroustikos<sup>9</sup>, N.Yamdagni<sup>32</sup>, J.Yelton<sup>25</sup>, A.Zaitsev<sup>31</sup>, A.Zalewska<sup>14</sup>, P.Zalewski<sup>38</sup>,  
 P.I.Zarubin<sup>12</sup>, E.Zevgolatakos<sup>9</sup>, N.I.Zimin<sup>12</sup>, A.I.Zinchenko<sup>12</sup>, M.Zito<sup>10</sup>, R.Zitoun<sup>18</sup>, E.Zonca<sup>28</sup>,  
 A.Zotov<sup>31</sup>, A.Zucchini<sup>5</sup>, G.Zumerle<sup>26</sup>

- <sup>1</sup> Ames Laboratory and Department of Physics, Iowa State University, Ames IA 50011, USA
- <sup>2</sup> Physics Department, Univ. Instelling Antwerpen, Universiteitsplein 1, B-2610 Wilrijk, Belgium  
and IIHE, ULB-VUB, Pleinlaan 2, B-1050 Brussels, Belgium  
and Service de Phys. des Part. Elém., Faculté des Sciences, Université de l'Etat Mons, Av. Maistriau 19, B-7000 Mons, Belgium
- <sup>3</sup> Physics Laboratory, University of Athens, Solonos Str. 104, GR-10680 Athens, Greece
- <sup>4</sup> Department of Physics, University of Bergen, Allégaten 55, N-5007 Bergen, Norway
- <sup>5</sup> Dipartimento di Fisica, Università di Bologna and INFN, Via Irnerio 46, I-40126 Bologna, Italy
- <sup>6</sup> Collège de France, Lab. de Physique Corpusculaire, 11 pl. M. Berthelot, F-75231 Paris Cedex 05, France
- <sup>7</sup> CERN, CH-1211 Geneva 23, Switzerland
- <sup>8</sup> Division des Hautes Energies, CRN - Groupe DELPHI and LEPSE, B.P.20 CRO, F-67037 Strasbourg Cedex, France
- <sup>9</sup> Greek Atomic Energy Commission, Nucl. Research Centre Demokritos, P.O. Box 60228, GR-15310 Aghia Paraskevi, Greece
- <sup>10</sup> Dipartimento di Fisica, Università di Genova and INFN, Via Dodecaneso 33, I-16146 Genova, Italy
- <sup>11</sup> Dept. of High Energy Physics, University of Helsinki, Siltavuorenpenger 20 C, SF-00170 Helsinki 17, Finland
- <sup>12</sup> Joint Institute for Nuclear Research, Dubna, Head Post Office, P.O. Box 79, 101 000 Moscow, USSR.
- <sup>13</sup> Institut für Experimentelle Kernphysik, Universität Karlsruhe, Postfach 6980, D-7500 Karlsruhe 1, FRG
- <sup>14</sup> High Energy Physics Laboratory, Institute of Nuclear Physics, Ul. Kawioro 26 a, PL-30065 Krakow 30, Poland
- <sup>15</sup> Université de Paris-Sud, Lab. de l'Accélérateur Linéaire, Bat 200, F-91405 Orsay, France
- <sup>16</sup> LIP, Av. Elias Garcia 14 - 1e, P-1000 Lisbon Codex, Portugal
- <sup>17</sup> Department of Physics, University of Liverpool, P.O. Box 147, GB - Liverpool L69 3BX, UK
- <sup>18</sup> LPNHE, Universités Paris VI et VII, Tour 33 (RdC), 4 place Jussieu, F-75230 Paris Cedex 05, France
- <sup>19</sup> Department of Physics, University of Lund, Sölvegatan 14, S-22363 Lund, Sweden
- <sup>20</sup> Dipartimento di Fisica, Università di Milano and INFN, Via Celoria 16, I-20133 Milan, Italy
- <sup>21</sup> Niels Bohr Institute, Blegdamsvej 17, DK-2100 Copenhagen Ø, Denmark
- <sup>22</sup> NIKHEF-H, Postbus 41882, NL-1009 DB Amsterdam, The Netherlands
- <sup>23</sup> National Technical University, Physics Department, Zografou Campus, GR-15773 Athens, Greece
- <sup>24</sup> Physics Department, University of Oslo, Blindern, N-1000 Oslo 3, Norway
- <sup>25</sup> Nuclear Physics Laboratory, University of Oxford, Keble Road, GB - Oxford OX1 3RH, UK
- <sup>26</sup> Dipartimento di Fisica, Università di Padova and INFN, Via Marzolo 8, I-35131 Padua, Italy
- <sup>27</sup> Rutherford Appleton Laboratory, Chilton, GB - Didcot OX11 0QX, UK
- <sup>28</sup> CEN-Saclay, DPhPE, F-91191 Gif-sur-Yvette Cedex, France
- <sup>29</sup> Istituto Superiore di Sanità, Ist. Naz. di Fisica Nucl. (INFN), Viale Regina Elena 299, I-00161 Rome, Italy  
and Dipartimento di Fisica, Università di Roma II and INFN, Tor Vergata, I-00173 Rome.
- <sup>30</sup> Facultad de Ciencias, Universidad de Santander, av. de los Castros, E - 39005 Santander, Spain
- <sup>31</sup> Inst. for High Energy Physics, Serpukov P.O. Box 35, Protvino, (Moscow Region), USSR.
- <sup>32</sup> Institute of Physics, University of Stockholm, Vanadisvägen 9, S-113 46 Stockholm, Sweden
- <sup>33</sup> Dipartimento di Fisica Sperimentale, Università di Torino and INFN, Via P. Giuria 1, I-10126 Turin, Italy
- <sup>34</sup> Dipartimento di Fisica, Università di Trieste and INFN, Via A. Valerio 2, I-34127 Trieste, Italy  
and Istituto di Fisica, Università di Udine, I-33100 Udine, Italy
- <sup>35</sup> Department of Radiation Sciences, University of Uppsala, P.O. Box 535, S-751 21 Uppsala, Sweden
- <sup>36</sup> Inst. de Fisica Corpuscular IFIC, Centro Mixto Univ. de Valencia-CSIC, Avda. Dr. Moliner 50, E-46100 Burjassot (Valencia), Spain
- <sup>37</sup> Institut für Hochenergiephysik, Österreich Akad. d. Wissensch., Nikolsdorfergasse 18, A-1050 Vienna, Austria
- <sup>38</sup> Inst. Nuclear Studies and, University of Warsaw, Ul. Hoza 69, PL-00681 Warsaw, Poland
- <sup>39</sup> Fachbereich Physik, University of Wuppertal, Postfach 100 127, D-5600 Wuppertal 1, FRG

## 1. INTRODUCTION

DELPHI, a DEtector with Lepton, Photon and Hadron Identification, is a detector operating at LEP (Large Electron and Positron collider) at CERN. It is designed as a general purpose detector with special emphasis on powerful particle identification, even in complex events; Ring Imaging CHerenkov counters (RICHes), three-dimensional information with high granularity in most of its components and precise vertex determination are its specific attributes [1].

This report describes the construction of the detector, the performance during the first 8 months of operation at LEP and a few test beam results of final components. All detectors are complete and fully operational, except the RICHes and the tracking detector for the Luminosity Monitor. For the Barrel-RICH, half the drift-tubes and liquid radiators have operated so far. First signals have also been observed from a provisional gas radiator. Fig. 1 shows a few examples of event displays obtained.

In the following description of the detector we shall use a coordinate system with the  $z$ -axis parallel to the beam, radius  $R$  and azimuth  $\phi$  in the plane perpendicular to it and polar angle  $\theta$  ( $= 0$  along  $z$ ).

## 2. GENERAL LAYOUT

DELPHI is installed in a cavern 100 m below ground. The general layout is shown in Fig. 2. The ensemble consists of a cylindrical section, the barrel, and two end-caps, which can be axially opened by 2.8 m to allow rapid access to the various detectors. When the end-caps are closed, mobile shielding around the beam pipe follows this movement, thus allowing access during beam operation anywhere outside the detector, which is self-shielding. Three-to-four-storey huts on both sides house the electronics, the 14 computers for the subdetectors, gas distributions and the cryogenics and power supplies for the superconducting magnet. The barrel and each end-cap can be moved sideways independently, together with their huts, to give free access for installation of major components. An optical data link sends the compressed data to the main computer and control centre located on the surface.

Fig. 3 shows details of the detector arrangement.

## 3. SOLENOID

The superconducting solenoid [2] has a length of 7.4 m and an inner diameter of 5.2 m (dimensions of the cryostat). The field of 1.2 T is produced by a single conductor layer (5000 A) with two 35 cm long end sections containing a second layer to improve field homogeneity. The superconducting cable is made from 17 twisted wires (700 microns  $\varnothing$ ) clad in high purity aluminium and forming a flat conductor ( $4.5 \times 24 \text{ mm}^2$ ). The wires themselves contain 300 Nb-Ti filaments (25 microns  $\varnothing$ ) embedded in a copper matrix. The cable is insulated by 2-stage pre-preg and wound from the inside onto the aluminium support cylinder, which is cooled from the outside by forced flow of liquid helium at 4.5°K. Normal operation requires a liquification rate of 0.85 g/s and 150 W of cooling at 4.5°K (including losses in the transfer lines and in the intermediate dewar) and 900 W at 65°K in the thermal shield.

The excellent field homogeneity required for the long-drift detectors was obtained after optimization of the currents in the short end layers, as shown in Fig. 4. Inside the Time Projection Chamber, the longitudinal component lies well within 12334 G  $\pm 10$  G (indicating a weak axial asymmetry) with negligible azimuthal variation; the radial component is  $< 5$  G.

The solenoid system is controlled using three G64 systems with higher level control from a MicroVAX. The VAX also provides data logging with a long-term memory and graphical display of solenoid parameters.

#### 4. BEAM PIPE

The aluminium beam pipe has a smooth central section, 32 cm long, an inner diameter of 158.4 mm and 1.2 mm wall thickness. It is supported by 3 wires at  $\pm 1.47$  m on the TPC and at  $\pm 3$  m behind two bellows, a pump and a valve by the superconducting quadrupoles. The internal pipe diameter of 156 mm was chosen to avoid all synchrotron radiation photons except those backscattered twice, according to conservative beam shape calculations.

After the first experience with LEP and beam envelope and background measurements it is clear that a smaller beam diameter is possible. A second generation pipe with internal diameter = 106 mm is being constructed, with a central beryllium section 1.4 mm thick and 570 mm long, followed by a carbon fibre tube 1 mm thick with 0.1 mm Al cladding on the inside. Installation of this pipe is scheduled for the end of 1990.

#### 5. TRACKING DETECTORS

A summary of the principal parameters and the performance of the tracking detectors is given in Table 1. Combined tracking performance is discussed in sect. 5.10.

##### 5.1 Vertex detector (VTX)

Two concentric shells of Si-strip detectors at average radii of 9 and 11 cm cover the central region over a length of 24.0 cm. The principle objective of this detector is to provide maximum  $R\phi$ -resolution, in particular for the study of heavy flavour physics: 5  $\mu\text{m}$  single track resolution and  $\leq 100$   $\mu\text{m}$  double track separation [3(a)].

Each shell consists of 24 modules with about 10% overlap in  $\phi$  between the modules (Fig. 5(a)). Each module carries 4 detectors along  $z$ , with strips parallel to the beam and detector pairs wire-bonded in series and read out at the ends. The Si-detectors are 300  $\mu\text{m}$  thick and have a diode pitch of 25  $\mu\text{m}$ (\*). A new feature is that the read-out strips (50  $\mu\text{m}$  pitch) are AC coupled over the whole length through 0.2  $\mu\text{m}$  of  $\text{SiO}_2$ . The diodes are biased using polysilicon resistors (5  $\text{M}\Omega$ ). Each detector has a sensitive length of

---

(\*) From SI, Oslo.

59 mm and a width of 25.6 mm (for 512 read-out channels) or 32 mm (640 channels) for the inner and outer shell, respectively. The number of read-out strips totals 54254.

The VLSI readout electronics ("M X 3",  $6 \times 6 \text{ mm}^2$ )<sup>(\*)</sup>, produced in  $3 \mu\text{m}$  C-MOS, contain 128 analog channels with serial read-out (power dissipation = 60 mW/chip). The outputs of nine chips are multiplexed together in electronics mounted nearby, giving 1152 channels per readout line. The measured preamplifier noise is  $\text{ENC} = 700 \text{ e}$  without load and 1500 e when connected to two strips in series (i.e. 12 cm long).

The detectors and preamps are mounted with carbon-fibre supports to aluminium rings at the outer ends. The mechanical structure is water cooled to guarantee good thermal stability. The two shells have a total thickness of only 1.1% of a radiation length. Fig. 5(b) shows a blow-up of the connection of detector and read-out chips. The whole detector can be slid into position in-situ on rails fixed to the Inner Detector. The lasers and the SAT Tracker have to be dismantled for this operation.

Relative alignment of the modules was surveyed before installation with an accuracy of about  $10 \mu\text{m}$  in 3D<sup>(\*\*)</sup>. Movements relative to the Inner Drift Chamber are monitored by light spots focussed to 12 of the outer modules and by 18 capacitive displacement probes [3(b)]. Sensitivity of the monitoring is  $\sim 10 \mu\text{m}$  in R and  $< 5 \mu\text{m}$  in  $\phi$  for the light spots and  $< 1 \mu\text{m}$  in R and  $\sim 6 \mu\text{m}$  in  $\phi$  for the capacitive probes [3(b)]. Stability at LEP is found to be  $< 1 \mu\text{m}$  radially over 10 days (Fig. 7(a)).

Laboratory measurements gave a signal/noise ratio of 15/1 for a m.i.p. The same performance is measured at LEP. Fig. 6 shows a partial online event display with information from the VTX, the IDC and the TPC. From tracks passing through the overlap region and producing 4 hits, a preliminary value of  $7 \mu\text{m}$  was obtained for the azimuthal resolution (Fig. 7(b)). Internal alignment with tracks from  $Z^0$  events has so far reached an accuracy of  $\sigma_{R\phi} = 14 \mu\text{m}$  for the full Vertex Detector, resulting in a vertex reconstruction error of  $90 \mu\text{m}$  in (x,y).

For the smaller diameter beam pipe, it is planned to install an innermost third layer of similar design, but 21 cm long to cover polar angles  $\geq 30^\circ$ . This will later be upgraded by adding layers with strips on both inner and outer surfaces to obtain z-information. First tests of such detectors have given  $16 \mu\text{m}$  resolution on the n-side.

## 5.2 Inner Detector (ID)

The ID [4] provides high redundancy for vertex reconstruction and trigger information. It consists of 2 concentric layers:

- an inner drift chamber with jet-chamber geometry, giving 24  $R\phi$ -points per track and

---

(\*) From Mielec, Belgium.

(\*\*) Poli-Varallo Sesia, Italy.

- 5 cylindrical MWPC layers, each layer with 192 wires and 192 circular cathode strips with about 5 mm pitch, proportional to R. The wires provide fast trigger information and resolve left/right ambiguities from the jet section. The strips give z information, also for the trigger.

The jet-chamber section has 24 azimuthal sectors. The wire layout of a 90 degree section is shown in Fig. 8(a). The gas ( $\text{CO}_2/\text{C}_4\text{H}_{10}/\text{C}_3\text{H}_7\text{OH}$ : 94.85/4.5/ 0.65%), field wire grids on both sides of the sense wire planes and operating point (drift field varying from 1 to 2 kV/cm) were chosen to produce a drift velocity proportional to R. Thus, the trigger information for radial tracks is always contained in a narrow time-window ( $\sim 100$  ns). Six laser beams – used in conjunction with the TPC – provide monitoring of drift properties.

In the five outer layers, sense wires are spaced about 8 mm apart and interleaved with field wires. Each layer is 8 mm deep and has circular cathode strips with multilayer transmission lines on the inner wall. The gas used is Ar/ $\text{CO}_2$  (70/30%).

The chamber walls are built from aramide-fibre/epoxy laminates chosen for its high mechanical strength and low thermal expansion. Radiation thickness at  $\theta = 90^\circ$  is 3.75%  $X_0$  for the whole detector. The flanges are made from glass-fibre/epoxy laminates.

Cosmic ray and beam tests have given point resolutions of  $\sigma_{R\phi} = 90 \mu\text{m}$  in the jet chamber and  $\sigma_z = 600 \mu\text{m}$  on average for the outer layer (angle dependent).

During LEP operation, good efficiency has been reached: typ. 20 points/track in the jet chamber and 95% per layer in the outer section. The average single wire resolution is  $\sigma_{R\phi} = 90 \mu\text{m}$  in the jet chamber (Fig. 8(b)) and  $\sigma_z < 1$  mm in the outer layers. The trigger efficiency for the jet chamber is above 90% for jet events. The outer layers give  $> 95\%$  trigger efficiency for single tracks. During beam ramping and squeeze, the HV has to be lowered, but under normal conditions, background is low: dark current = 6–10 nA per sector in the jet chamber for  $L = 3 \times 10^{30}/\text{cm}^2 \text{ s}$  and gas amplification of about  $10^4$ .

### 5.3 Time Projection Chamber (TPC)

The TPC is the principal tracking device of DELPHI [5]. Pattern recognition normally starts from its information. The size of the TPC being limited ( $R = 120$  cm,  $L = 2 \times 150$  cm) by the inclusion of the RICHes, other track chambers were added (OD, FCA and B; see below) to improve momentum resolution. As the RICHes promise very superior particle identification, operation of the TPC at 1 atm. was specified (although evacuation and 2 atm. are permitted), resulting in substantial technical advantages and lower radiation thickness. The reduced dE/dX information will still be useful, in particular for  $e-\pi$  separation below 8 GeV.

Each end-cap is divided into 6 sector plates with 192 sense wires (spacing = 4 mm; gap =  $2 \times 4$  mm) and 16 circular pad rows (constant spacing) (Fig. 9). A gating grid is placed at 8 mm in front of the cathode grid. The backplane is a G10 sandwich, 6 mm thick, coated with  $70 \mu\text{m}$  copper, with external ribs carrying the preamps and providing structural rigidity and a flatness tolerance of  $20 \mu\text{m}$ . Short



cathode pads (in R) were chosen for better two-track separation: length about 7.5 mm, width 8 mm, both adjusted to give constant surface and a multiple of 16 pads per row; in total 1680 pads per sector. Three rods per sector carry point sources of  $\text{Fe}^{55}$  and permit monitoring and absolute gain calibration of each sense wire when moved into position behind 1 mm holes in the backplane.

If required, feedback of positive ions into the drift volume may be reduced by gating off the amplification zone. This is accomplished by biasing consecutive wires of the gating grid (spacing = 1 mm) to  $\pm 100$  V. The bias is lifted for 3  $\mu\text{s}$  at each beam crossing to permit a level 1 trigger decision and is kept off only in case of a positive response.

The central high voltage plane is an Al honeycomb sandwich. The cylindrical vessels are constructed from carbon fibre composites, each 1.15%  $X_0$  thick. Vacuum tight connectors are mounted on Al rings, which also support the carbon fibre end covers. The field cages consist of G10 laminates (1 and 2 mm thick), with kapton foils carrying 3 mm Cu strips (spaced 1 mm) on both sides. With an Ar/CH<sub>4</sub> 80/20% mixture and nominal drift field of 150 V/cm, the drift velocity is  $v_D = 66.94 \pm .07$  mm/ $\mu\text{s}$  at  $T = 22^\circ\text{C}$ .

MOSFET preamplifiers, including pole-zero cancellation, are directly mounted on the backplane. Emphasis was put on low noise (ENC  $\sim 500$  e<sup>-</sup> on the pads) and low power dissipation (45 mW). After two-stage shapers, 14 MHz sampling is provided by 8-bit Flash ADC's(\*) (used with broken characteristics for increased dynamic range and better resolution at the low end). For the wires, there is the possibility to move to 45 MHz sampling rate to improve two-track resolution.

Six miniature nitrogen lasers, one per sector, are mounted on each end-cap (337 nm; 60  $\mu\text{J}$  in  $1 \times 2$  mm<sup>2</sup>; fwhm = 0.8 ns; diffraction limited). Each laser produces three ionization tracks, one parallel to and 3 cm in front of the gating grid and two diagonally pointing towards the central plane (Fig. 10).

Full gain maps with 1200 points/sector were obtained with a rotating line source ( $\text{Fe}^{55}$ ) before installation of the sectors. They showed excellent homogeneity to  $< 1\%$  over most of the surface.

After 1 year of testing above ground with cosmics and laser beams, the TPC has been operating successfully since the start-up of LEP.

Preliminary resolution results are:  $\sigma_{R\phi} = 180\text{--}280$   $\mu\text{m}$ , depending on  $\Phi$  and  $z$ ;  $\sigma_z < 0.9$  mm; two-track separation = 1.5 cm. These values are very close to the specification. The reconstruction of  $K^0$ 's is shown in Fig. 11(a); the mass resolution is 10 MeV. The dE/dx resolution (using 50% of the smallest samples) is at present  $\sigma = 6.2\%$  for muons at 45 GeV and 7.5% for pions between 280 and 400 MeV. Particle identification at low momenta is shown in Fig. 11(b). This was obtained without pulseheight calibration of the wires. With additional corrections it is expected from test beam data to reach a resolution of about 5.5%. Background is low for the maximum luminosity obtained so far ( $5 \times 10^{30}/\text{cm}^2$  s) and gating is not yet required: dark current = 10 nA/sector and less than 20 hits from synchrotron radiation per beam crossing in the full TPC.

---

(\*) Thomson, France.

#### 5.4 Outer Detector (OD)

The Outer Detector is essential to provide fast trigger information in both  $R\phi$  and  $z$ , and to improve the momentum resolution by a large factor ( $> 5$  for fast particles).

It is composed of 24 modules, mounted on the B-RICH, 4.7 m long and each consisting of 145 drift tubes in 5 layers [5]. The layers are staggered and overlap with the adjacent modules, thus providing full azimuthal coverage. Modules are cold bonded from Al-profiles 1.75 cm square, with high internal surface quality. Tight tolerances were observed for the dimensions of the tubes ( $\pm 50 \mu\text{m}$ ), the positioning of the wires ( $\pm 30 \mu\text{m}$ ) as well as in the mounting of the modules. The drift tubes are operated in the limited streamer mode (wire  $\phi = 110 \mu\text{m}$ ). All layers provide  $R\phi$  information, three in addition provide fast  $z$  information by relative timing of signals from both ends.

Thorough calibration with cosmics and lasers in a magnetic field has given  $\sigma_{R\phi} = 80 \mu\text{m}$  and  $\sigma_z = 2 \text{ cm}$  (with Ar/i-C<sub>4</sub>H<sub>10</sub>/C<sub>3</sub>H<sub>7</sub>OH = 51/48/1%). This performance is a significant improvement upon the original specification of  $\sigma_{R\phi} = 300 \mu\text{m}$  and  $\sigma_z = 7 \text{ cm}$ .

Since LEP start-up, the detector has operated as anticipated.

Preliminary results are:  $\sigma_{R\phi} = 110 \mu\text{m}$ ,  $\sigma_z = 4.4 \text{ cm}$  (Figs 12(a) and (b)). It is possible to determine the charge of tracks, up to the highest momenta, from the track element in the OD alone.

#### 5.5 Barrel Muon Chambers (B-MU)

The Barrel Muon detector is composed of 2 layers. The first layer of  $2 \times 24$  planks is inserted into the return yoke after 90 cm Fe and contains 3 staggered drift-chamber planes. The second layer is mounted on the outside of the yoke, behind a further 20 cm of iron. It consists of overlapping planks, with clearance between them for the passage of cables and pipes, each containing 2 staggered planes of drift-chambers (Fig. 13(a)). Each plank covers half the length of a yoke sector following the shape of the cable ducts to maximize coverage. The active length of the majority of chambers is 3.65 m. All chambers of the second layer are read out, but only 2 planes of the first layer, the third plane being regarded as spares.

Each plank is cold-bonded from accurately extruded Al-tubes, 20.8 cm wide and 2.6 cm high, with a single anode wire in the centre. Two plastic sheets, 0.28 cm thick, are glued to the wider inner surfaces and carry Cu strips for potential grading. A flat delay line is glued to one side below the anode wire, providing length measurements with a delay of  $\sim 1.8 \text{ ns/cm}$ . The cross section for drifting is 20 cm by 1.6 cm high.

The drift chambers operate in the proportional mode, with Ar/CH<sub>4</sub>/CO<sub>2</sub> (85.5/8.5/6%). Chamber signals are six-fold multiplexed into time digitizers. With 2 ns time digitization, tests with beams and cosmics gave  $\sigma_{R\phi} \sim 1 \text{ mm}$  and  $\sigma_z \sim 10 \text{ mm}$ .

Operation at LEP has proven to be very reliable. At the present time the detector is approximately 98% operational, with estimated individual chamber efficiencies of 95%. Overall efficiency for a muon track with typically 4 hits per track is therefore high. Measurements of resolution on extrapolated tracks give

$\sigma_{R\phi} = 4$  mm and  $\sigma_z \sim 2.5$  cm at present (Figs 13(b) and (c)), these figures being limited by the low rate of muons and the accuracy of the track extrapolation.

### 5.6 Forward Chamber A (FCA)

The forward chambers provide powerful tracking and triggering from  $\theta = 33^\circ$  down to  $\theta = 11^\circ$ .

Chamber A is mounted on both ends of the TPC. One side consists of 3 chambers, each with two staggered layers and split into half-discs with an outer radius of 103 cm. The chambers are turned with respect to each other by  $120^\circ$ , thus providing  $2 \times 3$  coordinates:  $xx'$ ,  $uu'$ ,  $vv'$ , where  $x'$  is staggered with respect to  $x$ . The layers are constructed from extruded conductive plastic (bulk resistivity about 15 k $\Omega$ cm) forming square cells (15 mm inside, 0.7 mm walls) with a 100  $\mu$ m anode wire in the centre. A double layer is reinforced on both outer surfaces by 0.7 mm G10 sheets. These sheets carry a pattern of 58 mm wide cathode strips, rotated by  $\pm 60^\circ$  w.r.t. the corresponding anode wires, to improve local pattern recognition (Fig. 14).

With operation in limited streamer mode in Ar/iso-C<sub>4</sub>H<sub>10</sub>/C<sub>2</sub>H<sub>5</sub>OH (48.75/48.75/2.5%), test beam results showed efficiencies for a double layer of  $\epsilon \sim 97\%$  for the anodes. The space resolution was  $\sigma_x = \sim 150$   $\mu$ m for the anode signals.

Preliminary results from operation at LEP are:  $\sigma = \sim 300$   $\mu$ m per layer, and efficiency/double layer  $\sim 95\%$ . Hits on the cathode strips are associated to the wire signals by time correlation ( $\sigma = 15$  ns).

### 5.7 Forward Chamber B (FCB)

Chamber B provides a precise track element using  $4 \times 3$  coordinates  $x$ ,  $u$ ,  $v$  for triggering, pattern recognition and substantially improved momentum resolution in the forward arms. The high redundancy provided by 12 read-out planes offers the possibility to analyze track elements in a high multiplicity and background environment.

The chambers (2 half-discs in each arm) are supported independently on the yoke, between the F-RICH and the F-EMC. A complete disc is a regular dodecagon with inner  $R = 48$  cm and outer  $R = 211$  cm. The 12 sense wire planes (separated by 1.1 cm) are rotated in pairs by  $120^\circ$  with respect to each other:  $(xx', uu', vv') \times 2$ , where  $x'$  is staggered w.r.t.  $x$  and  $(x, u, v)$  coordinates are parallel to those in FCA. The wire planes are tensioned on G10 frames and separated by cathode plates (1 mm thick conducting G10 containing carbon dust). Separate endplates (10 mm honeycomb) close the gas volume. Sense wires are spaced 2 cm and separated by field wires.

Beam tests gave  $\sigma_x < 150$   $\mu$ m and efficiency = 90% per point in Ar/C<sub>2</sub>H<sub>6</sub>/C<sub>2</sub>H<sub>5</sub>OH 50/48/2% at 1.05 T. The inefficiency is concentrated near the potential wire so that the efficiency of a staggered double layer was close to 100%.

Preliminary results from operation at LEP, using "parallel muons" produced at large distance from the interaction point, are:  $\sigma = 290$   $\mu$ m and efficiency = 80% per plane as average over all planes, including

effects from dead areas (Fig. 15). Combining the information of the 12 planes,  $\sigma_x = \sigma_y = 130 \mu\text{m}$  is obtained.

### 5.8 Forward Muon Chambers (F-MU)

Both arms of the Forward Muon Chambers [7] have 2 planes of chambers; one inside the yoke, behind  $\geq 85$  cm of iron, the second 30 cm further out, behind another 20 cm of iron and the Forward Scintillators. Each plane, covering some  $9 \times 9 \text{ m}^2$ , is composed of 4 quadrants ( $4.4 \times 4.4 \text{ m}^2$ ). A quadrant consists of 2 orthogonal layers of 22 drift chambers cold-bonded together.

The drift chamber body is an extruded Al tube, containing PVC profiles with coextruded Cu strips, which act as drift field electrodes ( $E = 700 \text{ V/cm}$ ; see Fig. 16(a)). The sensitive volume is 435.4 cm long, 18.8 cm wide and 2 cm high, with a  $100 \mu\text{m}$  anode wire in the centre. One cathode section facing the anode is formed by a flat solenoidal delay line, producing a pulse delay of 600 ns/m. Coordinates are derived from the anode drift time and the 2 delay line propagation times to both ends. The drift chambers are operated in the limited streamer mode, with a mixture of  $\text{Ar}/\text{CO}_2/\text{iC}_4\text{H}_{10}$  (14, 70, 14%) and 2% i-propanol.

Extensive tests in a cosmic hodoscope have shown  $\sigma_{x,y} = 1 \text{ mm}$  from drift time measurement. Left-right ambiguity is resolved using delay line information of the crossed layer:  $\sigma_{\text{DL}} \sim 2 \text{ mm}$ .

At LEP, halo muons accompanying the beams are used to investigate the detector performance. The efficiency per detector layer, averaged over all layers, was determined to be  $89 \pm 3\%$ , including 8% inefficiency for structural deadspaces. From a sample of muons hitting the four detector layers of one end-cap, the spatial resolution has been evaluated. Fig. 16(b) shows the residuals of the recorded hits w.r.t. the fitted trajectory, separately for each end-cap. These residual distributions ( $\sigma \sim 3 \text{ mm}$ ) represent an average over the 16 detector layers of one end-cap and include drift and delay line measurements. In addition to the detector's resolution, these residuals include effects due to the presence of a magnetic stray field.

### 5.9 SAT Tracker

The Small Angle Tagger (SAT), the principal luminosity monitor, consists of a calorimeter (sect. 7.3) and a tracker in front.

Both arms of the tracker foresee 3 planes of large area Si-detectors<sup>(\*)</sup> at  $z = 203, 216$  and  $230 \text{ cm}$ . The planes cover twice  $1465$  and  $2079 \text{ cm}^2$ , respectively, with an inner radius of  $10 \text{ cm}$ . The sensitive region extends from  $43.5$  to  $120 \text{ mrad}$ . Each plane has circular strips with  $1 \text{ mm}$  pitch in radius and covers  $5^\circ$  in azimuth.

The strip signals are read out by VLSIs built in CMOS<sup>(\*\*)</sup>. Each VLSI has 48 channels with analog and digital sections [8]. After amplification, shaping and discrimination of the signals, the zero-suppressed

---

<sup>(\*)</sup> Micron Semiconductors, England; A.S. Microelectronics, Horten, Norway.  
<sup>(\*\*)</sup> Si, Oslo; IMEC/MITEC, Belgium.

hit patterns are stored in registers. The detectors and VLSIs are mounted on kevlar substrates which also serve as printed circuits. The detectors are contained in a kevlar box with shielding and ducts for air cooling.

The tracker is expected to give a precision of  $\sigma_\theta = 1.5$  mrad and to define the acceptance radius to about  $40 \mu\text{m}$ .

At present, only the 1. and 3. planes are installed in one arm. Due to late installation and noise problems, only a few very preliminary results exist. Fig. 17 shows the radial distance to track extrapolations to high energy showers in the calorimeter section for the nearest hit in the tracker within a  $\phi$  sector of  $10^\circ$ .

In the second arm, a lead mask has been mounted to define the inner acceptance radius (sect. 7.3) for the calorimeter.

### 5.10 Combined tracking

The insertion of the RICHes required a large number of independent tracking devices. Combining their information is essential for the trigger, the vertex and general pattern reconstruction and in particular for high momentum resolution. In the forward region, DELPHI has the potentiality for quite unique resolution for a LEP detector, due to the power of the forward chambers.

Emphasis was, therefore, put on precise relative alignment and survey of the various components, but ultimate precision can only be achieved with high statistics calibration with cosmics and  $Z^0$  events.

So far the following results have been obtained for muon pairs at  $45.6 \text{ GeV}$ :  $dp/p = 7\%$ , i.e.  $\Delta p/p = 0.0015 \times p(\text{GeV})$ , in the barrel region, combining information of ID, TPC and OD (Fig. 18(a)) and  $(dp/p) = 17\%$  in the forward sectors ( $\theta = 20^\circ\text{--}35^\circ$ ), using information from ID, TPC and Chamber B (Fig. 18(b)).

## 6. SCINTILLATOR COUNTERS

### 6.1 Time-Of-Flight Counters (TOF)

The Time-Of-Flight [9] system in the barrel serves as fast trigger for beam events and cosmics and may be used to veto cosmic muons during beam crossings. Cosmics are heavily used for alignment. The rate was measured to be  $10^{-4}$  particles/cm<sup>2</sup> s sr at  $\alpha = 0^\circ$  with  $\cos^2\alpha$  dependence for  $|\alpha| = 0\text{--}60^\circ$ , where  $\alpha$  is the polar angle with respect to the vertical.

The TOF system consists of a single layer of 172 counters ( $355 \times 19 \times 2 \text{ cm}^3$ ) mounted on the inside of the return yoke just outside the solenoid. The counters cover most of the polar angle  $\theta = 41$  to  $139^\circ$ , but leave a dead zone  $6 \text{ cm}$  wide around  $\theta = 90^\circ$  and at the support legs of the cryostat.

NE110 is used as scintillator. On both ends, a PM is connected via Plexiglass light-guides folded back by  $180^\circ$  to reduce the dead zone in the centre and to avoid the higher magnetic field near the cable ducts at the ends of the barrel yoke (Fig. 19). The scintillator wrapped with Al foils produces an effective attenuation length of  $135 \text{ cm}$  and an effective light propagation of  $16 \text{ cm/ns}$ . Signal loss in the light guide

is 78%. Measurements of Cherenkov signals produced by particles traversing the light guides (which cover 32% of the total TOF surface) indicate that less than 10% of the triggers would come from Cherenkov signals with shifted timing.

Time resolution measured with cosmics is  $\sigma_t = 1.2$  ns, corresponding to  $\sigma_z = 20$  cm. A simple back to back coincidence on cosmics using only octants of the TOF gives a rate of 3.5 Hz. Detection efficiency is 99.9% for m.i.p.'s.

## 6.2 Forward Hodoscope

The forward scintillator hodoscopes improve muon detection and trigger system efficiencies for beam events and cosmics. In particular, it is the only trigger on beam related halo muons which are very useful for alignment.

The hodoscopes are mounted in the 45 mm gap between the end-cap yoke and the second muon chamber layer, and cover the whole cross section (in total  $\sim 140$  m<sup>2</sup>) in a single layer. The layer is arranged in quadrants, each containing 28 counters (Fig. 20). The extruded plastic scintillators 1 cm thick, 20 cm wide and up to 450 cm long are mounted with some overlap. They are coupled via bent light-guides (made from the same scintillator sheets) to a single photomultiplier at the outer radius. The light attenuation length was measured to be about 1.5 m and the loss in the light guides less than a factor 3.

Time resolution was measured with halo muons to be 5 ns, averaged over the whole counter. Typical noise rates of 250 Hz/counter lead to a random trigger rate of about 0.1 Hz for back-to-back coincidences of quadrants for a beam crossing gate width of 50 ns. Detection efficiency is 95% for m.i.p.'s at the far end of the counter. The read-out of the hit pattern and time measurements (one per quadrant) are combined with that of the forward muon chambers.

## 7. ELECTROMAGNETIC CALORIMETERS

### 7.1 High-density Projection Chamber (HPC)

The HPC [10] is one of the first large-scale applications of the time-projection principle to calorimetry. The aim is to measure the three-dimensional charge distribution induced by e.m. showers and by hadrons with very high granularity in all coordinates, with an acceptable number of readout channels. The resulting capability of precise tracking allows the detection of e.m. showers and their separation from hadrons even in the complex event topologies encountered at LEP.

With only 18000 electronics channels, a granularity of 4 mm along  $z$ ,  $1^\circ$  in azimuth and a nine-fold radial sampling (over  $18 X_0$ ) have been achieved in the HPC. The dynamical range of the detector allows for e.m. showers up to about 50 GeV with, simultaneously, full sensitivity to minimum ionizing particles.

The time–projection principle is realized by using the lead converter as electric field cage. The ionization charge of showers and tracks is thus extracted onto a single proportional wire plane at one end of each HPC module.

Fig. 21(a) shows the principle of construction. The converter consists of 41 lead walls spaced by 8 mm gas gaps. Each layer is formed by thin trapezoidal lead wires glued to both sides of a fiberglass–epoxy support. A voltage gradient between neighbouring lead wires provides a longitudinal drift field of about 100 V/cm. In these narrow drift channels, charge transmission is limited by transverse diffusion, once the electric drift field in the HPC and the magnetic field in DELPHI are precisely aligned. To adjust to the small radial field component in the magnet, each HPC unit can be tilted by up to  $\pm 5$  mrad for optimization of transmission. Charge attenuation lengths in excess of 350 cm have been obtained in the HPC, for a maximum drift length of 85 cm.

The proportional chambers use pad readout. The pad pattern defines the granularity of radial and azimuthal coordinate sampling (Fig. 21(b)). The drift coordinate  $z$  is obtained by digitizing the amplified ionization charge with bilinear conversion 8–bit FADC's at 15 MHz. The bilinear conversion results in an effective dynamic range of 800:1. The associated electronics provides excellent tail suppression (less than 0.1% of peak height after 1  $\mu$ s) and base line stability. This electronics, combined with an efficient on–board zero–suppression scheme, results in an average data transfer rate of only 14 kbytes per hadronic interaction at LEP for the complete HPC detector.

For fast triggering purposes, a plane of scintillators is inserted into one of the HPC sampling gaps close to the shower maximum (behind  $4.5 X_0$ ). The readout uses 4–6 m long plastic fibers to PM tubes mounted outside the cryostat.

A second level trigger decision is derived from the analog electronics of each HPC unit. The trigger is based on coincidence patterns inside the HPC and is fully efficient for about 1 GeV shower energy.

The HPC detector covers the barrel area inside the magnetic field with 144 separate modules, using a segmentation of 24 in azimuth and 6 along  $z$ . The polar angle coverage is  $43^\circ$  to  $137^\circ$ . The modules are offset by  $7.5^\circ$  in  $\phi$  w.r.t. the hadron calorimeter to achieve optimum solid angle coverage. Gaps between modules are 1 cm in  $z$  and  $\phi$ , except for a gap of 7.5 cm at  $z = 0$  caused by a stiffening ring inside the cryostat. This zone is covered by scintillator/lead sandwich blocks which are read out via wave–length shifter and fibers, providing crude shower information and 97% efficiency for m.i.p.

Before installation, each module was tested with cosmic muons for drift performance and gain control. A subsample of modules was tested with electron beams. After installation, performance and calibration are checked with three  $\alpha$ –sources installed in each module and, at regular intervals, with a minute admixture of radioactive Kr gas emitting 40 keV photons [11]. From test beam data on shower axis reconstruction, the angular resolution of the HPC alone (without vertex constraint) was found to be  $(36/\sqrt{E} + 2.5)$ mrad in  $\theta$  and  $(97/\sqrt{E} + 10)$ mrad in  $\phi$  for fixed  $\theta$  and  $\phi$ .

All 144 HPC modules are operating reliably. An example of the detailed event topology available from HPC information is presented in Fig. 22(c) for a Bhabha event and (d) for a multishower event.

The reconstruction of  $\pi^0$ 's in low multiplicity events is demonstrated in Fig. 23(a).

The power of the angular resolution in HPC is illustrated in Fig. 23(b), which shows the track angles for electrons and positrons from Bhabha events at the  $Z^0$ , as measured in the HPC alone.

## 7.2 Forward Electromagnetic Calorimeter (FEMC)

Good energy resolution and granularity were the principle aims of the forward e.m. calorimeter.

The FEMC consists of two 5 m diameter disks with a total of 9064 lead glass blocks in form of truncated pyramids, arranged to almost point ( $-3^\circ$ ) towards the interaction point. They cover polar angles  $10^\circ < \theta < 36.5^\circ$  and  $143.5^\circ < \theta < 170^\circ$  (Fig. 24).

The lead glass<sup>(\*)</sup> counters ( $20 X_0$  deep,  $5 \times 5 \text{ cm}^2 \sim 1^\circ \times 1^\circ$ ) are read out with newly developed vacuum phototriodes<sup>(\*\*)</sup>, giving an average gain of 12, which is reduced by 30% in the 1.2 T field [12(a)]. Each counter has been calibrated in a 20 GeV electron beam, half of them twice with one year interval, showing a stability of response better than 1%.

The preamplifiers show very low noise:  $166 \pm 9$  electrons r.m.s. with open input;  $270 \pm 20$  electrons directly mounted on the phototriodes in the laboratory and 300 electrons in the complete calorimeter module in the experiments; this corresponds to about 20 MeV of energy deposit.

The test beam results [12(c)] showed an energy resolution of  $\sigma_E/E = [(0.35 + 5/\sqrt{E})^2 + (6/E)^2]^{1/2}\%$ , with E in GeV/c, the last term being due to amplification noise.

At LEP, the energy resolution is degraded due to about two radiation lengths of material in front of the calorimeter. Bhabhas at 45 GeV were measured with  $\sigma_E = 6\%$ , using calibration constants obtained in the test beam and rescaled for the effect of the magnetic field by means of monitoring pulses from a high stability Xenon lamp. By using part of the data to correct these constants, the resolution could be improved in the following data to  $\sigma_E = 4\%$  (Fig. 25(a)). The good precision in the reconstruction of the shower position is visible in Fig. 25(b), which shows the difference between the polar angles of electrons and positrons ( $\sigma_\theta = 0.3^\circ$ ).

## 7.3 Small Angle Tagger (SAT)

The SAT is optimized for luminosity measurements counting Bhabha events. Each arm consists of a calorimeter and a tracker (sect. 5.9) in front.

---

(\*) Glass type SF3,  $X_0 = 2.04 \text{ cm}$ , by Schott Glaswerke – FRG.  
(\*\*) Type R2184–01 by Hamamatsu Photonics K.K. – Japan.



The calorimeter, covering polar angles from 43 to 135 mrad, consists of alternating layers of lead sheets (0.9 mm thick) and plastic scintillating fibres ( $\varnothing = 1$  mm)<sup>(\*)</sup>, aligned parallel to the beam. Scintillating fibres were chosen because of their excellent radiation hardness and because they can easily be fitted into a cylindrical geometry. The fibre and lead layers are bonded with double-sided adhesive tape and mounted into an Al support in form of half-cylinders. The total thickness is 28 radiation lengths. Behind the calorimeter, the fibres are collected in 144 bundles per half-cylinder (450–800 fibres per bundle) and coupled via conical lightguides to circular photodiodes<sup>(\*\*)</sup> with 1 cm<sup>2</sup> active area. Light collection is about 70%, diode quantum efficiency 90% at the peak. With the amplifiers developed for the FEMC ( $\tau = 1$   $\mu$ s), a noise of  $\sim 550$  e<sup>-</sup>/channel is achieved at  $T = 25^\circ\text{C}$ . A 45° prototype had shown an energy resolution of  $\sigma_E/E = (\sqrt{1.2^2 + 11.4^2/E} + 2.3)\%$  with good linearity from 10 to 70 GeV. The 2.3% term is due to response variations across the module. The impact point was determined to 2 mm.

The read-out segmentation is shown in Fig. 26(a). In the vertical plane, there is a 2 cm wide dead-zone between the 2 half cylinders. The inner four rings have 15°, the outer 4 rings 7.5° segments. Radial segmentation is 3 cm, resp. 3.2 cm for the outer 2 rings. The inner radius of the fiducial volume will be measured with high precision ( $\sim 40$   $\mu$ m) by the trackers. Until the trackers are both commissioned, a lead mask (10  $X_0$  thick) is used on one arm (Fig. 26(b)). Its conical outer surface defines the acceptance radius to  $< 100$   $\mu$ m. Zones of 15° from the vertical have also been excluded from the fiducial volume (Fig. 26(a)).

Fig. 27 gives a scatter plot of shower coincidences as measured in both arms. The cut for Bhabha events is indicated. The total systematic error on the luminosity determination is estimated to be 2.0% at present. The main contributions come from internal geometry uncertainties associated with the  $\phi$ -cut, from energy cut, MC modeling and theory (1%).

#### 7.4 Very Small Angle Tagger (VSAT)

A tagger in the very forward arms is needed for fast monitoring of both luminosity and machine operation. As SAT and VSAT give different rates and systematic errors, their luminosity measurements are independent.

The detector in each arm is composed of two rectangular W-Si calorimeter stacks, 24  $X_0$  deep, 5 cm high, 3 cm wide and 10 cm long. The blocks are mounted at  $z = \pm 7.7$  m to both horizontal sides of the elliptic beam pipe and fixed to the support of the superconducting quadrupoles (survey precision 0.2 mm). They cover polar angles between 5 and 7 mrad (6 to 8 cm from beam axis) and an azimuth of  $\pm 45^\circ$  around the horizontal axis.

The accepted cross section for two-tag events is about 400 nb with the superconducting quadrupoles powered, leading to a Bhabha rate 10 times the  $Z_0$  rate on the peak.

---

(\*) Optecron, France.

(\*\*) A.S. Microelectronics, Horten, Norway.

The VSAT detector is also designed to measure the background of single electrons and of x-rays. These measurements provide both checks of orbit calculations for the LEP machine and a measure of the background to the Bhabha process. All events are bunch labelled, an essential prerequisite for LEP operation with polarized beams.

Each stack consists of 12 W-plates ( $2 X_0$  thick), interleaved with full area Si-detectors ( $3 \times 5 \text{ cm}^2$ ) for energy measurement. Each full area detector is monitored by an  $\alpha$ -source. Two Si-planes with 32 vertical strips (1 mm pitch) are inserted behind 5 and 9  $X_0$  and one plane with 48 horizontal strips behind 7  $X_0$ .

Energy spectrum and rates of off-momentum electrons are different for modules situated outside and inside the LEP circumference: a few hundred Hz of electrons with energy close to that of the beam on the outside and a much softer energy spectrum and a rate below 100 Hz on the inside. Monte Carlo predictions using TURTLE program for the LEP beams agree with these observations within a factor 2. Fig. 28(a) shows the scatter plot for Bhabha triggers of the energy deposition in an external module and its diagonal internal partner.

The information from the strips is used to eliminate showers at the edge of the detector and to correct for lateral energy leakage. Fig. 28(b) shows a projection on one axis of Fig. 28(a) after a circular energy cut of  $3\sigma$  around the Bhabha peak. One obtains an energy resolution of 5% at 45 GeV, in agreement with the Monte Carlo predictions for fully contained showers ( $35\%/\sqrt{E}$ ). In Figs 28(c) and (d) transverse profiles are shown for the first x plane and for the y plane, averaged over many showers.

## 8. HADRON CALORIMETER

The hadron calorimeter [13] is a sampling gas detector incorporated in the magnet yoke, the barrel part covering polar angles between  $42.6^\circ$ – $137.4^\circ$ , and two end-caps between polar angles of  $11.2^\circ$ – $48.5^\circ$  and  $131.5^\circ$ – $168.8^\circ$ . The barrel is constructed of 24 sectors, with 20 layers of limited streamer mode detectors inserted into 2 cm slots between the 5 cm iron plates in each sector. The modularity of the end-caps is similar to the barrel, with a sampling depth of 19 layers. The detectors are wire chambers which consist of a plastic cathode forming 8 cells of  $9 \times 9 \text{ mm}^2$  with one anode wire in each. The inner surface of the cathode cells is coated with a poorly conductive graphite varnish with surface resistivity  $> 50 \text{ k}\Omega/\square$ . The  $80 \mu\text{m}$  anode wires are made of copper-beryllium. Special emphasis was placed on tight production tolerances, repeated polishing of the conductive layer, repainting of insulator spots, quality of wire, tolerance of spacers and profiles and gas tightness. Thorough tests of the detectors with stringent rejection criteria were performed in order to maximise the operational reliability.

The calorimeter contains about 19,032 detectors varying in length between 40 and 410 cm. They operate stably with relatively low i-butane content: Ar/CO<sub>2</sub>/i-butane 10/60/30%. This is important, as the hadron calorimeter contains by far the largest volume of gas in DELPHI and small leaks (mostly due to diffusion through the PVC) are unavoidable in this construction. With this gas mixture, an average charge of

10 pC is induced on the external readout boards with a HV of 3.92 kV. The HV of each detector can be disconnected individually to reduce dead zones in case of a defect.

The copper clad read-out boards are segmented into pads which pick up the streamer charges. Pads are shaped to form towers pointing to the intersection point; in the barrel (end-caps), pads of 5 (4 or 7) adjacent layers are combined into a tower. Each tower covers an angular region of  $\Delta\phi = 3.75^\circ$  and  $\Delta\theta = 2.96^\circ$  in the barrel and  $\Delta\theta = 2.62^\circ$  in the end-caps. The dimensions of a typical tower in the barrel are  $25 \times 25 \times 35 \text{ cm}^3$  (Fig. 29).

The analogue signals from towers are collected into 96 front-end electronics crates (one per sector) for charge integration, multiplexing by 256, 8-bit analog-to-digital conversion, zero suppression and a discrimination according to a control signal. The quality of the charge integration amplifiers was tested carefully to reduce fluctuations in the signals. The charge integration time is 2  $\mu\text{s}$ . A fast discrimination of the signals from groups of  $4 \times 4$  towers (supertowers) is performed and logical combinations of the supertower signals are available for triggering purposes. The zero suppressed data are processed in a local FASTBUS data acquisition system, essentially composed of 12 receiver cards, a high speed buffer memory and a crate control processor.

At LEP, operation has become smooth after solving severe noise problems. Even during LEP fills, the HV can be kept on. During 6 months of machine operation the tube failures are essentially zero, random faults are at the level of 0.5% and may be repaired.

The performance of the detector has been studied using hadronic and dimuonic events from  $Z^0$  decay. For the hadronic analysis tracks measured in the TPC and punching through to interact in the hadron calorimeter were used. Fig. 30(a) shows the average energy deposition in the calorimeter against the momentum measured in the TPC: good linearity up to 10 GeV is evident and in fact linearity up to 60 GeV has been found for a single sector in a beam test. Fig. 30(b) shows an estimate of the resolution in which  $dE/E$  is scaled by  $\sqrt{E}$ . The resolution is about  $120\%/\sqrt{E}$ . To obtain an estimation of resolution for jets, jet energies were composed by adding up the energies of TPC tracks and the data are compatible with a resolution of  $120\%/\sqrt{E}$ . Figs 30(c) and (d) show the total energy deposited for hadronic Z events and for background events, respectively. The calorimeter alone can distinguish  $Z^0$  events from background. Fig. 30(c) also shows a Monte Carlo result in good agreement with the data. The efficiency of single muon detection in the barrel for muons resulting from the dimuon decay of the  $Z^0$  is around 80%, both muons being identified in the Muon chambers.

## 9. RING IMAGING CHERENKOV COUNTERS (RICH)

The aim of the novel RICH detectors is superior hadron identification over most of the momentum range by Cherenkov angle reconstruction from both gas and liquid radiators:  $4.2 \sigma$ -separation for  $\pi/K$  up to 18 (30) GeV/c and for K/p up to 33 (50) GeV/c in the Barrel (Forward) RICH [14(a),15].

### 9.1 Barrel-RICH

The design of the Barrel-RICH is shown in Fig. 31(a). It is a 3.5 m long cylinder with inner  $\varnothing = 246$  cm and outer  $\varnothing = 394$  cm, divided into two halves by a central support wall, 6.4 cm thick. Liquid radiator boxes (1 cm liquid) with quartz windows on the outer surface are mounted near the inner radius. UV-photons are detected in the drift-tubes constructed entirely from quartz plates<sup>(\*)</sup>, which act as a TPC with read-out chambers at the outer end. Cherenkov-photons produced in the outer gas volume are reflected by parabolic mirrors<sup>(\*\*)</sup> and focussed into ring images in the same drift tubes. Each half contains 24 drift tubes and liquid radiators in azimuth, grouped in pairs. Next to an electron attenuation length that is large compared to the 155 cm length of the drifttubes, minimal distortion of the drift trajectories is essential. Great care has been taken to produce a homogeneous drift field by precise construction and by providing conductive strips on both the inside and outside of the quartz windows: the strips, 0.1 mm wide with pitch = 3 mm, were produced by vacuum deposition. An additional double field cage with 100  $\mu$ m wires at 6 mm pitch is mounted from the drifttubes 1.4 cm to the side of the mirrors. The tapering of the drifttube gap (4.2 to 6.2 cm) improves the electron collection efficiency. For calibration and monitoring of the electron drift parameters, UV lightpulses are injected into the driftboxes through quartz fibres, producing 5 rows (along z) with 9 spots across each box. Attenuation lengths of the order of 10 m and drift deviations close to the tube walls of less than 1 mm over 150 cm drift have been demonstrated [14(b)].

The inner cylinder of the vessel contains a 15 mm thick insulator wound onto an Al honeycomb cylinder. The insulator consists of 93 mylar layers of 120  $\mu$ m embedded in polyurethane and is topped by a HV degrader (strips at 6 mm pitch on kapton) [14(c)]. To the inner radius are glued heating strips, thermal insulation and water cooling pipes. Similar arrangements for heating of the detector are found on the outer cylinder and endplates of the vessel to allow operation up to 40°C.

The read-out chambers are operated at a charge multiplication of approximately  $2 \times 10^5$  for efficient single photoelectron detection. They contain blinds with high walls between the sense wires to reduce crosstalk by photon feed-back and gating grids to reduce space charge build-up (Fig. 31(b)). The chambers provide 3-D reconstruction of photon conversion points from anode and cathode signals and time information. Cathode-strip efficiency is 85–90% for single-electrons [14(d)].

Some other design parameters are summarized below:

- Liquid radiator:  $C_6F_{14}$ ,  $\langle n \rangle = 1.278$  at 6.5 eV, threshold  $\gamma = 1.6$ ; UV-Absorption after cleaning:  $< 20\%/cm$  for  $E_{ph} < 6.9$  eV,  $< 5\%/cm$  for  $E_{ph} < 6.6$  eV.
- Gas radiator:  $C_5F_{12}$ ,  $\langle n \rangle = 1.00174$  at 6.5 eV (40°C, 1 atm.), threshold  $\mu = 16.9$ .
- Drift gas:  $CH_4/C_2H_6$  75/25% + photo-ionizing substance TMAE, drift field = 600 V/cm; photon absorption length = 2.5 (1.3) cm for TMAE of 20 (30)°C.

---

(\*) Nippon Silica, Japan.

(\*\*) Bofors, Sweden [9.1(e)].

- Quartz transparency (0.4 cm): > 80% for  $E_{ph} < 6.5$  eV.
- Mirrors: 288 in total, 6 shapes, vacuum formed on moulds. Coating: Al +  $MgF_2$ ; reflectivity: > 85% over the relevant wavelength region [14(e)].
- Gas tightness: Contamination of the drift gas by  $C_5F_{12}$  has to be kept very low, as 1 ppm leads to 39%  $e^-$  absorption over 1 m drift. Oxygen contamination should also remain below  $\sim 1$  ppm to limit the concentration of electronegative TMAE oxidation products.

Each drift tube was tested for gas leaks, HV and drift properties before installation. The fluid systems have to provide very clean fluids (for good UV transparency and low electron-absorption) and safe pressure control: a differential pressure of only 0.1 atm. can break the quartz windows.

All Barrel RICH components are installed, except the drifttubes on one half-cylinder; these will be added in autumn 1990. All 24 installed drifttubes and the 24 liquid radiators facing them are in operation. Fig. 32 displays examples of Cherenkov images obtained from the liquid radiator. An individual ring is shown in Fig. 32(a), a superposition of rings from cosmic muons in Fig. 32(b). Rings from muon pairs and hadrons with momenta  $p > 6$  GeV/c are displayed in Fig. 32(c) and (d), respectively. The peak in the corresponding distribution of reconstructed photon angles (Fig. 32(e), (f)) is centred at the correct value for  $\beta = 1$  particles. The error on those still largely uncorrected data,  $\sigma_\theta = 18$  mrad, contains an appreciable contribution from extrapolation errors on the particle tracks, to be eliminated after proper tuning and alignment. The average number of photo-electrons per liquid-radiator ring from nearly perpendicularly incident tracks is  $\langle N_{ph} \rangle = 12$ . These data were obtained with an effective TMAE temperature of 13°C at 1 atm. They scale with the prototype result  $\langle N_{ph} \rangle = 18$  for warm TMAE.

Next to increasing the TMAE concentration, heating is also necessary for  $C_5F_{12}$  as gas radiator which provides the highest number of photoelectrons; the boiling point of  $C_5F_{12}$  is 30°C at 1 atm. The full system for heating and temperature control of the Barrel RICH elements has been implemented. It is gradually being brought into operation, with careful monitoring of effects on other DELPHI components.

## 9.2 Forward RICH

The construction of the Forward-RICH [15] has to be different from that of the Barrel RICH because of the geometry and the crossed E-B fields in the photon detectors. The design is shown in Fig. 33(a,b). Each end-cap consists of two truncated half-cones and is divided in azimuth into 12 modular sectors. Each such sector contains one driftbox, two MWPC's, three liquid-radiator containers and five mirrors. The MWPC's are mounted radially on the two borders of each 30° sector. Each MWPC has two crossed layers of photon screens to cope with the crossed E-B field configuration (Fig. 33(c)).

The vessel is built from carbon-epoxy laminate and contains heating elements on the inside and cooling pipes on the outside. The two vessels of one end-cap are supported from the iron yoke on a carbon epoxy cylinder, which has been tested to bend 1 mm under the 1 t load.

Operation is foreseen at 1 atm., with  $C_5F_{10}$  and  $C_6F_{12}$  as gas and liquid radiators and  $C_2H_6 + TMAE$  as driftgas. With a prototype, good rings were obtained in a test beam with  $\sim 20$  photoelectrons/ring from the liquid and  $\sim 10$  from the gas radiators (Fig. 34).

At LEP, one end-cap is mounted so far, but with only two drift-boxes. Because of the priority given to the B-RICH, electronics for only one modular sector of the Forward RICH has been constructed so far. Also other items have been delayed: the drift-boxes (13 of 24 now available), the read-out chambers (20 of 48 now available) and all of the the fluid systems. On the other hand, all mirrors and all liquid radiators are mounted in the 4 vessels. Photons generated by a UV-flash lamp and injected at specific locations in one of the two drift-boxes now installed, have been detected and read out through the data-acquisition chain. First detection of Cherenkov photons from some liquid radiator containers filled with  $C_6F_{14}$  is planned for August 1990.

## 10. GAS SYSTEMS

Standardisation was considered essential for the 16 gas systems required in DELPHI [16]. Only the systems for the RICHes contain some special elements. Each detector system has an individual gas mixer, and one or more distribution modules to meter the gas to and from each chamber. Mixer and distribution modules are controlled by individual G64 microprocessors, which operate local or remote run/stop commands, and continually monitor for leaks, mixture errors, etc. Small excursions cause warnings to the operators; larger errors stop the supply, and automatically ramp down the chamber high tension. Alarm messages and changes in gas pressures and mixtures are communicated to the rest of the slow controls system (sect. 11) with "STRINGLISH" plain text on Ethernet.

The mixers use Mass Flow Controllers: the carrier gas flows on demand via a pressure regulator to maintain a constant 200 mbar supply pressure, while component gas and vapour flows are "slaved" to the measured carrier gas flow. The microprocessor iteratively corrects the mixture ratios, giving a mixture stability of  $\pm 0.1\%$  as measured by the flow controllers.

Multichannel distribution modules electronically measure supply/return flows to  $\pm 2\%$ . In addition, hygrometers and oxygen meters sample chamber exhaust gases from up to 48 channels of some systems.

The TPC and HPC distributions recompress the exhaust gas and recirculate it via purifier modules. The gas is dried by molecular sieves, then oxygen is removed with active copper pellets. The used column is regenerated under microprocessor control by electrical heating to  $200^\circ$  under argon + 7% hydrogen backflow to expel water and reduce copper oxide to copper. Meanwhile, a standby column takes over purification. About 10% of the  $Ar + CH_4$  return gas is vented and replaced by fresh mixture to prevent excessive nitrogen building up in the circuit. At a flow rate of 1600 NI/h, both purifiers give output levels of about 0.5 ppm oxygen and 1-3 ppm water.

## 11. THE SLOW CONTROLS SYSTEM

DELPHI has been equipped with an automated system for monitoring and controlling technical aspects of the experiment, and for reporting and acting on changes in the status of the detector or its environment [17].

The system is based on a series of microprocessors, communicating over the DELPHI local area network with the MicroVAX control computers.

The main functions of the slow controls system are as follows:

- Monitoring of slowly-varying values (e.g. temperatures), and checking that they are within acceptable limits, to guarantee safety and successful data-taking.
- Keeping a record of parameters important for the subsequent analysis of the data.
- Control of detector voltages and gas supplies, either by global commands from the operator (such as at the beginning of a run), or from detector experts, or automatically based on conditions detected during monitoring.

Most monitoring and control is performed by systems based on the G64 standard implemented in special "MAC" crates. This crate has a lower frame with the standard G64 backplane, and an upper frame taking purpose-built "MAC" cards to interface to the detector hardware. The G64 crates themselves are driven using a paging processor card<sup>(\*)</sup>. G64/MAC crates can be fitted with various types of input/output card, such as ADCs, digital relay cards, temperature monitoring cards, etc.

Most detectors have a MicroVAX "Equipment Computer" and several G64 crates, with between 20 and 2000 channels per crate. These are connected by thin-wire Ethernet and a G64 interface card.

In addition to the computer-based monitoring, independent hard-wired interlocks are provided to cut high voltages in the event of a serious gas loss, a magnet quench, or a signal from the "General Safety and Surveillance" (GSS) system. This system incorporates detectors for gas, smoke, and flood, etc. The GSS and DELPHI computers keep each other informed of safety problems via the local-area network and, for less serious alarm conditions, computer control is used before activating the hard-wired interlocks in order to allow an orderly shutdown of apparatus.

The organization of the slow controls software is shown in Fig. 35.

Most of the G64s run a standard (EPROM or disk-based) program. This program accepts requests from the MicroVAX to return data read from the hardware, or to change a parameter. Commands can also be given directly via the G64 keyboard. Channels are continuously monitored and compared against acceptable limits, discrepancies being reported to the MicroVAX. The configuration of cards, the list of channels to monitor, and error limits are downloaded from a central database by the MicroVAX.

---

(\*) With Motorola 6809 microprocessor

Communication between MicroVAX and G64 is effected using the Remote Procedure Call (RPC) model, in which the applications programs make subroutine calls, with the data to be sent or returned are passed as normal parameters. The RPC system handles the encoding/decoding and sending/receiving of the data, using the CATS and OSI standards for message transfer over Ethernet.

For each slow controls logical subsystem (e.g., the high voltage control for a specific detector), there is an "Elementary Process" (EP) in the MicroVAX equipment computer. This sends requests to the G64 and receives alarm indications from it using RPCs. On startup, the data defining the G64 channels to be monitored is read from the central DELPHI database. This information also allows the G64s to be initialised. When initialisation is complete, the EP performs the following functions:

- Error conditions detected by the G64 and reported to the EP are passed on to a distributed error message handling facility, "EMU", which can route messages to a number of destinations, such as logfiles or VDU displays, or broadcast them to specified users.
- Detailed changes in detector status, e.g. the tripping of some channels, or changes in the values of parameters needed for the reconstruction of data, are written to the central database. Monitoring rates and tolerances in the values of such parameters form part of the data read from the database on initialisation.
- Adjustment of the values of individual channels can be made by an interactive program.

A distributed state management facility, "SMI", hierarchically coordinates all the Elementary Processes for one detector with each other and performs an overall coordination of the state of all the detectors in DELPHI. Each EP reports the state of its subsystem to SMI, which uses these both for automatic control (for instance, switching off part or all of DELPHI when an alarm such as a gas loss, is indicated), and for providing an operator's display of the state of each detector. The operator can then give SMI commands to control any desired part of DELPHI. This facility is, however, regulated by an authorisation scheme, based upon normal VMS rights identification.

## 12. THE TRIGGER

### 12.1 Survey of the Trigger System

A four-level trigger system was designed to cope with high luminosities and large background rates [14(a)]. During the first year of relatively low luminosity, only the first level and the most important components of the second level trigger were implemented.

In the four level scheme, the first two trigger levels are synchronous with the Beam Cross Over (BCO), which occurs every 22  $\mu$ s. The trigger decisions for the first and second levels are taken 3 and 40  $\mu$ s after the BCO respectively. The third and fourth level triggers are asynchronous with respect to the BCO. The processing time is expected to be typically 30 ms and 300-500 ms respectively.



The timing of the first level trigger is set to minimise the space charge in the Time Projection Chamber. For the second level trigger, data from detectors with long drift times are used, causing the loss of one BCO for an event having passed trigger level one. The task of the third level trigger is to reduce the trigger rate to a few Hertz at the highest luminosities.

## 12.2 The First and Second Level Trigger Scheme

The central trigger decision for the first and second level trigger is taken by the Trigger Supervisor. This module receives trigger information prepared by the subtrigger, units which handle the signals provided by the detectors.

The main trigger components are: "Track", "Muon", "Electromagnetic Energy", "Hadron Energy" and "Bhabha". In addition, a special cosmic ray trigger provided by the Time of Flight (TOF) counters is used for calibration purposes and can be activated between bunch crossings when the DELPHI detector is idle.

The whole trigger electronics was designed in Fastbus standard. However, in the first year of operation also a trigger component using NIM electronics was implemented to treat the signals given by the scintillation counters (TOF, HPG trigger counters and HOF) and by wire chamber planes (ID, OD and FCA/B).

The trigger data from the subtriggers contain multiplicity information on the number of tracks (0, 1, 2 and more than 2), or number of energy clusters above a given threshold for the calorimeters.

The Trigger Supervisor module accepts 120 input signals. The required combination of logical "AND" and "OR" of these signals is defined by a look-up-table which is programmed and loaded into the module. The system was designed to allow for a high degree of flexibility with four final trigger combinations which are equipped with scalers for downscaling.

### 12.2.1 The Track Trigger

The charged track trigger has two independent components, one in the barrel and one in the forward/backward region. A barrel track trigger uses signals from the Inner and the Outer Detector. A correlation between the two detectors is done in the R- $\phi$  plane where 24 segments of the Inner Detector are correlated with the corresponding 24 modules of the Outer Detector. The polar angle acceptance of the barrel ID\*OD trigger is  $42^\circ < \theta < 138^\circ$ .

The TPC provides a second level barrel track trigger using the "OR" of the ID and OD signals as first level (pretrigger). This second level TPC trigger has two components, the R-Z and the contiguity trigger [18(b)].

The R-Z trigger operates in the R-Z projection of each TPC sector, requiring for a track that at least 13 of the 16 pad rows are hit. The contiguity trigger operates in three dimensions using typically groups of four pads in a row as the smallest element in order to define a road of contiguously hit elements. The TPC trigger has polar angle acceptance limited by the ID detector as  $27^\circ < \theta < 153^\circ$ . Tracks produced in the six

inefficient regions of the TPC at the separation between the TPC wedges are rescued by the ID\*OD trigger. The TPC trigger has been used as single track trigger with threshold in transverse momentum which could be programmed in the range from 0.3 up to 1.6 GeV/c. The operation of this trigger is illustrated by the  $\tau$  candidate event in Fig. 36 where the hit pattern of the contiguity trigger is compared to the actual hit pattern of the TPC read-out.

The forward/backward track trigger uses data from Forward Chambers A and B. The first level trigger works in the x, u and v wire projection of FCA and FCB. For each wire orientation of FCA, groups of four wires are formed which are correlated with corresponding wire groups in FCB.

For the second level trigger, reconstructed points rather than projections are used, requiring the sum of the three coordinates to fulfil the triangle criteria. The forward/backward track trigger has transverse momentum threshold of about 1.6 GeV/c. As a consequence of the large background in the forward/backward region due to beam halo, this trigger was used requiring a multiplicity of at least two tracks. It is planned to add a first and second level forward/backward trigger using the TPC wire information to be correlated to the FCA/B chambers in order to be able to trigger on single tracks.

### 12.2.2 The Muon Trigger

The detectors participating in the muon trigger are the TOF, HOF and the Muon Chambers. The muon signature is provided by the muon chambers.

In the first year of operation of DELPHI, this trigger was implemented in the forward/backward region. The first level trigger uses the signals from the HOF counters while at the second level hits having the appropriate space correlation are required in three out of the four muon drift chambers.

### 12.2.3 The Electromagnetic Energy Trigger

The first level barrel trigger is provided by the HPC trigger counters. The scintillators are read out by photomultipliers via optical fibres. The segmentation is identical to that of the HPC modules.

The second level barrel trigger is based on the pulse-heights from the 128 pads per module arranged in six groups for the trigger. For each group of pads, the drifting charges are digitized in 32 time samples. From the 6 times 32 samples per module, a pattern of at least 2-4 (normally 3) consecutive pad groups and drift times above a given threshold defines a module with an acceptable energy deposition. This energy trigger, eliminates the background of the lead absorber due to local energy depositions originating from natural radioactivity.

During the first year of running, the HPC trigger modules were arranged in eight sectors, four with  $z < 0$  and four with  $z > 0$ .

The forward/backward first and second level electromagnetic energy triggers are provided by the Forward Electromagnetic Calorimeter (FEMC). The trigger gives the number of superblocks (0, 1, 2 and

> 2) with energy depositions above two thresholds. A superblock consists of 16-32 leadglass blocks. The trigger segmentation is 24 in phi and 6 in theta.

The second level trigger also contains information on the total energy above two energy thresholds in the very forward, forward, very backward and backward regions, coded on two trigger signals for each region.

Presently, the energy threshold for electromagnetic showers was set to about 2 GeV in the barrel region and to about 3.5 GeV in the forward/backward region.

#### 12.2.4 The Hadron Energy Trigger

For the first level trigger, the hadron calorimeter segmentation is 24 in phi and 2 in theta for the barrel region. The pulse-height sums are compared with a low and a high energy threshold.

For the second level trigger, the segmentation is again 24 in phi, 2 in theta for the forward and backward regions and 6 in theta for the barrel region. The total energy deposition is compared with two energy thresholds for each of the five regions.

The trigger components formed by the hadron calorimeters were not yet implemented.

#### 12.2.5 The Bhabha Trigger

The forward  $e^+e^-$  trigger (the Bhabha trigger) is provided by the Small Angle Tagger (SAT) and the Very Small Angle Tagger (VSAT). Coplanar energy depositions of at least 13 GeV are required in both the forward and backward detectors. The SAT is divided in phi in  $30^\circ$  wide segments having a  $15^\circ$  overlap with each of the adjacent segments. For the first level trigger, the SAT also provides multiplicity information for each arm and a pre-scaled single arm trigger used for efficiency studies.

The VSAT Bhabha trigger requires energy depositions exceeding 30 GeV in opposite modules. A special fake Bhabha trigger, measuring the accidental coincidence rate, requires a single arm trigger from one Beam Cross Over in coincidence with a single arm trigger from the next four Beam Cross Overs.

### 12.3 Summary of Trigger Operation

In the first year of operation of DELPHI, most trigger components which had been foreseen were actually implemented. Some of them, however, we used in a simplified form with respect to the original design.

With a luminosity of a few  $10^{30} \text{ cm}^{-2}\text{s}^{-1}$  typical trigger rates were of about 500 Hz for the first level and of 2–3 Hz for the second level trigger. The main trigger components used in the experiment are listed in table 3. The redundancy of the various components has allowed studying trigger efficiencies for hadronic and leptonic events of usual topology. As an example, the trigger efficiency for hadronic events is presented in Fig. 37 as a function of the polar angle of the sphericity axes.

## 13. THE READOUT SYSTEM

### 13.1 Introduction

The readout system is based on the Fastbus standard. The system divides into three main areas separated by data buffers.

The first area is hardware controlled and the operations are synchronous with the crossing of the beam bunches - the Beam Cross Over (BCO). The main functions are to activate the first and second level trigger procedures and to get the Front End Buffers ready for the next event. The complete sequence takes about 3.5 ms.

The second area is software controlled and asynchronous with the Beam Cross Over. This is the main readout phase and the main functions are the transfer of data from the Front End Buffers to the Multi Event Buffer of each detector and the third level trigger processing. Inspection of the data can be performed with the Equipment Computer of each detector via the Spy Event Buffer. The complete sequence of third level trigger processing and data transfer to the Multi Event Buffer takes typically 30 ms.

The third area is also software controlled and performs the transfer of data from the various Multi Event Buffers to a single Global Event Buffer. The fourth level processing is performed by a set of emulators tagging the various event types. The data are finally transferred for storage on magnetic tape at a maximum rate of about 3 Hz.

### 13.2 The First and Second Level Trigger Phase

The accumulation of data in the Front End Buffers takes from a few hundred nanoseconds to 23  $\mu$ s for the detector with the longest drift time. The first level trigger decision is taken 3  $\mu$ s after the Beam Cross Over and in case of a negative decision the data accumulation is halted and the buffer pointers are reset. The system is ready to take data at the next Beam Cross Over. In case of a positive decision, the second level trigger phase is started. The second level trigger decision is taken 39  $\mu$ s after the BCO. In case of a negative decision the present data are aborted and the system will be ready to take data at the next BCO, having lost one BCO. In case of a positive second level trigger decision, a 3.5 ms deadtime is introduced in order to free the front end of the detectors and to prepare for the next event. The left part of Fig. 38 shows schematically the control of the synchronous phase of the data read-out.

This whole sequence is controlled by the Trigger Supervisor (TS) and for each detector by the Local Trigger Supervisor (LTS) and the Front End Freeing Controller (FEFC). The TS and LTS are pure hardware modules whereas the FEFC is in most cases software controlled.

### 13.3 The Main Readout Phase

Once the event is accepted by the second level trigger and the data are stored in local Front End Buffers (FEB), transfer of data from the local FEB to the Global Event Buffer (GEB) is done in several stages. The

FEB data, which typically contain data from one Fastbus module, are first transferred to the Crate Event Buffer by a Crate Processor, the Fastbus Intersegment Processor (FIP). During this process, data reduction (zero suppression), formatting and third level trigger processing are done.

The information in the many Crate Event Buffers is transferred to the single Multi Event Buffer (MEB) for each detector. The data in the MEB are duplicated in a Spy Event Buffer (SEB), which is accessible from the Equipment Computer of each detector to inspect the data.

A set of Local Event Supervisors (LES) handle the data transfer tasks during the main readout phase. During a first stage, some LES were General Purpose Fastbus Masters (GPM), the other LES being FIPs. In a second stage, all have been standardised on FIPs. The FIP and the GPM are Fastbus masters in which 32 and 16 bit architecture microprocessors<sup>(\*)</sup> are integrated. They support block transfers up to 20 Mbytes/s. These FIPs are connected to the data acquisition VAX cluster via Ethernet for remote login and program downloading. All processors are running the OS9 operating system.

Processing of trigger level three will be performed in the global third level processor in parallel with the transfer of data from FEB to MEB. A trigger level three rejection will abort the corresponding event data in the MEB and halt the event transfer of remaining blocklets of the event. At the end of data taking in 1990, this trigger level has not yet been enabled. The main readout phase is schematically shown on the central part of Fig. 38.

#### 13.4 Event Tagging and Data Storage

When the main readout phase is finished the data exist in 15 Multi Event Buffers - mostly one per detector. The event data are transferred from the Multi Event Buffers to the Global Event Buffer asynchronously to the other two readout phases. This task is handled by the Global Event Supervisor, which was composed of two GPM microprocessors for the control and monitoring and a Block Mover<sup>(\*\*)</sup> for the data transfer. The two GPMs were lately replaced by one FIP. The Global Event Buffer has a 2 Mbyte RAM Memory.

The main purpose of the fourth level tagging, implemented on three 3081/E emulators, is to identify the various types of events for fast physics analysis and background rejection. The results of the fourth level trigger process, added to the event data in the GEB, are transferred to the data acquisition computer for permanent storage on magnetic tape. The data acquisition computer<sup>(\*\*\*)</sup> situated on ground surface about 100 m from the detector, performs the data monitoring and data display prepared by the emulators. The event tagging phase of the readout is shown on the right part of Fig. 38.

---

(\*) Motorola 68020 and 68000.  
(\*\*) Kinetics Systems Corp.  
(\*\*\*) VAX 8700.

### 13.5 The VSAT readout

Due to the relatively high Bhabha trigger rate in VSAT a special readout procedure is followed. The VSAT events are stored locally and are all read out when a DELPHI event occurs. In case the VSAT buffer gets full (after 10–20 triggers), the readout is also performed. The procedure ensures that the recorded Bhabha events correspond to the live time of DELPHI.

## 14. SUMMARY

The DELPHI detector has been in operation since the short pilot run of LEP in August 1989. During the first 8.5 months of LEP operation until end of August 1990, about 135,000 hadronic  $Z^0$  events have been recorded. Trigger rates were typically 2.5 Hz at the highest luminosities around  $5 \times 10^{30} \text{ cm}^{-2} \text{ s}^{-1}$ , with a lifetime of about 95%. Several detectors have reached their design resolution and globally good performance has already permitted a rich harvest of physics results.

### Acknowledgements

This complex detector could only be constructed with the dedicated effort of many technical collaborators at the participating institutes and at CERN. We wish to express our gratitude and appreciation to all of them.

We also thank the funding agencies for the continued support for this project over the past eight years. The members of the LEP Division we wish to congratulate and thank for the speedy commissioning and successful operation of the collider and for the good collaboration with the experiments.

## REFERENCES

- [1] DELPHI Technical Proposal, CERN/LEPC 83–3 (1983);  
DELPHI Progress Report, CERN/LEPC 84–16 (1984).
- [2] Applied Superconductivity Conference (1984), vol. MAG–21, 490–3.
- [3] (a) V. Chabaud et al., CERN/EP 90–12 (1990), submitted to Nucl. Instr. & Meth. A.  
(b) Z.H. Dijkstra et al., Nucl. Instr. & Meth. A289 (1990) 400.
- [4] F. Hartjes et al., Nucl. Instr. & Meth. A256 (1987) 55.
- [5] C. Brand et al., IEEE Trans. Nucl. Sc. NS36 (1989) 122;  
C. Brand et al., Nucl. Instr. & Meth. A283 (1989) 567.
- [6] A. Amery et al., Nucl. Instr. & Meth. A283 (1989) 502;
- [7] L. Etienne et al., Nucl. Instr. & Meth. A241 (1985) 429;  
C. De Clercq et al., Nucl. Instr. & Meth. A243 (1986) 77;  
E. Daubie et al., Nucl. Instr. & Meth. A252 (1986) 435;  
E. Daubie et al., Nucl. Instr. & Meth. A273 (1988) 553;  
F. Stichelbaut et al., Nucl. Instr. & Meth. A283 (1989) 792.
- [8] Balder, Centre for Industrial Research Oslo, Int. Rep.
- [9] A. Ferrer et al., Anales de Fisicas B83 (1987) 291;  
P. Allen et al., Nucl. Instr. & Meth. A277 (1989) 347;  
J.M. Benlloch et al., Nucl. Instr. & Meth. A290 (1990) 327.  
J.M. Benlloch et al., Nucl. Instr. & Meth. A292 (1990) 319.
- [10] H.G. Fischer and O. Ullaland, IEEE Trans. Sci. NS–27 (1980) 38;  
M. Berggren et al., Nucl. Instr. & Meth. 225 (1984) 477;  
A. Cattai et al., Nucl. Instr. & Meth. A235 (1985) 310;  
V. Gracco et al., Nucl. Instr. & Meth. A252 (1986) 573–578;  
F.L. Navarria et al., Nucl. Instr. & Meth. A257 (1987) 499;  
H.G. Fischer et al., Nucl. Instr. & Meth. A265 (1988) 218.
- [11] ALEPH: A detector for electron–positron annihilations at LEP, CERN–EP/90–25, submitted to  
Nucl. Instr. & Meth.
- [12] (a) P. Checchia et al., Nucl. Instr. & Meth. A248 (1986) 317;  
(b) G. Barichello et al., Nucl. Instr. & Meth. A254 (1987) 111;  
(c) P. Checchia et al., Nucl. Instr. & Meth. A275 (1989) 49.
- [13] M. Ellila, Acta Polytechnica Scandinavica, Appl. Phys. Series 159 (1988);  
N.A. Filatova, Nucl. Instr. & Meth. A243 (1986) 91.  
G.D. Alekseev et al, Nucl. Instr. & Meth. A269 (1988) 652.
- [14] (a) J. Séguinot and T. Ypsilantis, Nucl. Instr. & Meth. 142 (1977) 377;  
R. Arnold et al., Nucl. Instr. & Meth. A270 (1988) 255.  
(b) D. Fraissard et al., Nucl. Instr. & Meth. A252 (1986) 524;  
F. Hahn et al., Nucl. Instr. & Meth. A283 (1989) 686.  
(c) G. Kalkanis et al., Nucl. Instr. & Meth. A283 (1989) 37.  
(d) R. Arnold et al., Nucl. Instr. & Meth. A252 (1986) 188;  
D. Bloch et al., Nucl. Instr. & Meth. A273 (1988) 847;  
G. Van Apeldoorn et al., Nucl. Instr. & Meth. A283 (1989) 767.  
(e) P. Baillon et al., Nucl. Instr. & Meth. A277 (1989) 338;  
S. Walles, Particle World 1 (1989) 62.

REFERENCES (Cont'd)

- [15] W. Dulinski et al., Nucl. Instr. & Meth. A252 (1986) 418;  
P. Beltran et al., Proc. of Int. Symp. on Position Detectors in High-Energy Physics, D1, 13-88-172, Dubna (1987) 286.
- [16] R.C.A. Brown, IEEE Trans. Nucl. Sci., Vol. 36 (1988) 71.
- [17] T. Adye et al., Computer Physics Communications 57 (1989) 466.
- [18] (a) S. Quinton et al., Int. Conf. on the Impact of Digital Microelectronics and Microprocessors on Particle Physics, Trieste (1988) 20;  
S. Quinton et al., IEEE Trans. Nucl. Sci. (1989) 390.  
(b) G. Darbo and B.W. Heck, IEEE Trans. Nucl. Sci 34,1 (1987) 227 and Nucl. Instr. & Meth. A257 (1987) 567;  
G. Darbo et al., to be publ. in IEEE Trans. Nucl. Sci. (1990).



**TABLE CAPTIONS**

- TABLE 1      Specifications and performance of tracking detectors.
- TABLE 2      Specifications and performance of calorimeters.
- TABLE 3      Summary of the second level trigger components. Logical "OR" and "AND" are indicated by + and \* respectively. The multiplicity requirement is also shown.

TABLE 1

	Acceptance			No-points along track	Resolution per point ( $\sigma$ , mm)		Comments
	R(cm)	z  (cm)	$\theta$ ( $^\circ$ )				
Vertex Det.	9/11	12	37-143	2	R $\phi$ : 0.007	(a)	2-track sep.: 100 $\mu$ m
IDC: jet-s.	11.8-22.3	40	17-163	24	R $\phi$ : 0.11	(a)	
trigger-s.	23-28	$\leq 50$	30-150	5	z: < 1	(a)	
TPC	35-111	$\leq 134$	20-160(i)	16 192	R $\phi$ : 0.23	(a)	(i) for $\geq 3$ pad rows. 192 dE/dx samples $\sigma$ (dE/dx) = 6.2% (a) 5.5% (b)
OD	198-206	$\leq 232$	43-137	5 * R $\phi$ 3 * z	R $\phi$ : 0.11	(a)	Fast z-information
B-Muon	~ 445 ~485	$\leq 185$	52-138	2 (+ 2)	z: 44	(a)	
F-CHA	30-103	155-165	11-33	2 * (x,u,v)	R $\phi$ : 1.5	(b)	2 layers, sep. by 20 cm Fe
F-CHB	53-195	267-283	11-35	4 * (x,u,v)	z: 10	(b)	
F-Muon	70-460	463 500	9-43	(2 + 2)*(x, y)	x,u,v: 0.3	(a)	2 layers, sep. by 20 cm Fe
SAT Tracker	10-23.8/27.6	203,216,230	2.5-6.8	2(3)	x, y: 1.0	(b)	
					R: 0.3	(a)	
					$\phi$ : 0.5 $^\circ$		

- (a) Measured at LEP.
- (b) Measured in test beam.

TABLE 2

	Acceptance		Readout-Granularity	Depth	Shower Resolution ( $\sigma_E/E$ ; %)	Comments
	R(cm)	z  (cm)				
HPC	208-260	$\leq 254$	$\phi \sim 1^\circ$ ; z: 4 mm R: 9 samples	18 $X_0$	$23\sqrt{E} + 1.1^{(a)}$	(a) In test beam Eff. for m.i.p.'s > 90%
F-EMC	46-240	284-340	$\phi$ : $1^\circ$ ; $\theta$ : $1^\circ$	20 $X_0$	$[(0.35 + 5\sqrt{E})^2 + (6/E)^2]^{1/2}$ 4% at 45.6 GeV	(a) In test beam
SAT	10-36	233-285	$\phi$ : $7.5^\circ$ , $15^\circ$ $\theta$ : $0.7^\circ$	28 $X_0$	$[1.22 + 11.4^2/E]^{1/2} + 2.3$	
VSAT	-6-9 ( x )	770	5-7 mrad	24 $X_0$	5% at 45.6 GeV	12 W/Si-layers $3 \times 5 \times 10 \text{ cm}^3$
HCAL	B: 320-479 FW: 65-460	< 380 340-489	$\phi$ : $3.75^\circ$ $\theta$ : $3.0^\circ$ (B), $2.6^\circ$ (FW)	6 $\lambda$	120 $\sqrt{E}$	$\sigma_E$ from TPC inform.

TABLE 3

<p style="text-align: center;"><b>BARREL REGION</b></p> <ul style="list-style-type: none"><li>- HPC <math>\geq 2</math></li><li>- TOF <math>\geq 2</math></li><li>- (HPC <math>\geq 1</math>) * (TOF <math>\geq 1</math>)</li><li>- (OD <math>\geq 1</math>) * (TOF <math>\geq 1</math>)</li><li>- ID * OD (back to back octants)</li><li>- (ID * OD) single track with <math>p_T \geq 1.6</math> GeV/c</li><li>- (ID + OD) * TPC single track with <math>p_T \geq 0.5</math> GeV/c</li></ul>
<p style="text-align: center;"><b>FORWARD/BACKWARD REGION</b></p> <ul style="list-style-type: none"><li>- (Muon forward) * (Muon backward)</li><li>- Muon forward/backward single arm</li><li>- FEMC <math>\geq 1</math></li><li>- Majority 2 of the following components: HOF, FEMC, FCA/B, ID * OD</li></ul>
<p style="text-align: center;"><b>LUMINOSITY MONITOR</b></p> <ul style="list-style-type: none"><li>- "Bhabha" = (SAT forward) * (SAT backward)</li><li>- Single arm SAT</li><li>- "Very forward Bhabha" = (VSAT forward) * (VSAT backward)</li><li>- Single arm VSAT</li></ul>

## FIGURE CAPTIONS

- FIGURE 1 Examples of  $Z^0$  events, as seen on the DELPHI interactive analysis display. The  $\mu\mu\gamma$ -event shows the sensitivity of both the electromagnetic and the hadron calorimeters to muons.
- FIGURE 2 Perspective view of the DELPHI detector. 1 = Micro-Vertex Detector. 2 = Inner Detector. 3 = Time Projection Chamber (TPC). 4 = Barrel Ring Imaging Cherenkov Counter (RICH). 5 = Outer Detector. 6 = High Density Projection Chamber (HPC). 7 = Superconducting Solenoid. 8 = Time of Flight Counters (TOF). 9 = Hadron Calorimeter. 10 = Barrel Muon Chambers. 11 = Forward Chamber A. 12 = Small Angle Tagger (SAT) = Luminosity Monitor. 13 = Forward RICH. 14 = Forward Chamber B. 15 = Forward Electromagnetic Calorimeter. 16 = Forward Muon Chambers. 17 = Forward Scintillator Hodoscope. The Very Small Angle Tagger (VSAT) falls outside the view.
- FIGURE 3 Longitudinal (a) and transverse section (b) through the DELPHI detector.
- FIGURE 4 Magnetic Field with optimized compensation currents ( $I_A = -850$  A,  $I_C = -650$  A;  $I_{MAIN} = 5000$  A): (a) Axial component; (b) Radial component, as function of longitudinal coordinate  $z$  and radius  $R$ .
- FIGURE 5 Micro Vertex Detector: (a) Sketch of assembly in two shells with 10% azimuthal overlap between 15 degree sectors. (b) Close-up showing connection of strip detector (left) to VLSI preamplifier chips.
- FIGURE 6 Event display showing track fitting through Microvertex, Inner Detector and innermost section of TPC. In the Microvertex, some tracks produce a third hit in the overlap regions.
- FIGURE 7 Micro Vertex Detector: (a) Measurement of the radial gap to the Inner Detector. Variation over 10 days:  $\sigma = 0.64$   $\mu\text{m}$ . (b) Preliminary  $R\phi$ -resolution obtained from tracks producing 4 hits in the overlap regions:  $\text{fwhm}/2.35 = 7$   $\mu\text{m}$ .
- FIGURE 8 Inner Detector: (a) 90° cross section; (b) Distribution of  $R\phi$ -residuals per wire in jet-chamber section.
- FIGURE 9 Time Projection Chamber (TPC): One read-out plane formed by six sectors, each with 16 circular pad rows and 192 anode wires.
- FIGURE 10 Laser calibration system for TPC. Each laser, one per sector, produces three photo-ionization tracks.
- FIGURE 11 Results from the TPC: (a)  $K^0$  reconstruction, (b)  $\Lambda$ -peak in the proton pion mass spectrum, (c)  $dE/dx$ -resolution in the low momentum region.

FIGURE CAPTIONS (Cont'd)

- FIGURE 12 Outer Detector: (a) Shape and arrangement of detector modules. (b) Distribution of residuals in  $R\phi$ :  $\text{fwhm}/2.35 = 86 \mu\text{m}$ , corresponding to a resolution of  $110 \mu\text{m}$  per layer; (c) Distribution of  $z$ -coordinates relative to the track extrapolation from the TPC:  $\text{fwhm}/2.35 = 4.4 \text{ cm}$ .
- FIGURE 13 Barrel muon chambers: (a) Cross section through a drift tube. (b) Distribution of residuals in  $R\phi$  on extrapolated dimuon tracks:  $\sigma_{R\phi} = 4 \text{ mm}$ . (c) Residual distribution in  $z$ :  $\sigma_z \sim 2.5 \text{ cm}$ . These errors include the extrapolation error.
- FIGURE 14 Forward Chamber A. (a) Cross section through one staggered double layer. (b) Fit residuals of drift distances as measured in all six layers:  $\sigma = 225 \mu\text{m}$ .
- FIGURE 15 Forward Chamber B: (a) General layout. (b) Cross section. (c) Plot of residuals as obtained from track fits for parallel halo muons. The resultant resolution of  $250 \mu\text{m}$  per plane leads to a total chamber resolution of about  $120 \mu\text{m}$  in  $x$  and  $y$ .
- FIGURE 16 Forward Muon Chambers: (a) Cross section through drift tube. (b) Residuals for fitted tracks of halo muons registered in the four detector layers, separately for end-caps A and C, including drift time and delay line measurements and errors due to the magnetic stray field:  $\sigma \sim 3 \text{ mm}$ .
- FIGURE 17 The Tracker of the Small Angle Tagger: Radial distance to track extrapolations pointing to high energy showers in the calorimeter section; nearest tracker hit within  $\phi$  sector of  $10^\circ$ .
- FIGURE 18 Combined Tracking: Momentum resolution for muons of  $45.6 \text{ GeV}$ . (a) Barrel region, using information from ID, TPC and OD. (c) Forward region,  $\theta = 18\text{--}32^\circ$ , using ID, TPC and Chamber B.
- FIGURE 19 Time of Flight Counters: Construction details of a single counter.
- FIGURE 20 Forward Scintillators: Layout of a  $90^\circ$  section of the hodoscope in one end-cap.
- FIGURE 21 High Density Projection Chamber (HPC). (a) Design details of a module. (b) Pad layout of a read-out chamber, providing 9 samples in  $R$ .
- FIGURE 22 HPC samples obtained from a  $45 \text{ GeV}$  electron shower (a) and a multi-shower event (b).
- FIGURE 23 HPC: (a)  $\pi^0$  reconstruction. (b) Track angles for Bhabha events as measured in the HPC; electrons and positrons are well separated.
- FIGURE 24 Layout of Forward Electromagnetic Calorimeter.
- FIGURE 25 Forward Electromagnetic Calorimeter. Energy deposition (a) and difference between the polar angles of electrons and positrons (b) as measured in Bhabha events.
- FIGURE 26 Small Angle Tagger (SAT): (a) Segmentation of read-out. (b) Lead mask used on one arm.

FIGURE CAPTIONS (Cont'd)

- FIGURE 27 Scatter plot of energies of shower coincidences as measured in both arms of the SAT.
- FIGURE 28 Very Small Angle Tagger: (a) Scatter plot for Bhabha triggers in diagonally opposite modules. (b) Projection on one axis of scatter plot (a) after circular energy cut of 37 GeV around Bhabha peak. (c), (d) show transverse profiles for the first x-plane and the y-plane, obtained by aligning the strips with the largest pulseheights.
- FIGURE 29 Tower structure of read-out for the hadron calorimeter.
- FIGURE 30 Hadron Calorimeter: (a) Average energy deposition in the calorimeter versus track momentum as measured by TPC. (b) Comparison of energy deposition of single tracks in hadron calorimeter and TPC after scaling by the square root of the TPC energy. (c) Total energy deposition in hadron calorimeter for hadronic events and (d) for background events, as defined by off-line event selection.
- FIGURE 31 Constructional details of the Barrel-RICH. (a) Longitudinal cross section. (b) Details of the readout chamber.
- FIGURE 32 Rings obtained with the liquid radiator ( $C_6F_{14}$ ) of the Barrel RICH. (a)–(d) show projections onto a plane perpendicular to the track direction: (a) From a single high momentum particle. (b) Superposition of photons from 246 cosmic muons. (c) Photons from 111 muon pairs. (d) Photons from many particles in hadronic events with  $p > 6 \text{ GeV}/c$  (central ionization due to  $dE/dx$  suppressed and total reflection cut at 0.7 rad). (e) Radial projection from distribution (c): 8.6 photons per track, error on Cherenkov angle = 18 mrad r.m.s. (f) Radial projection of distribution (d): error of Cherenkov angle = 18 mrad r.m.s.
- FIGURE 33 Forward RICH. (a) Layout of half an end-cap: A = liquid radiators, B = drift box, C = MWPC, D = gas radiator volume, E = mirrors. (b) Drift box covering a  $30^\circ$  sector. (c) Detail of readout chamber showing the crossed photon screens.
- FIGURE 34 Forward RICH. Superposition of photons obtained with  $C_5F_{12}$  as gas radiator in a test beam. Distinct peaks are observed for K's and  $\pi$ 's.
- FIGURE 35 Slow Controls System. Diagram showing the software structure for one detector's high voltage and temperature monitoring.
- FIGURE 36 Comparison of the hit pattern of the contiguity trigger (b) with the actual hit pattern of the TPC read-out (a).
- FIGURE 37 Trigger efficiency for hadronic events as function of the polar angle of the sphericity axis.

**FIGURE CAPTIONS (Cont'd)**

**FIGURE 38**     The architecture of the read-out system. The schematics displays the trigger processes and the control of the read-out phases by the Trigger Supervisor, Event Supervisor and Global Event Controller.



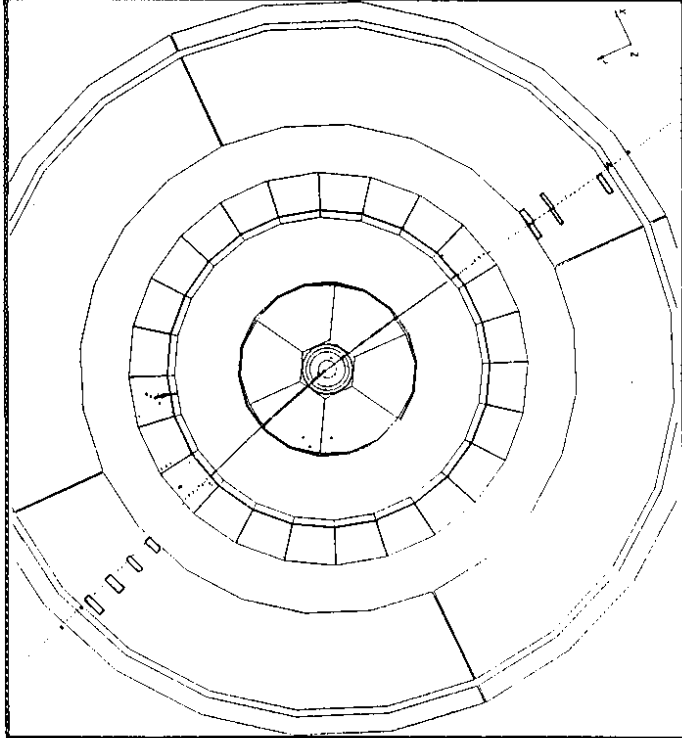
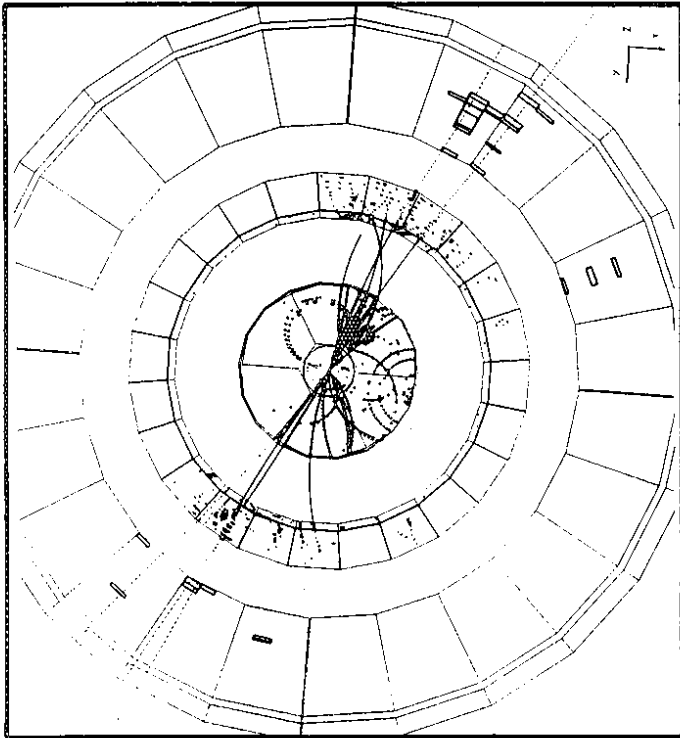
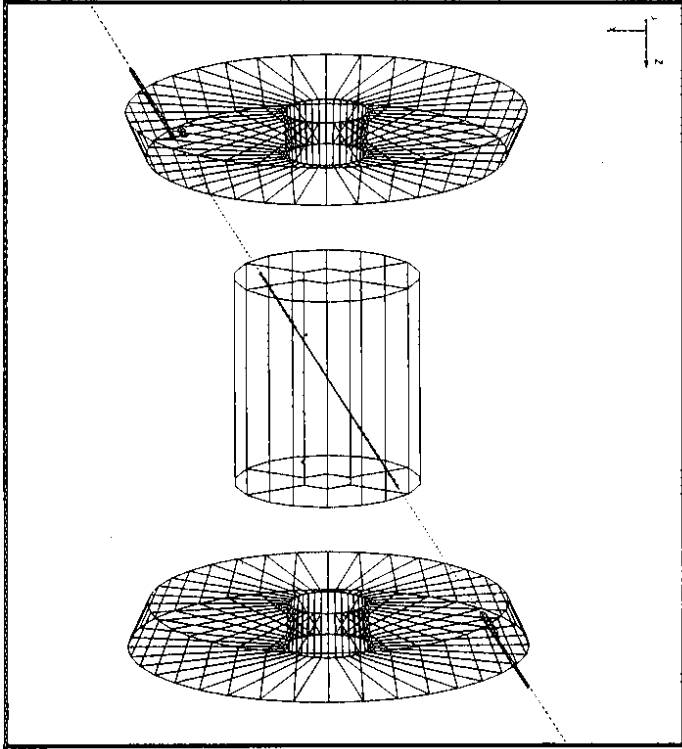
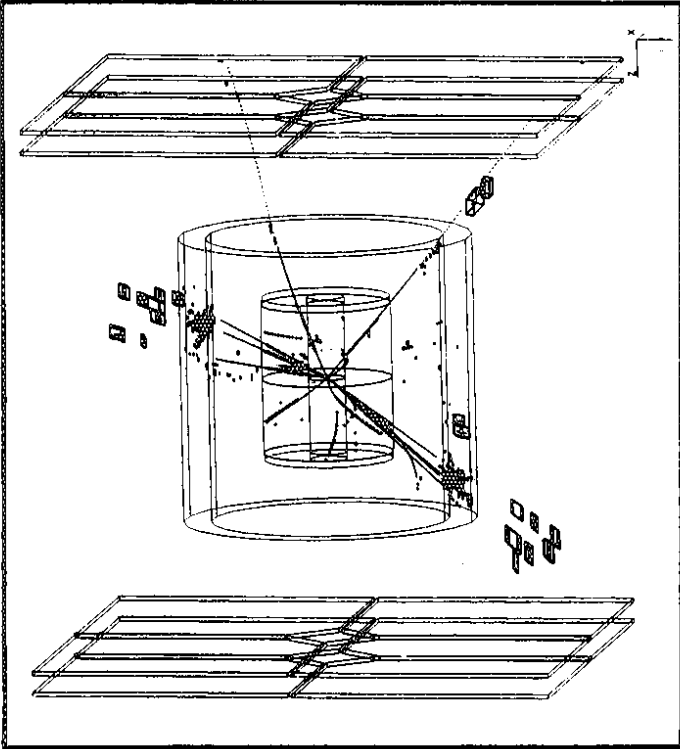


Fig. 1

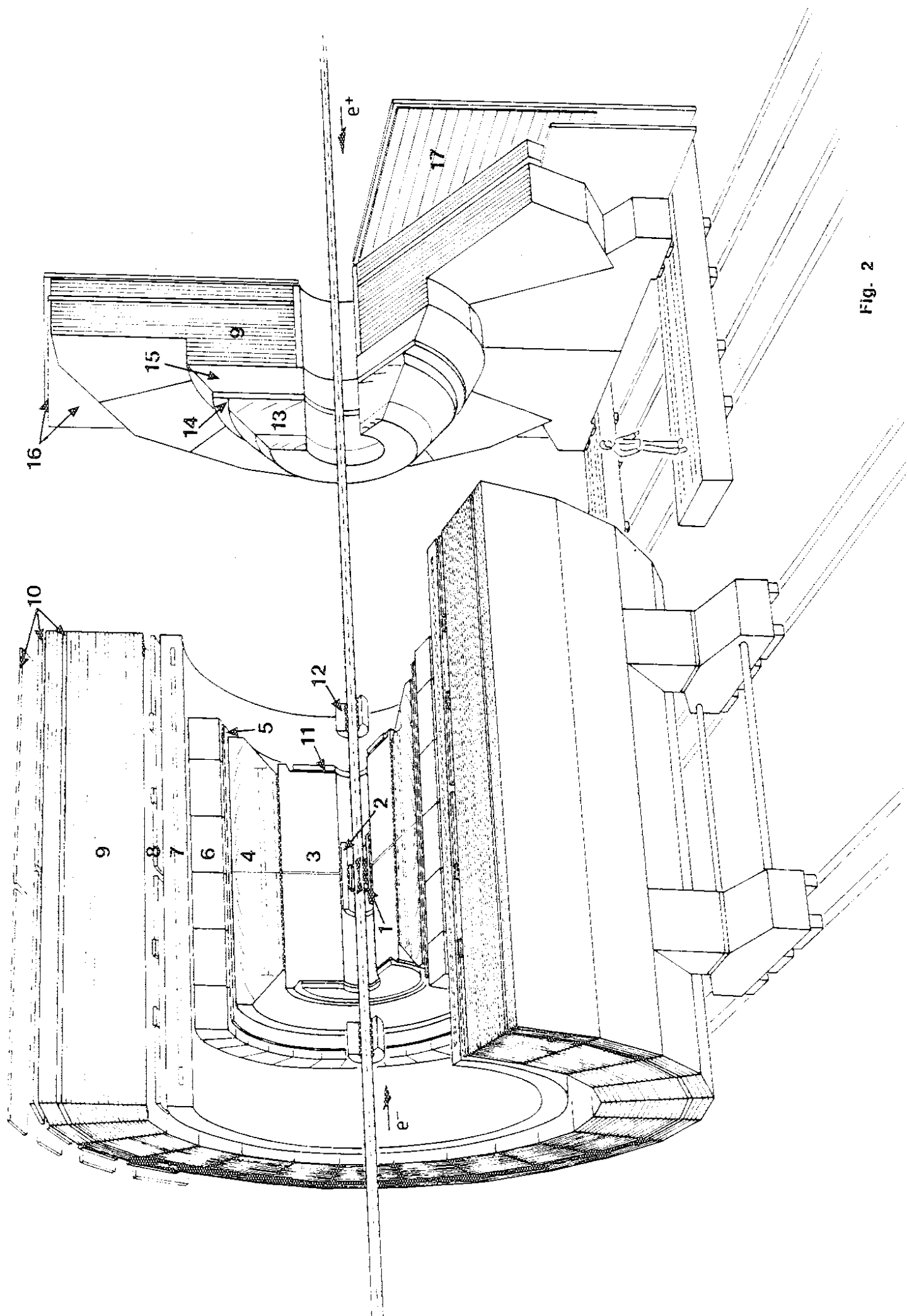
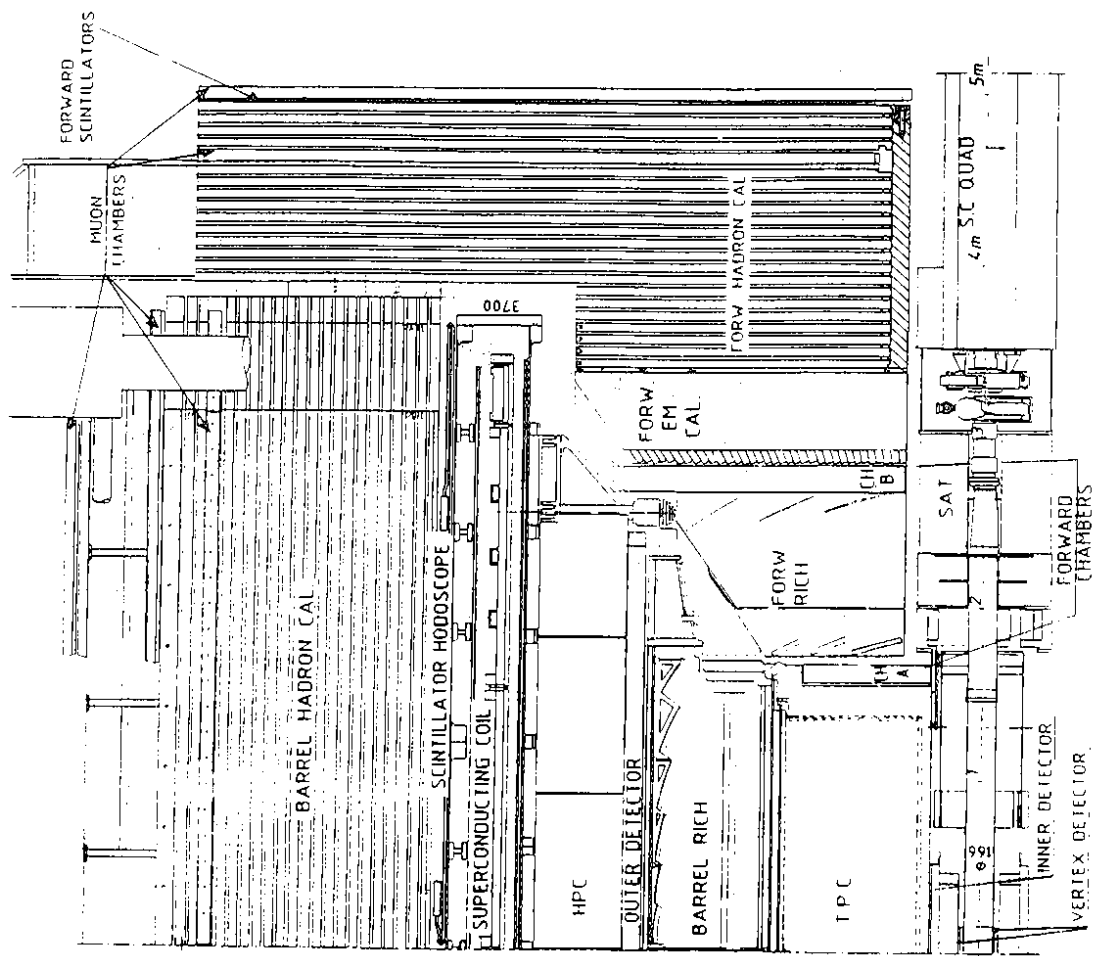
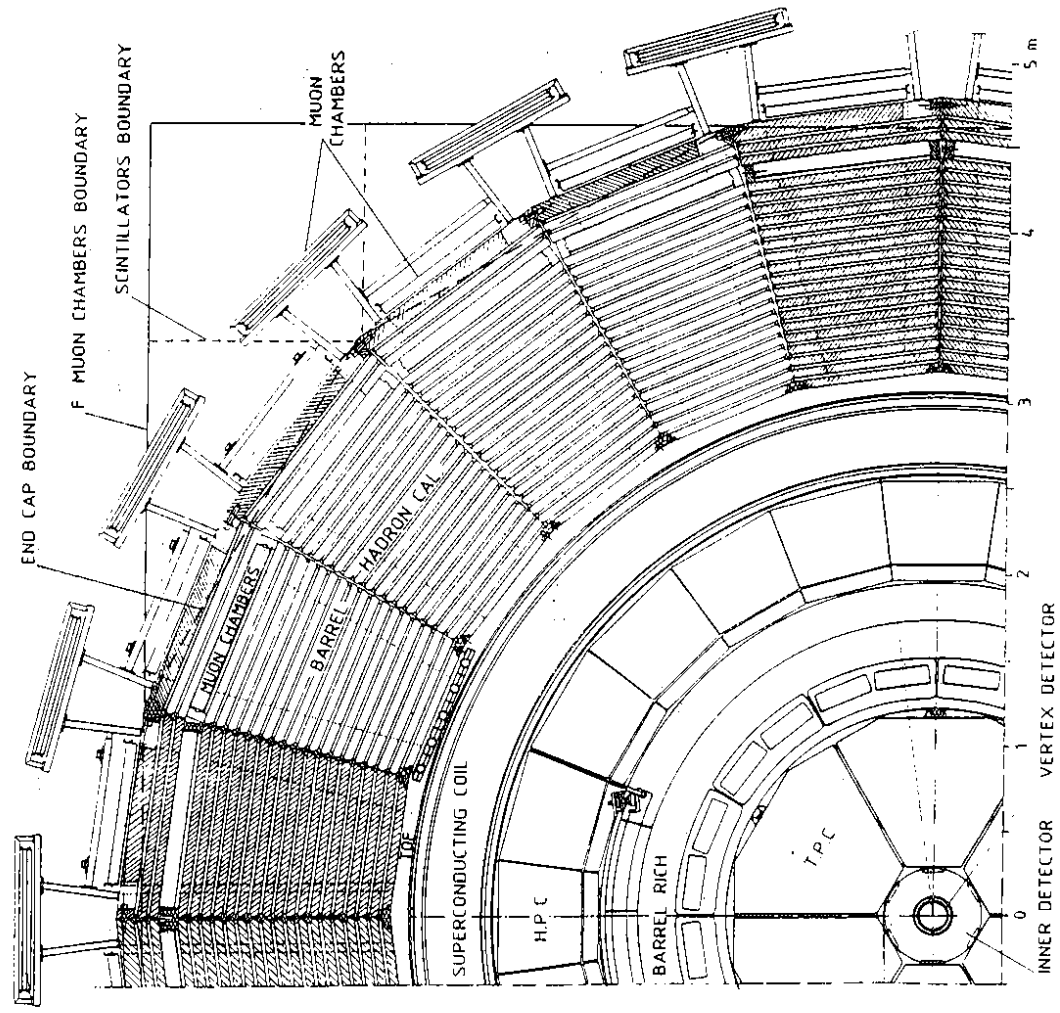


Fig. 2



(a)



(b)

Fig. 3

# DELPHI SOLENOID

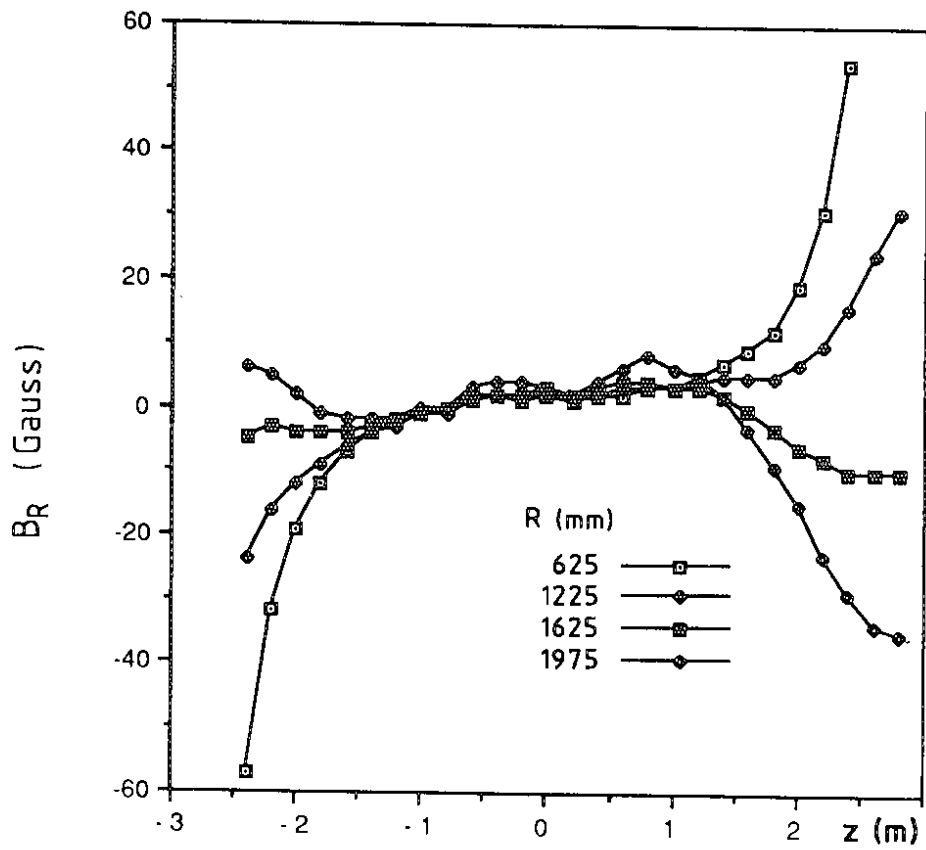
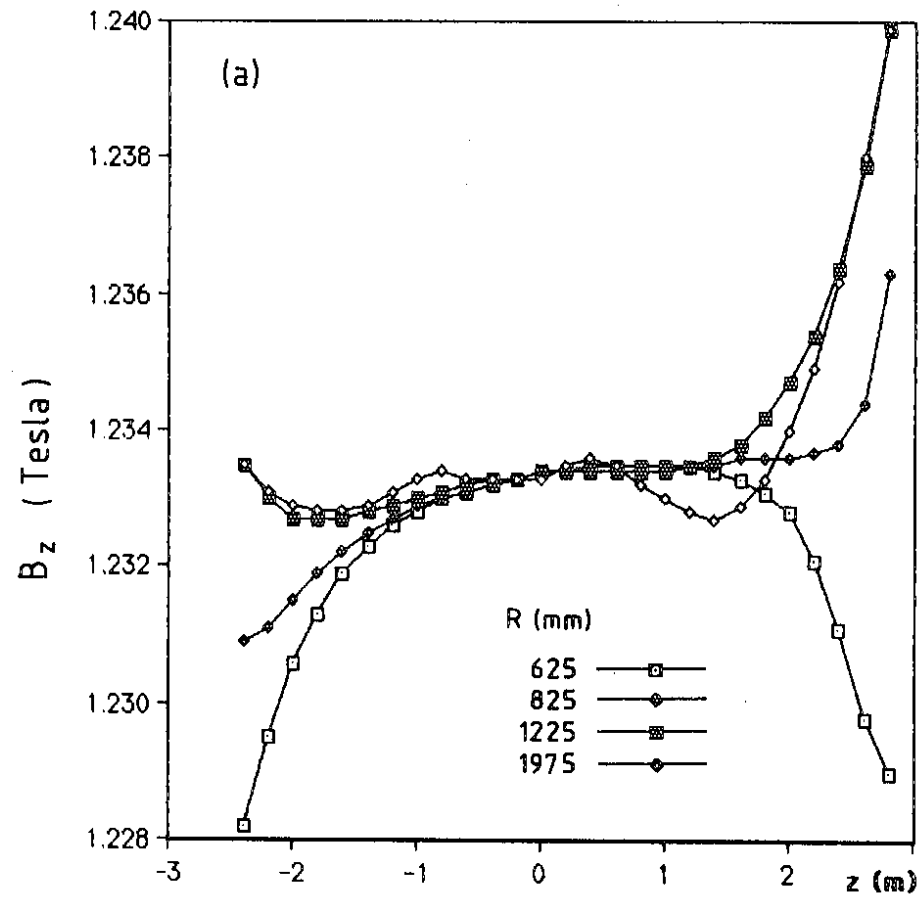


Fig. 4

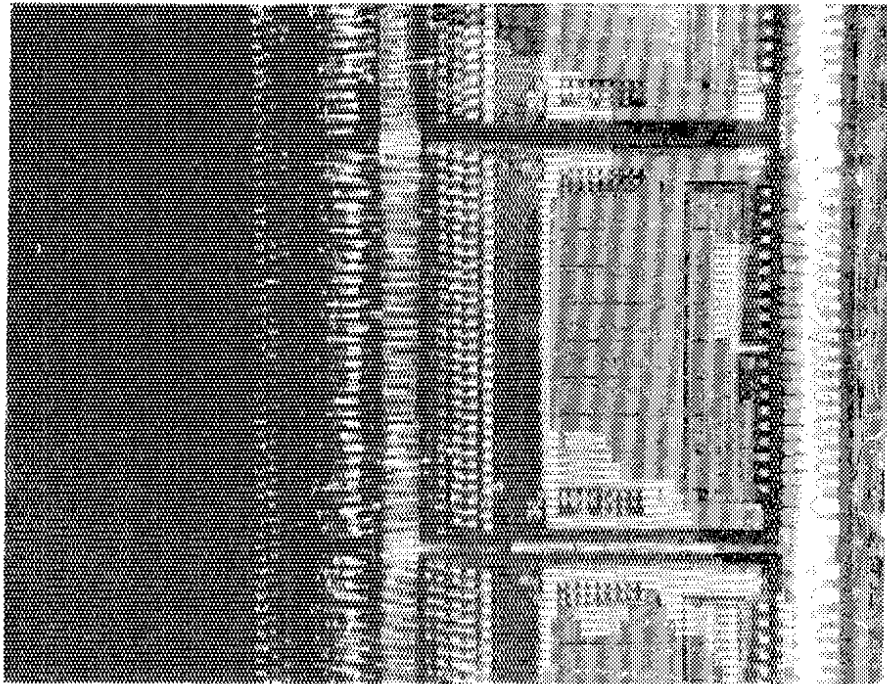
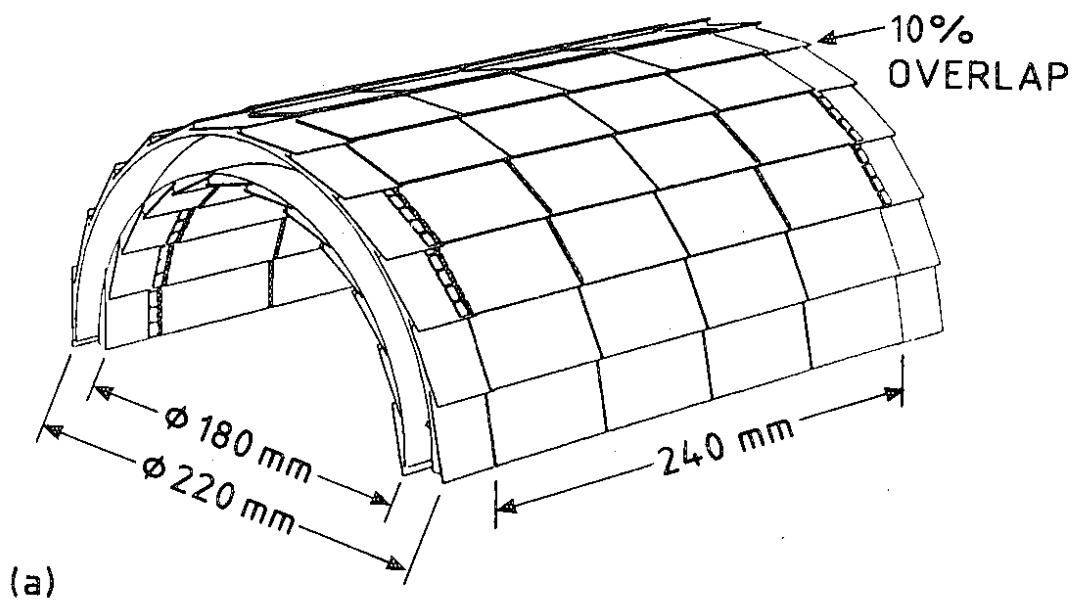


Fig. 5

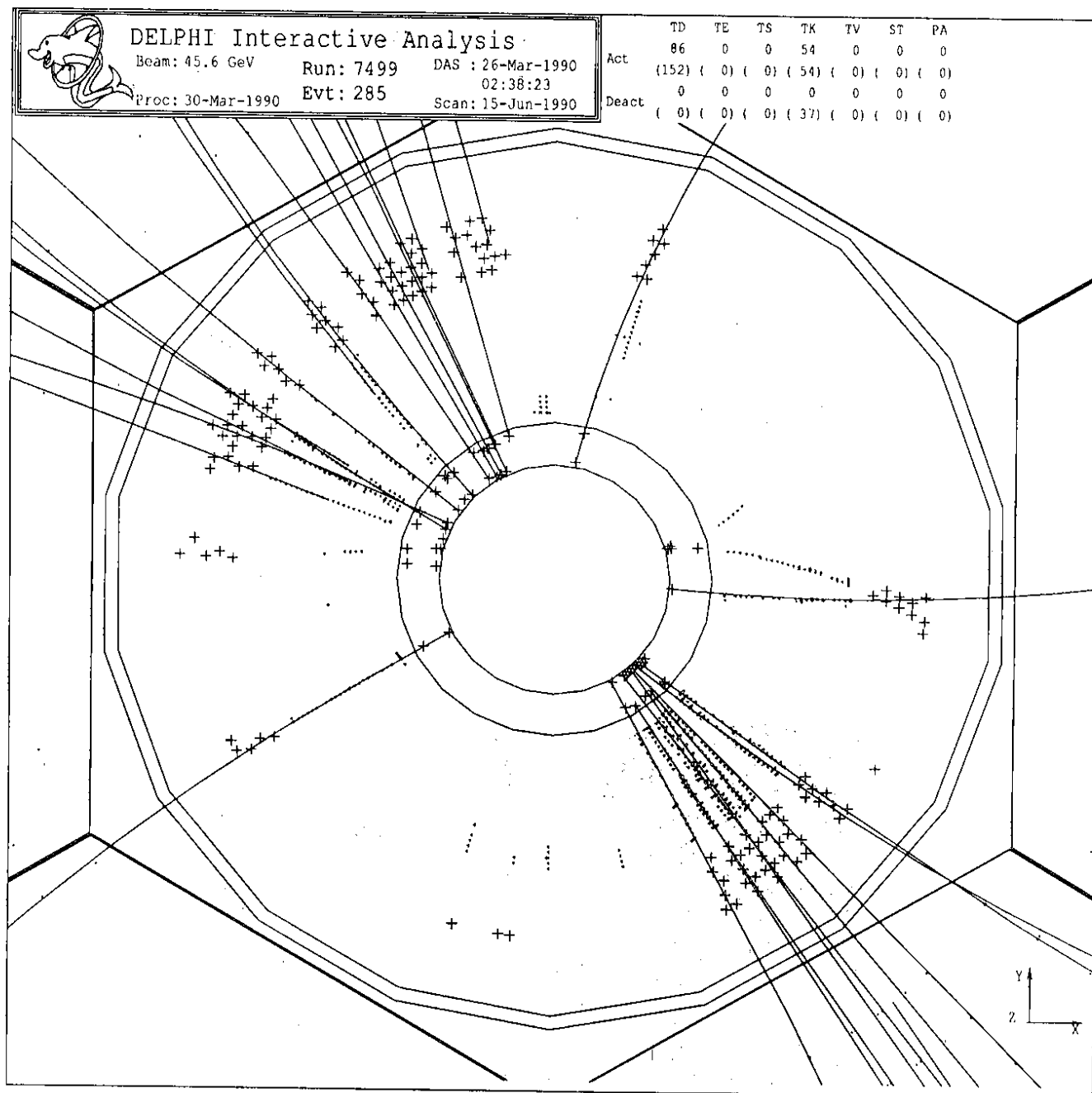


Fig. 6

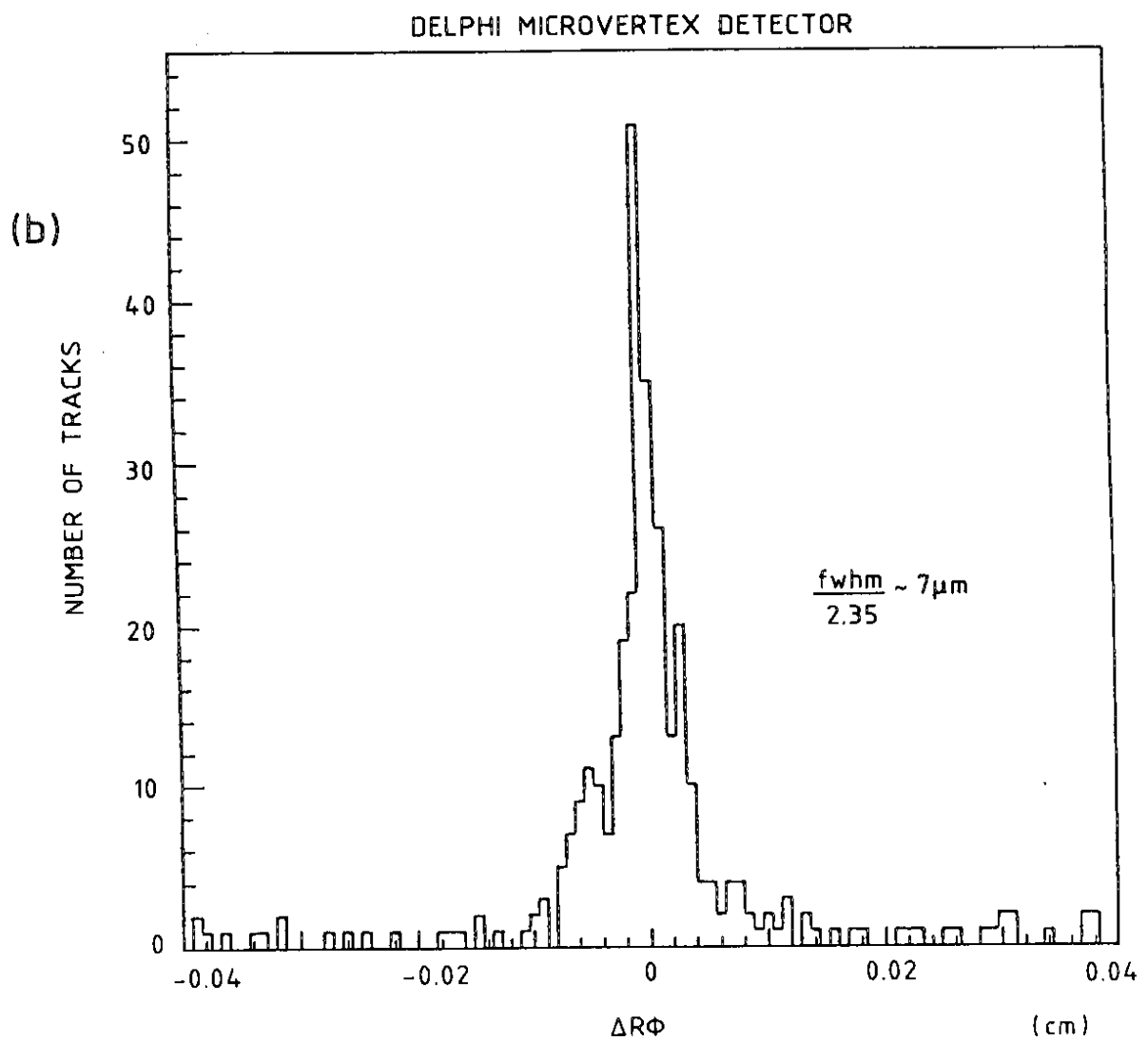
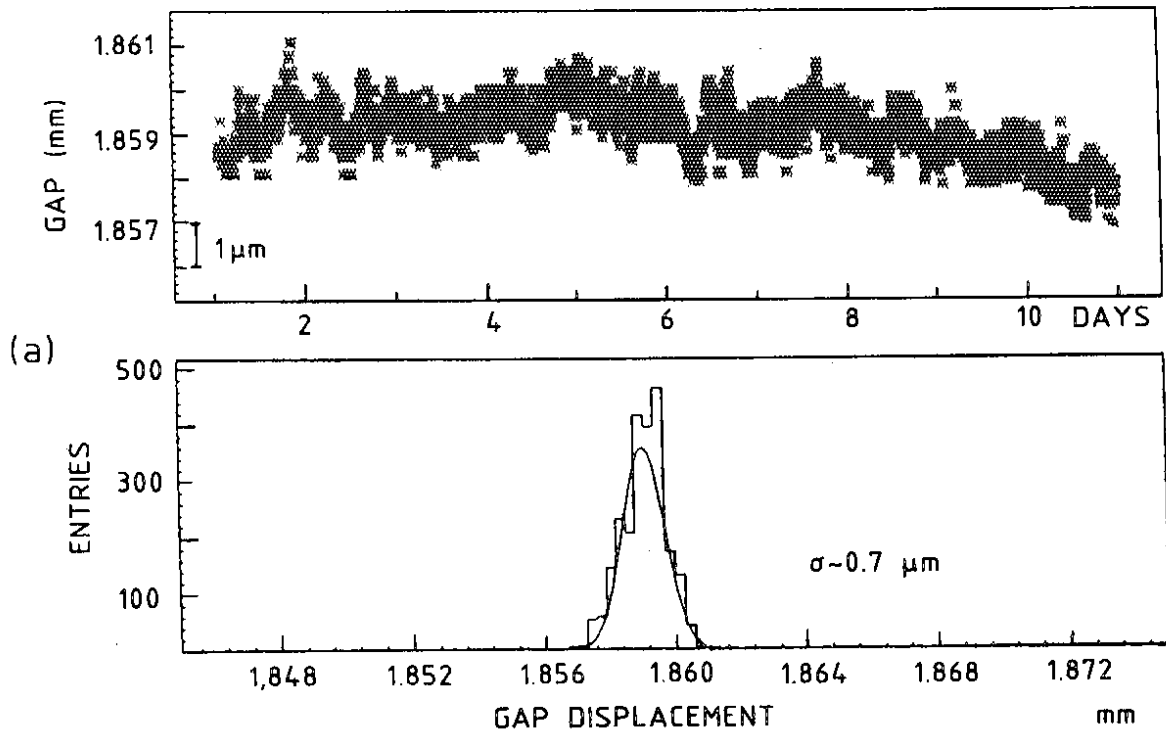
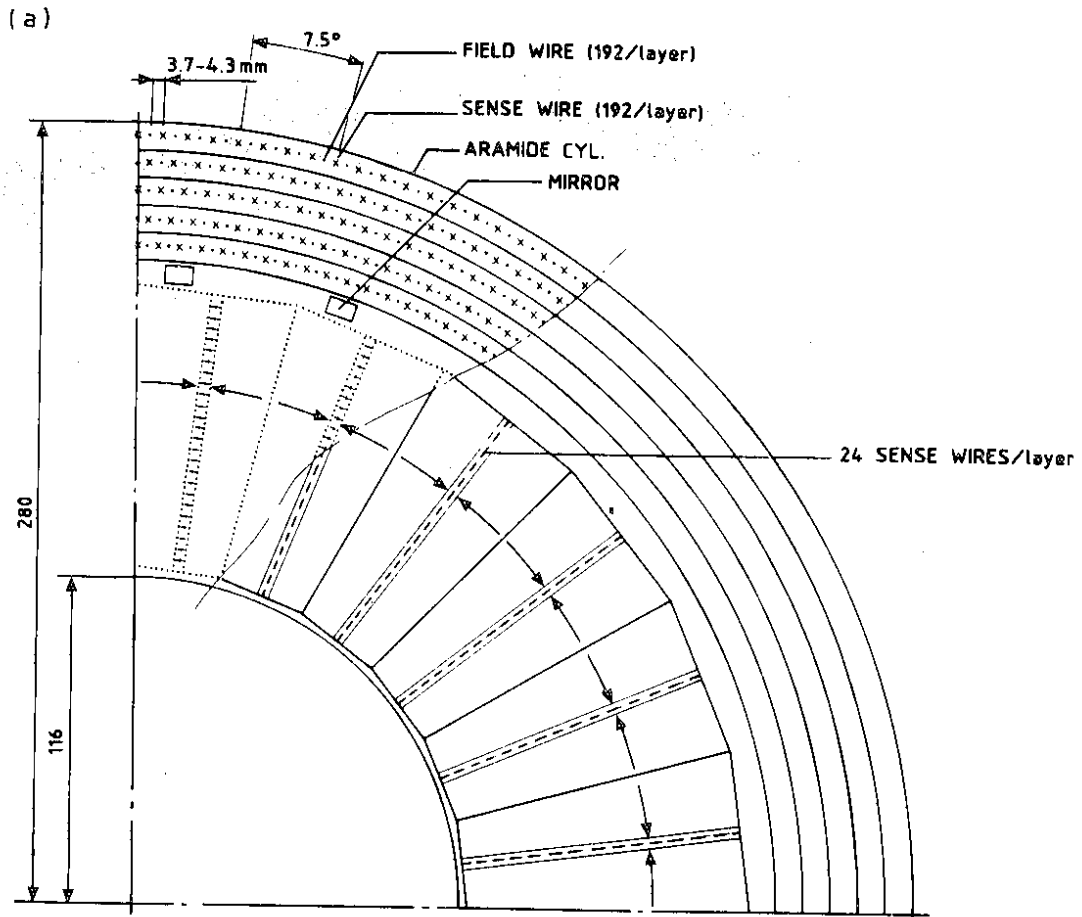


Fig. 7



INNER DETECTOR

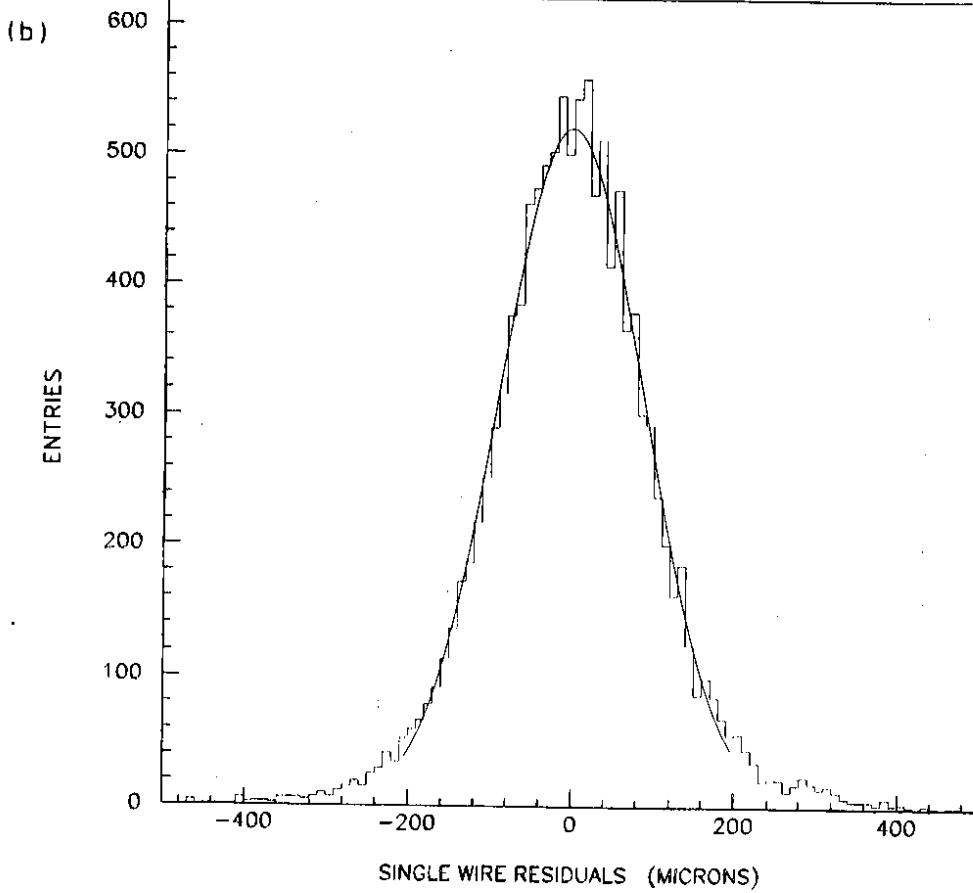


Fig. 8



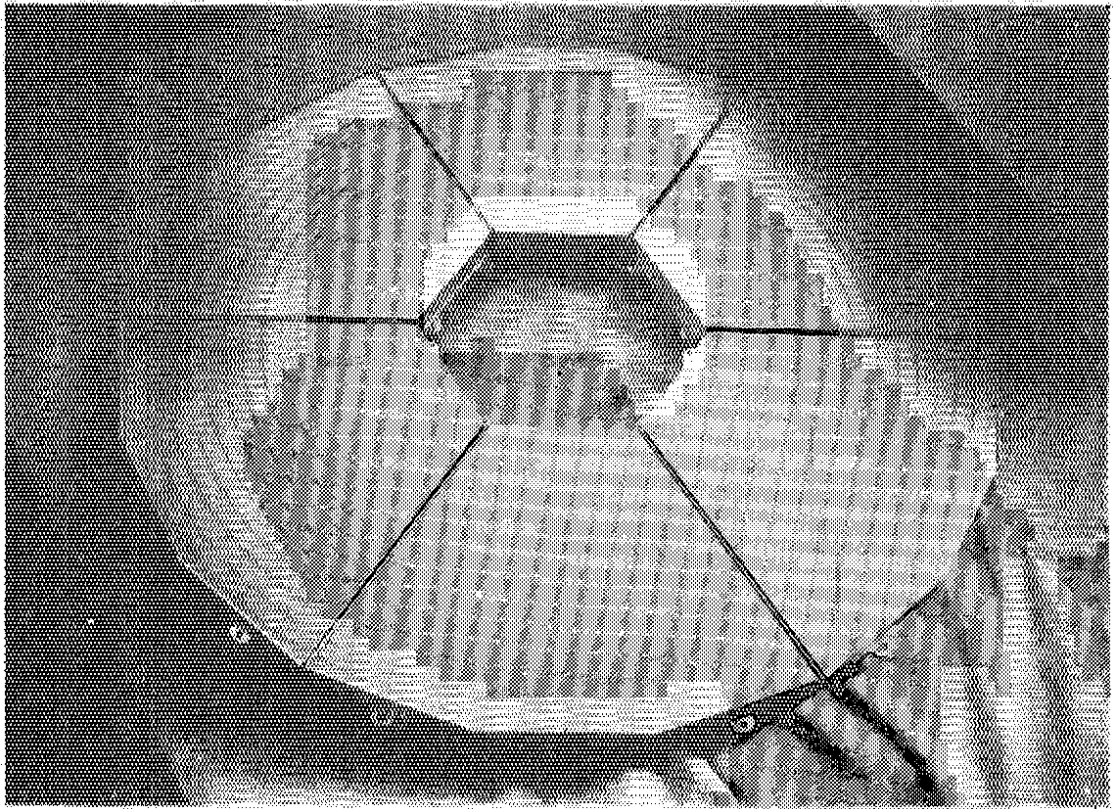


Fig. 9

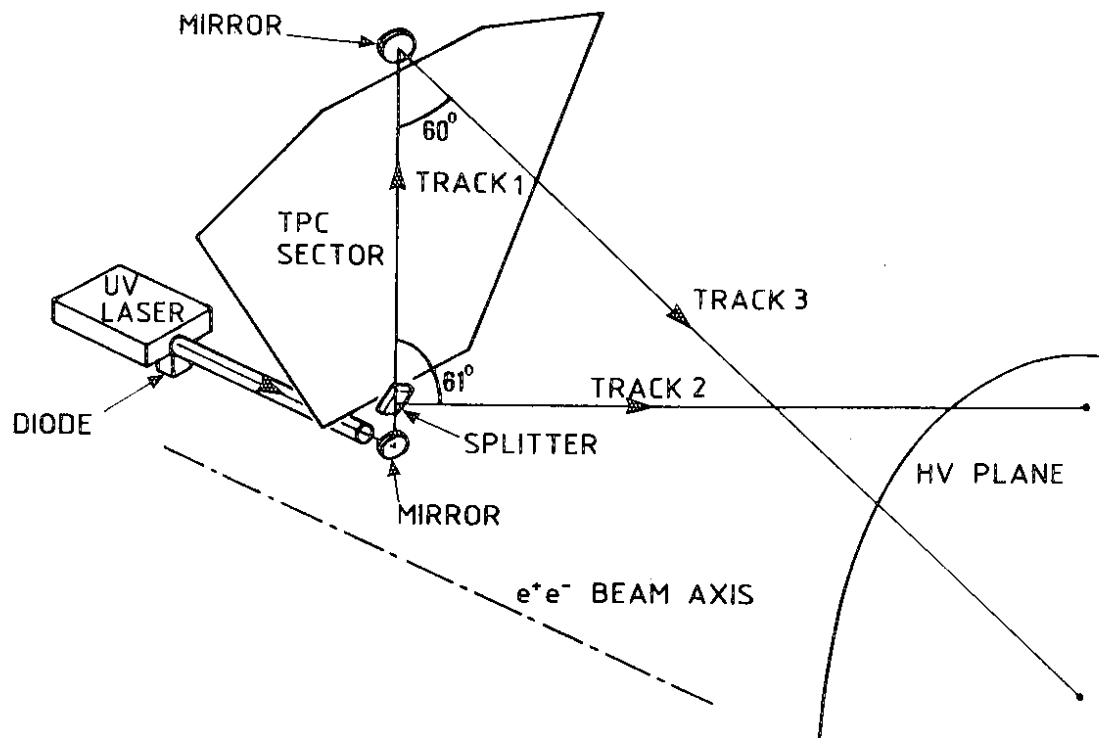
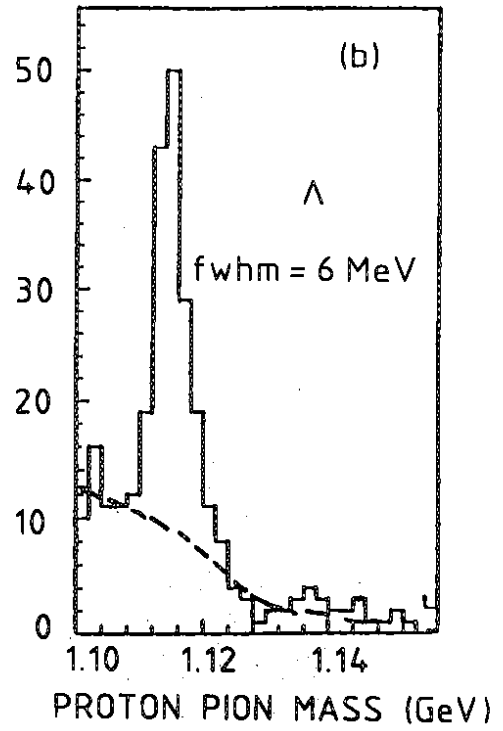
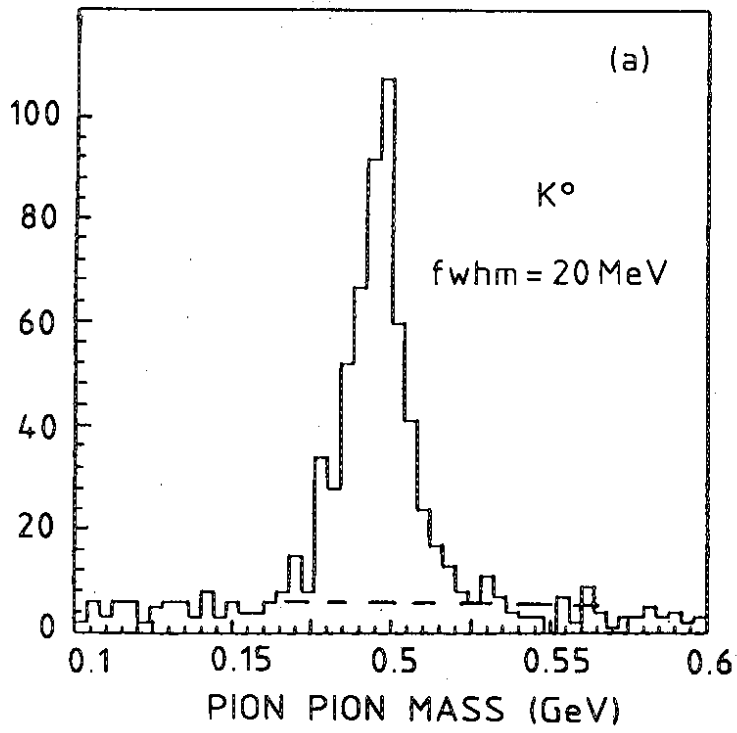


Fig. 10

DELPHI TPC



DELPHI TPC

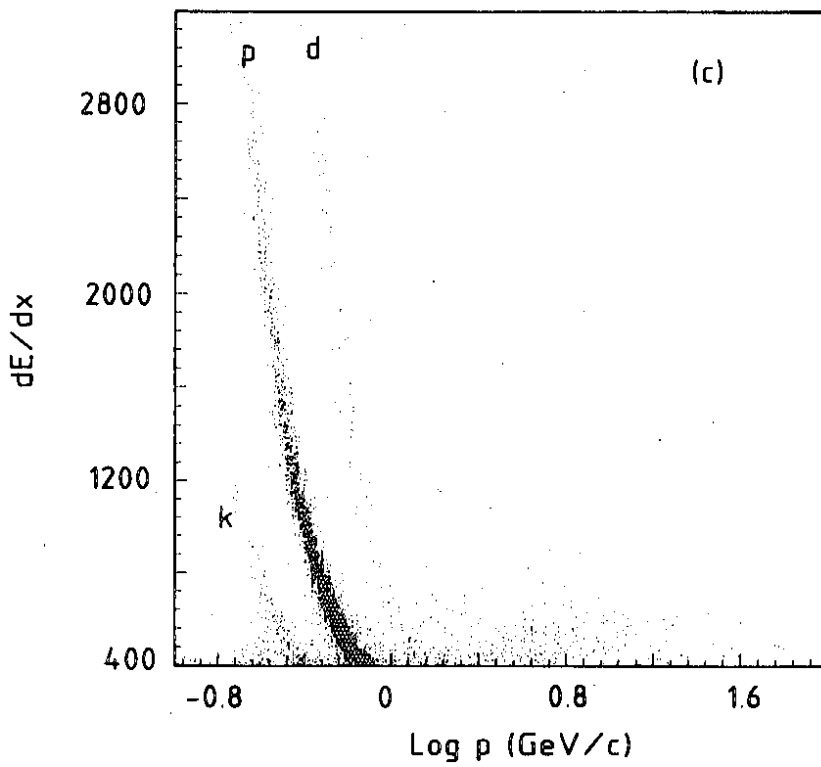


Fig. 11

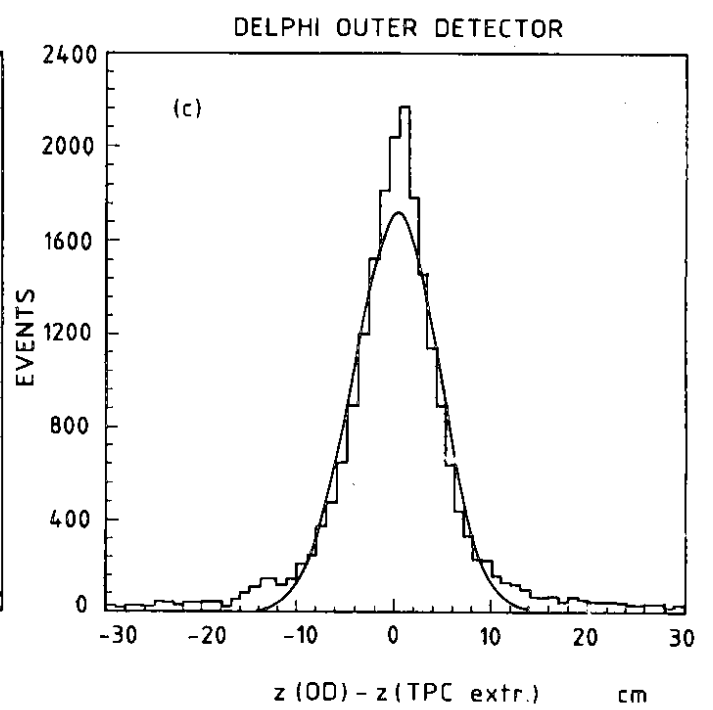
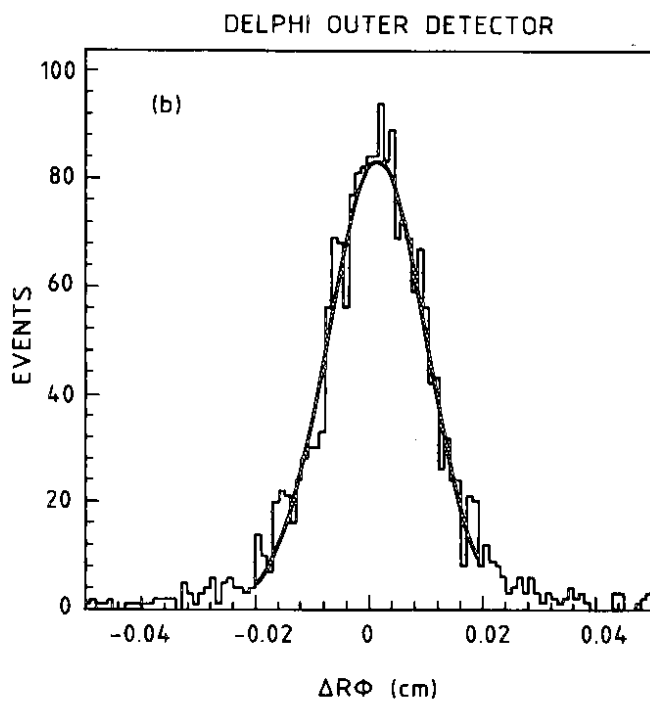
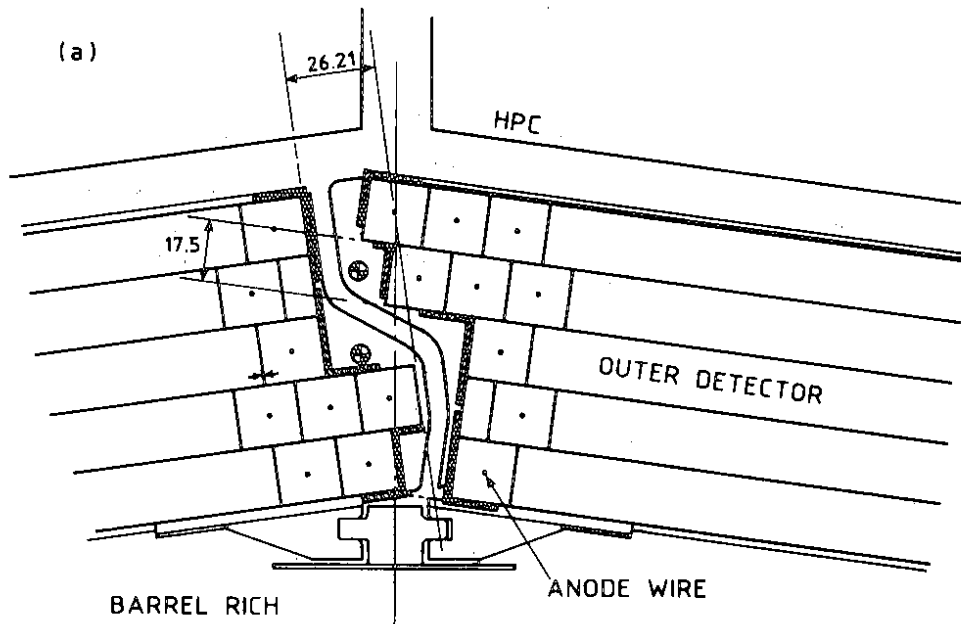


Fig. 12

# DELPHI BARREL MUON CHAMBERS

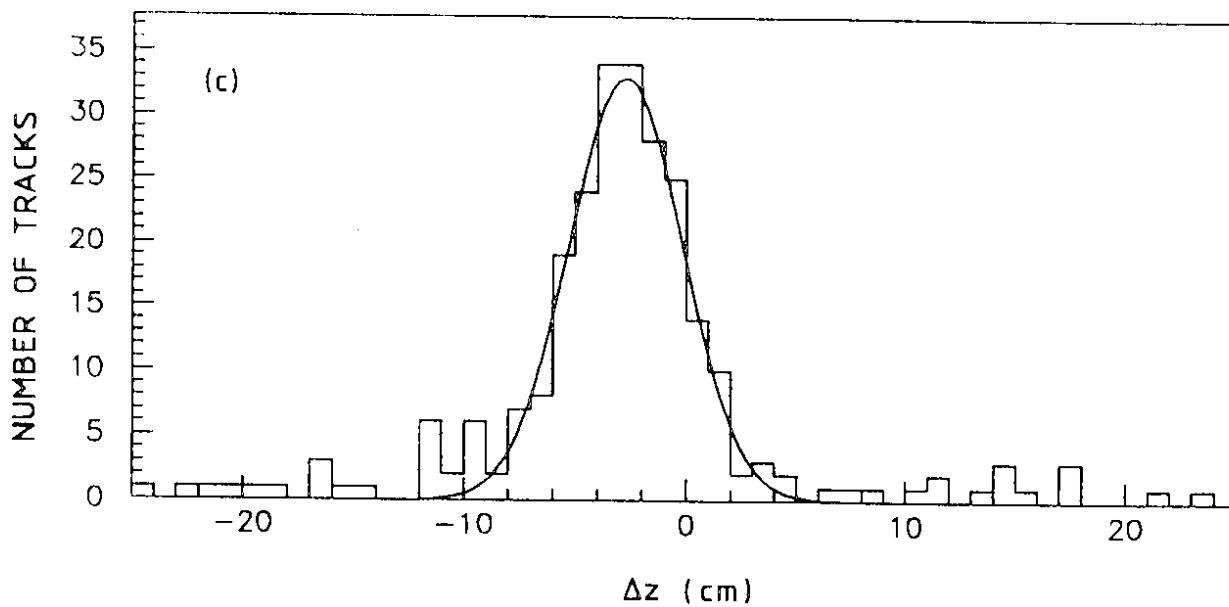
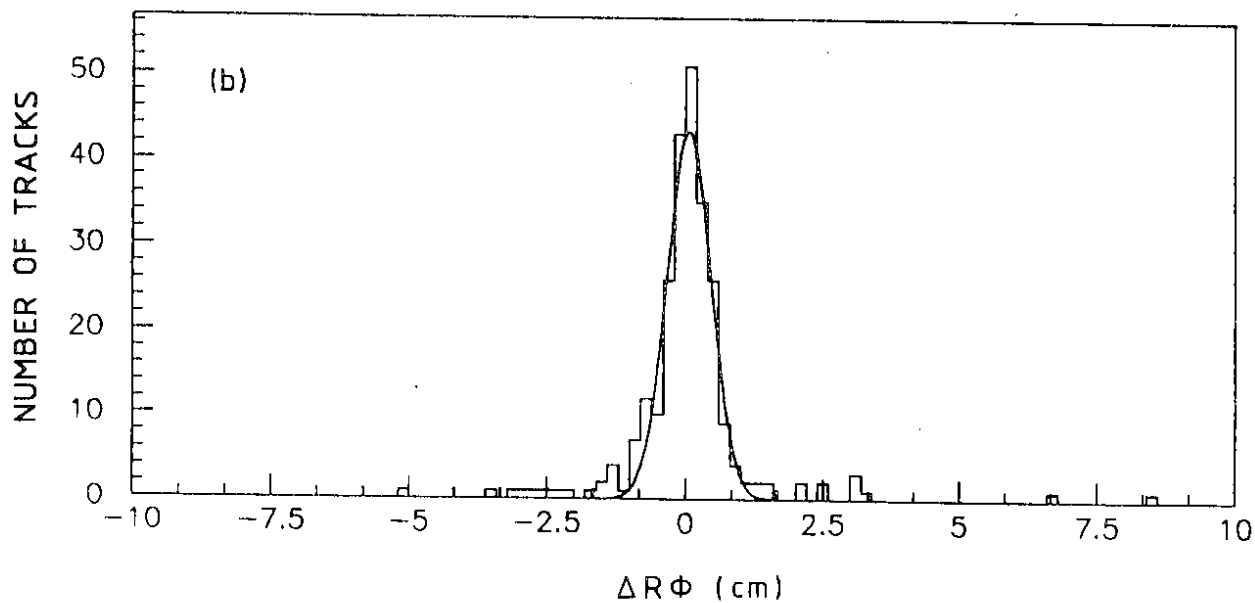
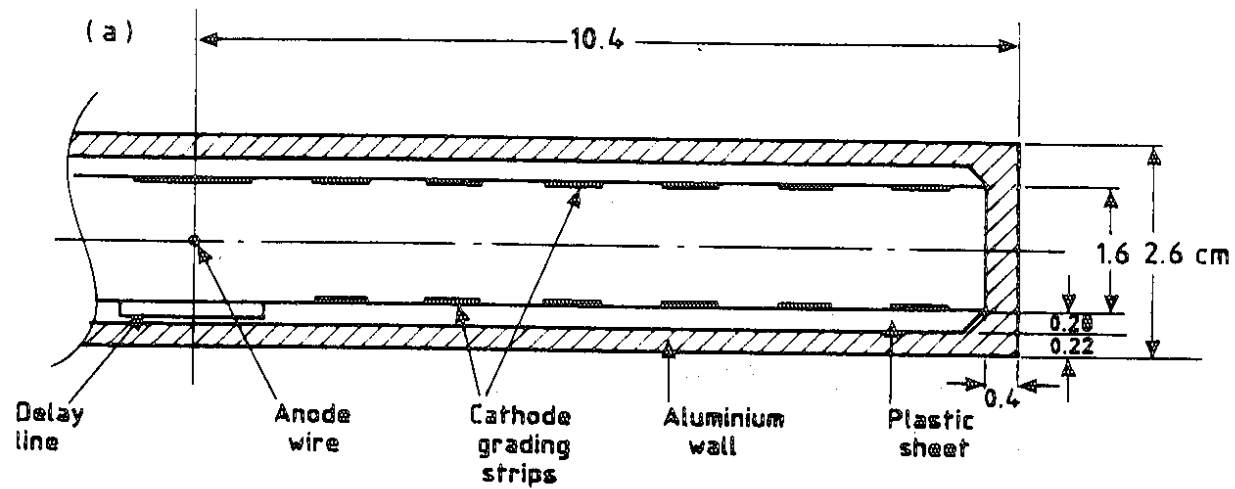


Fig. 13

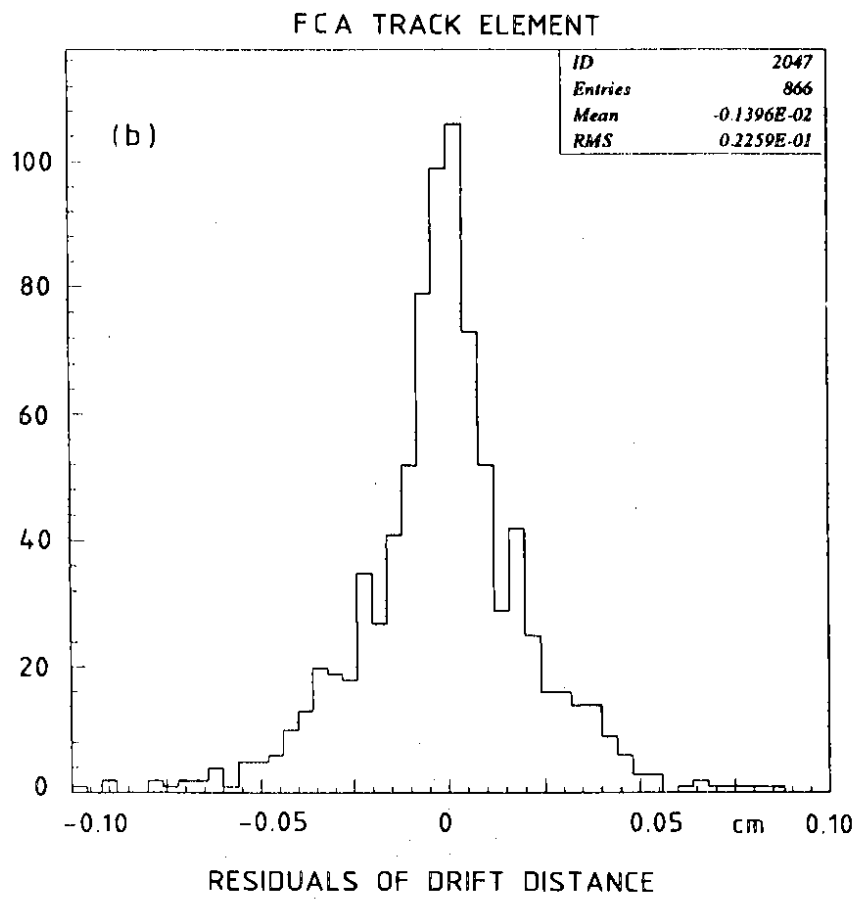
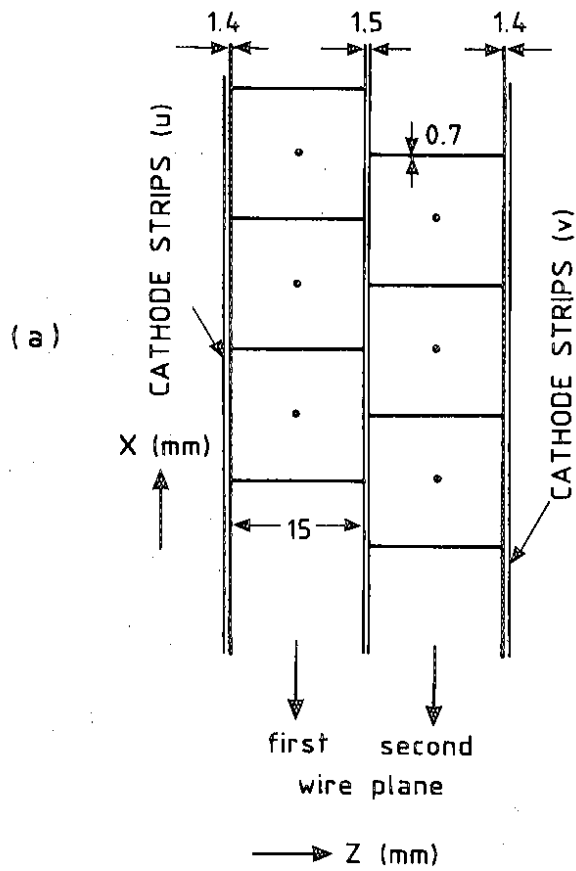


Fig. 14

# FORWARD CHAMBER B

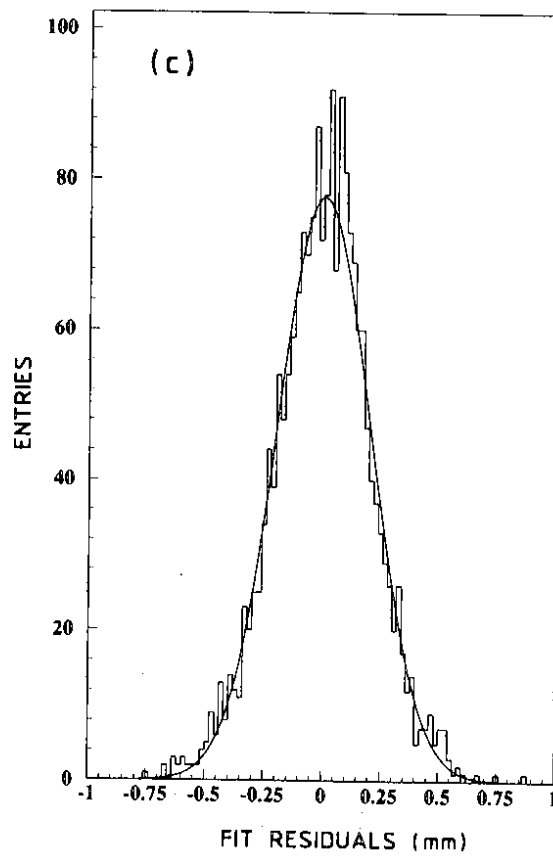
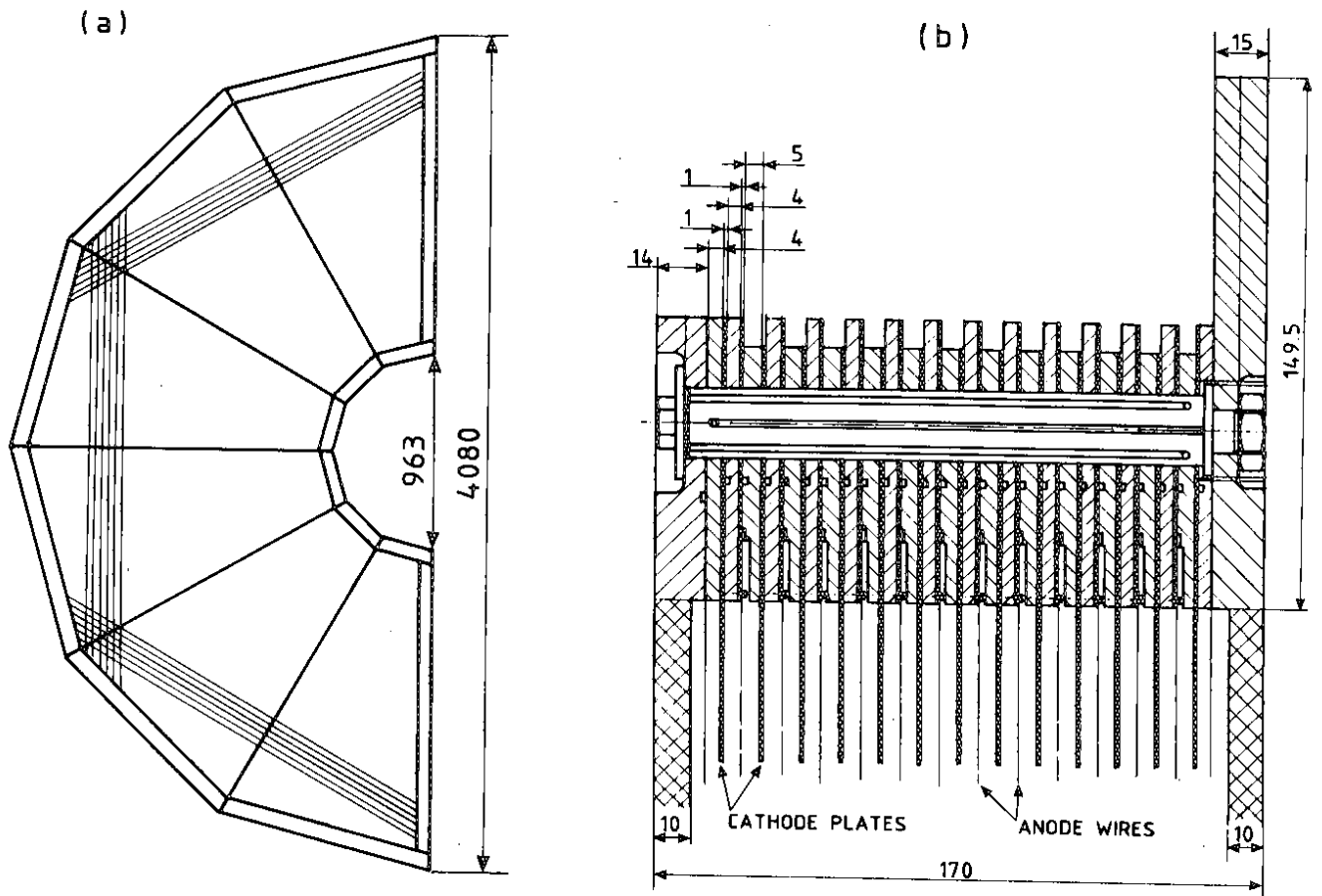


Fig. 15

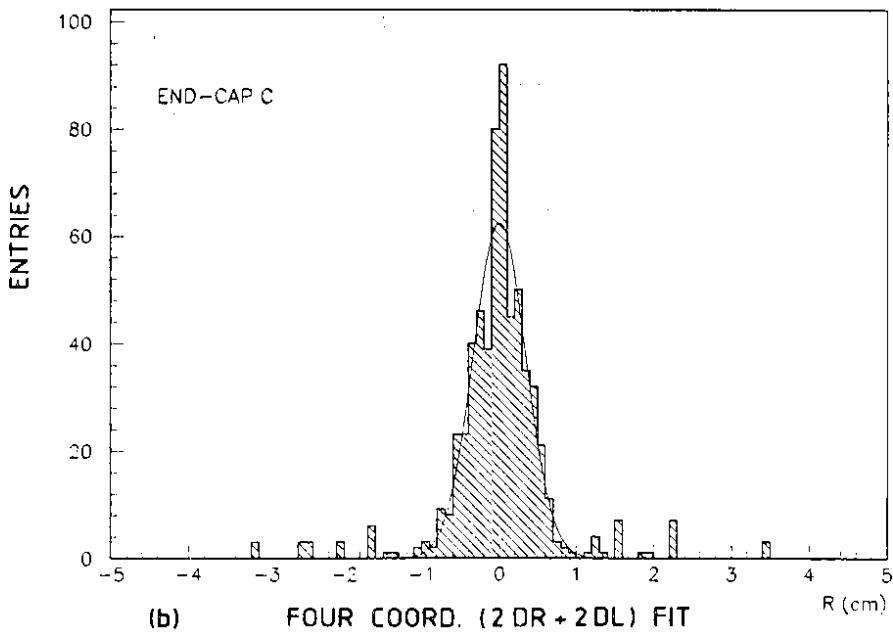
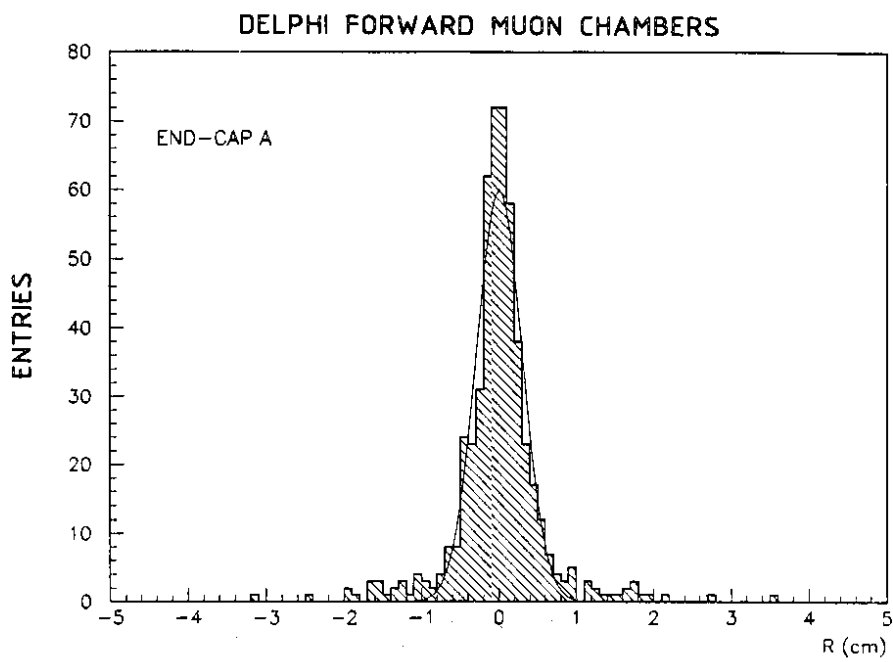
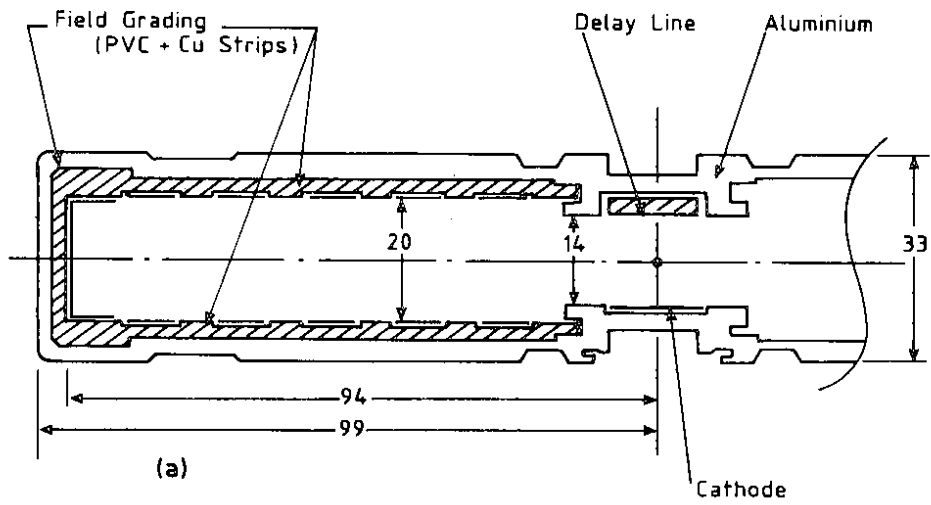


Fig. 16

# SAT TRACKER

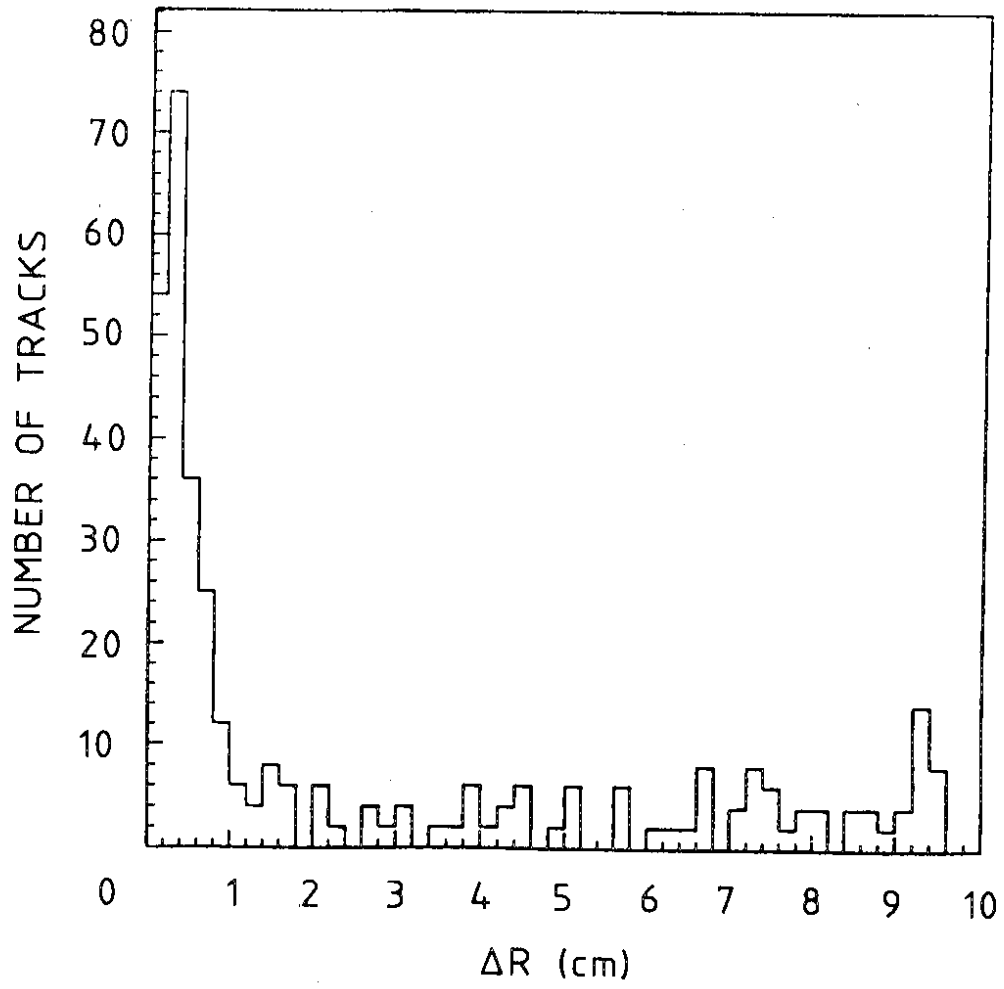


Fig. 17



DELPHI COMBINED TRACKING ( $\mu\mu$ )

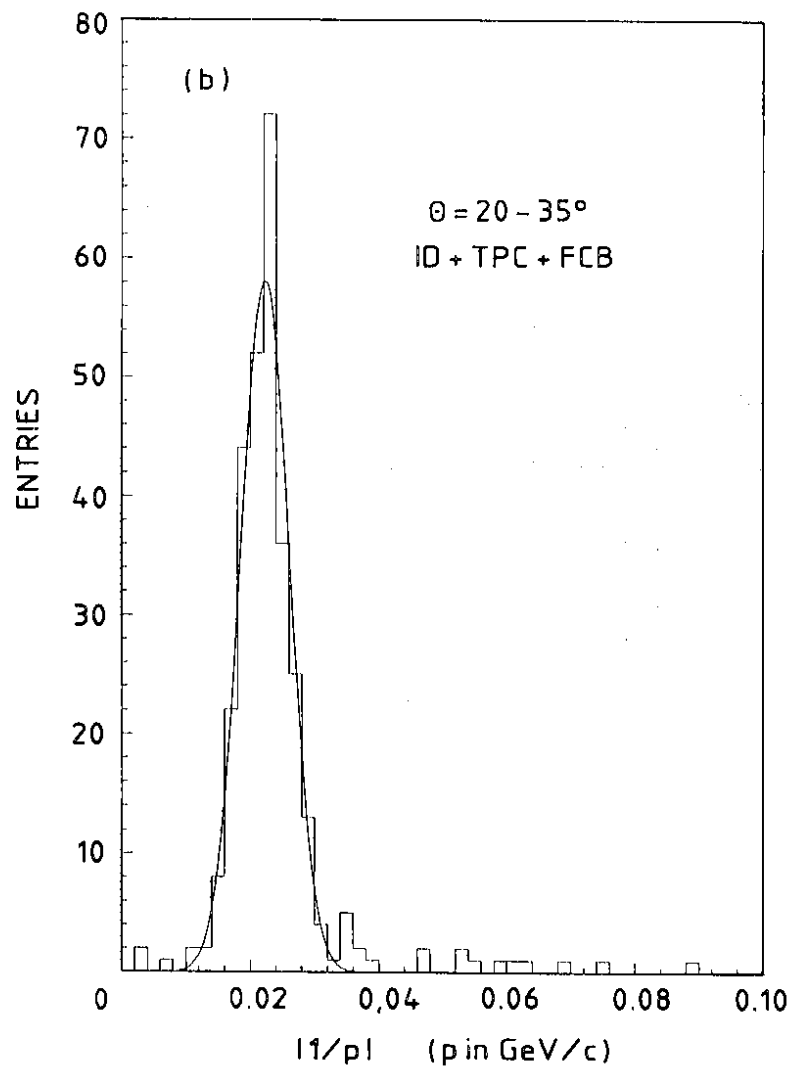
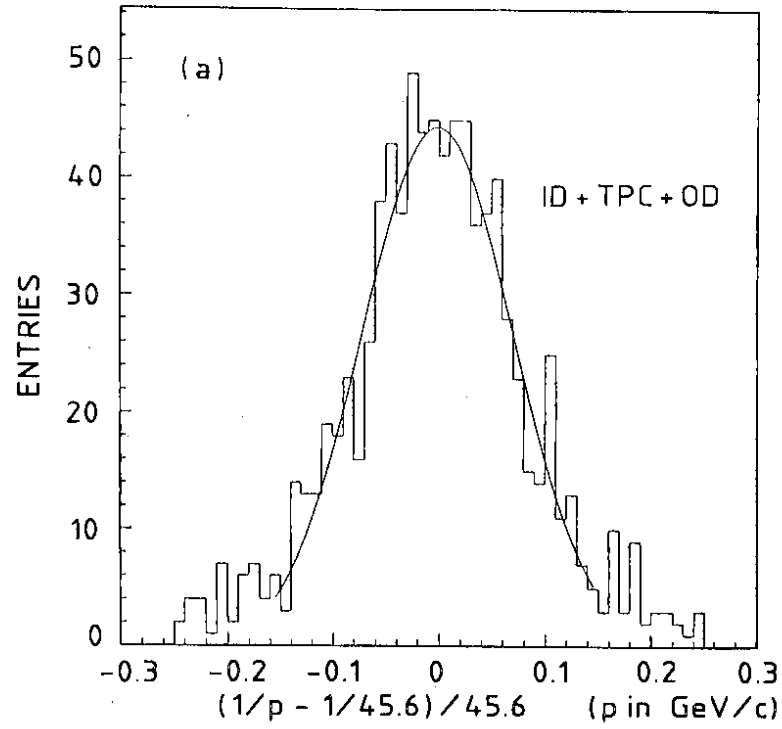


Fig. 18

# BARREL - SCINTILLATOR COUNTER (TOF)

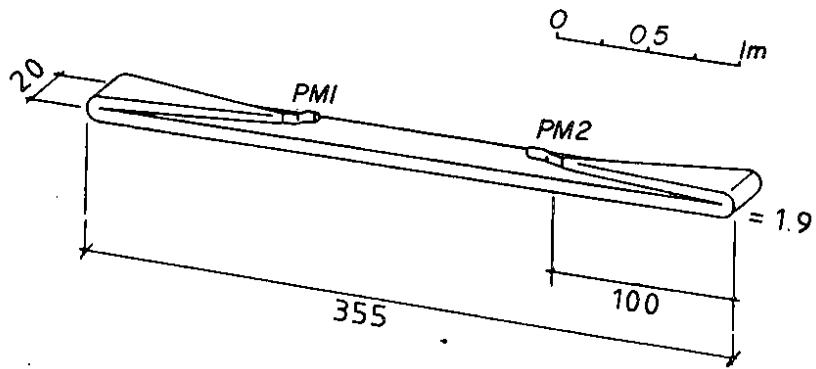


Fig. 19

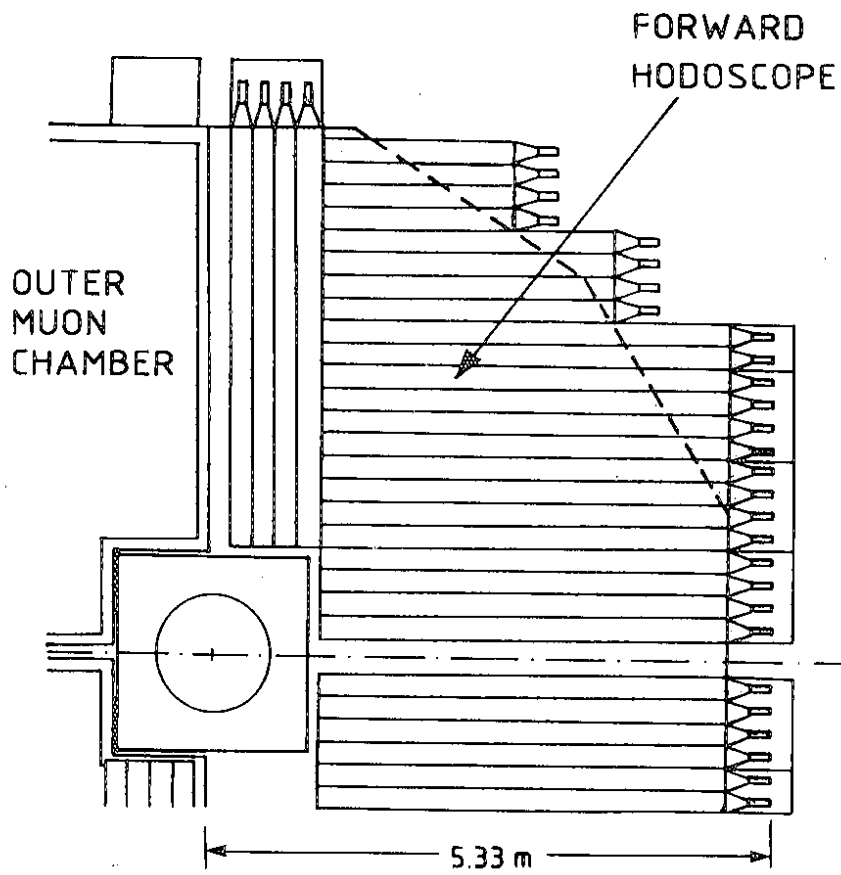


Fig. 20

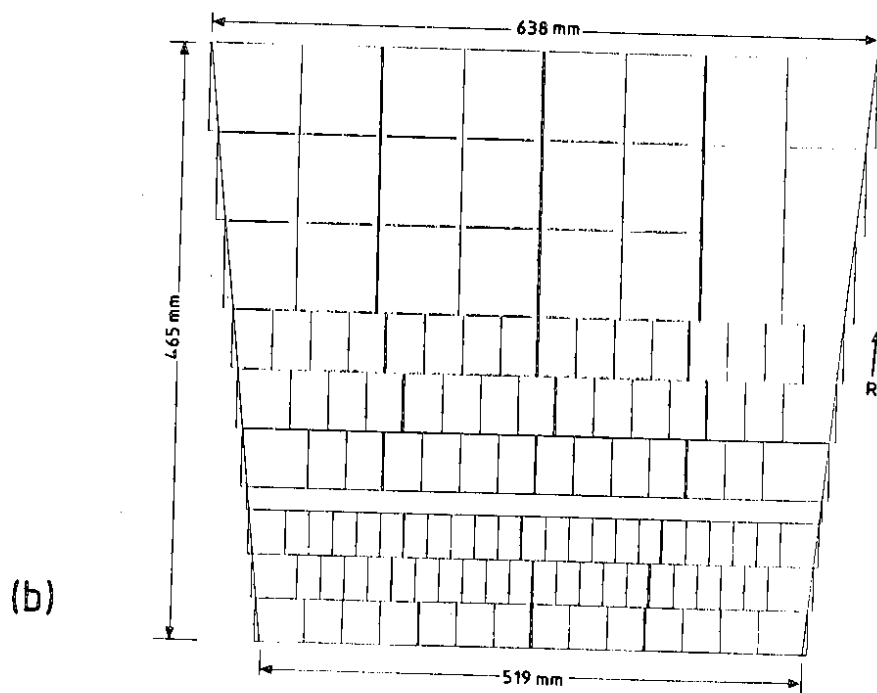
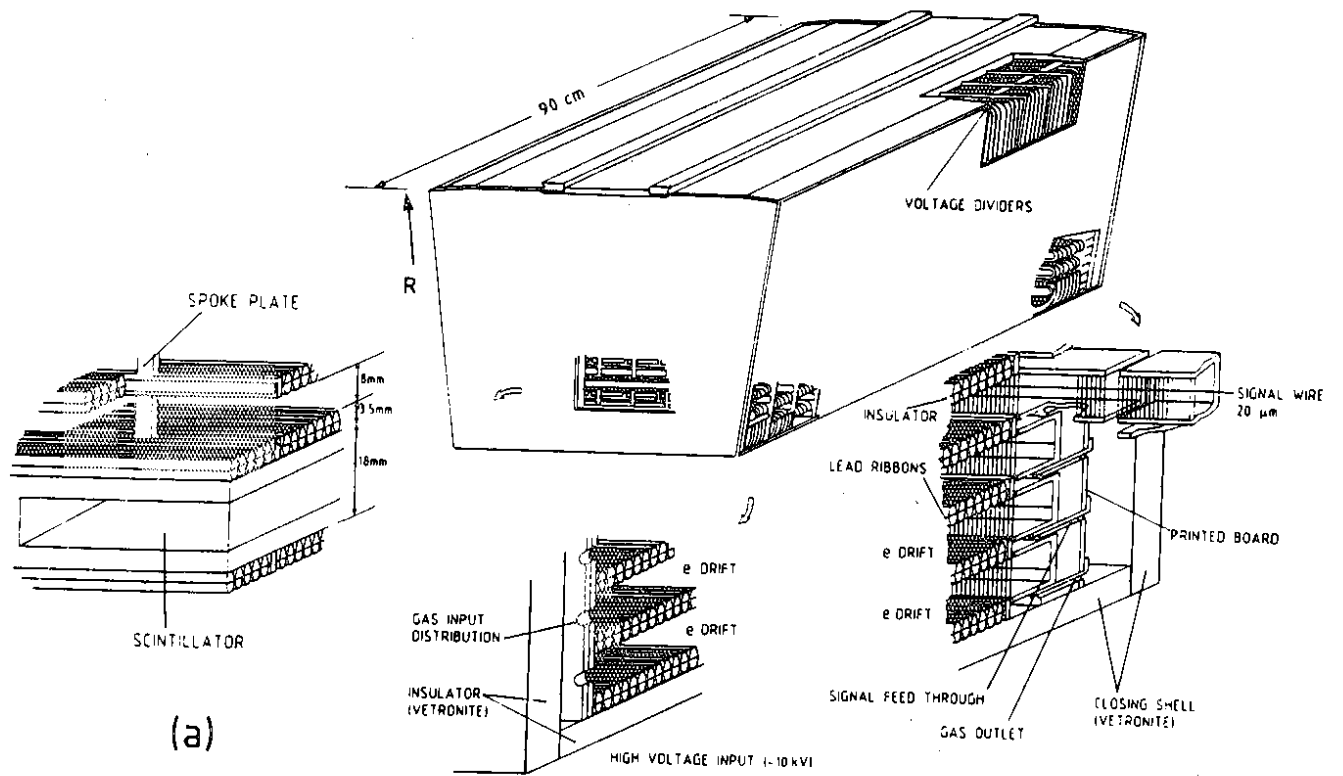
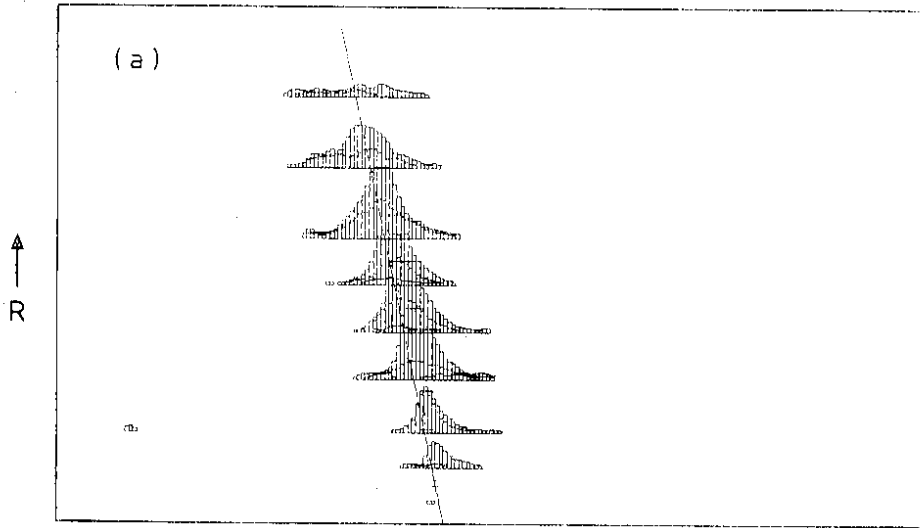


Fig. 21

HPC



DRIFT TIME (Z)

HPC

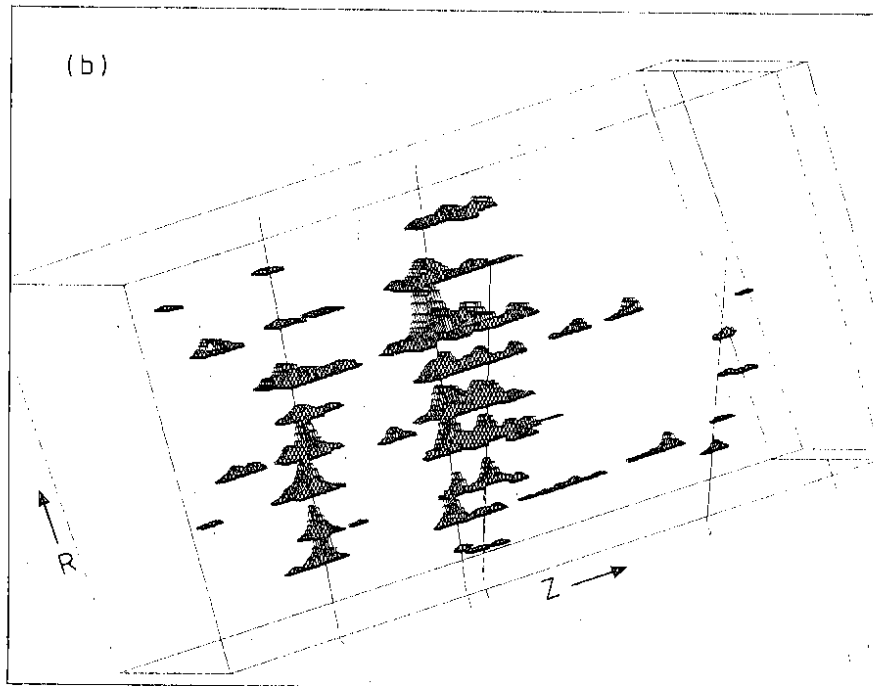
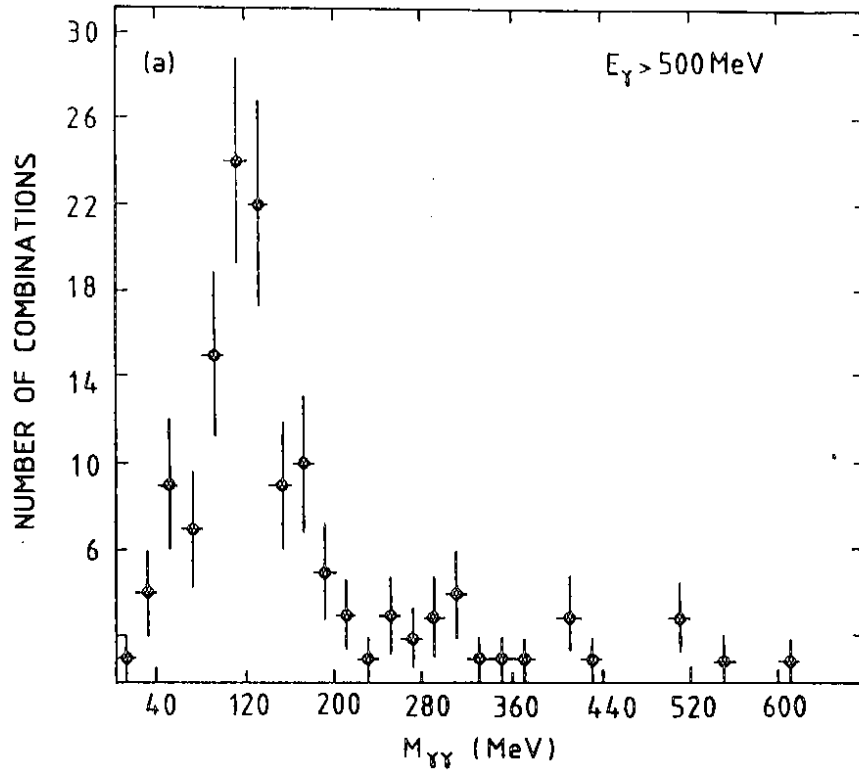


Fig. 22

DELPHI HPC



DELPHI HPC

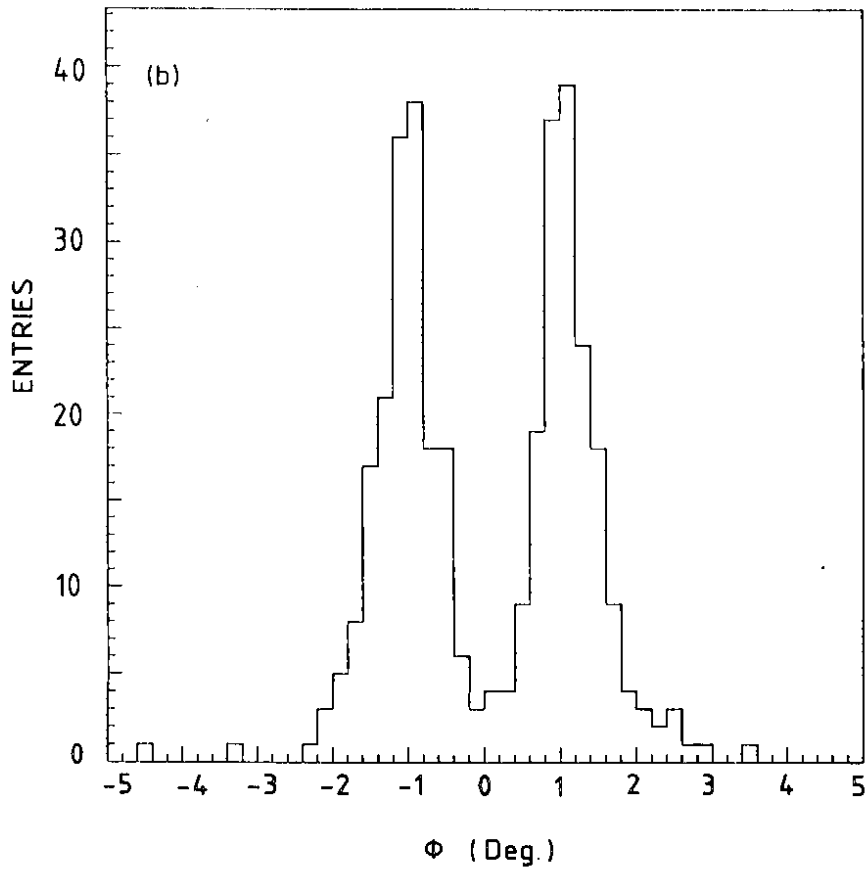
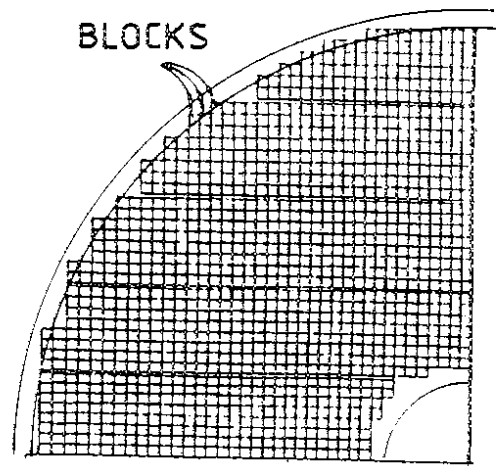
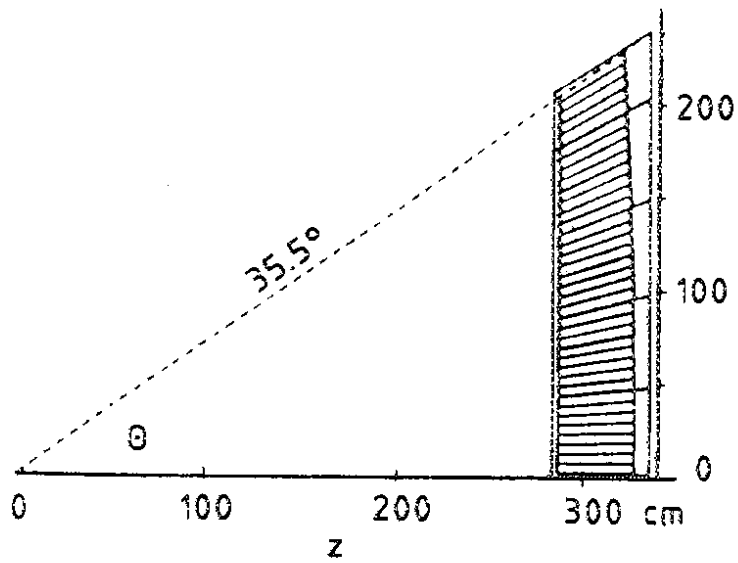
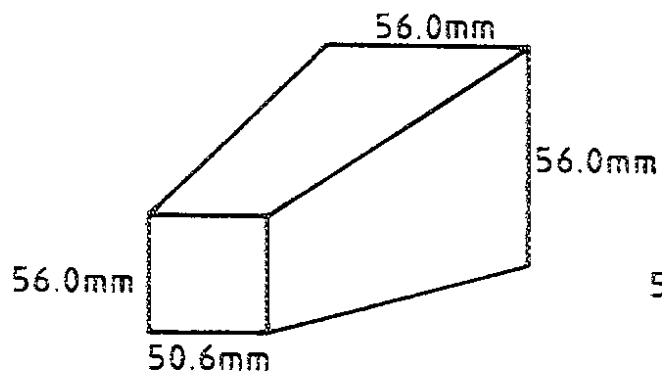


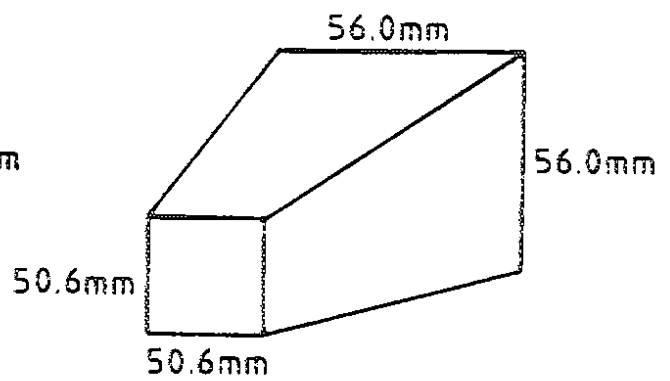
Fig. 23



TYPE 1



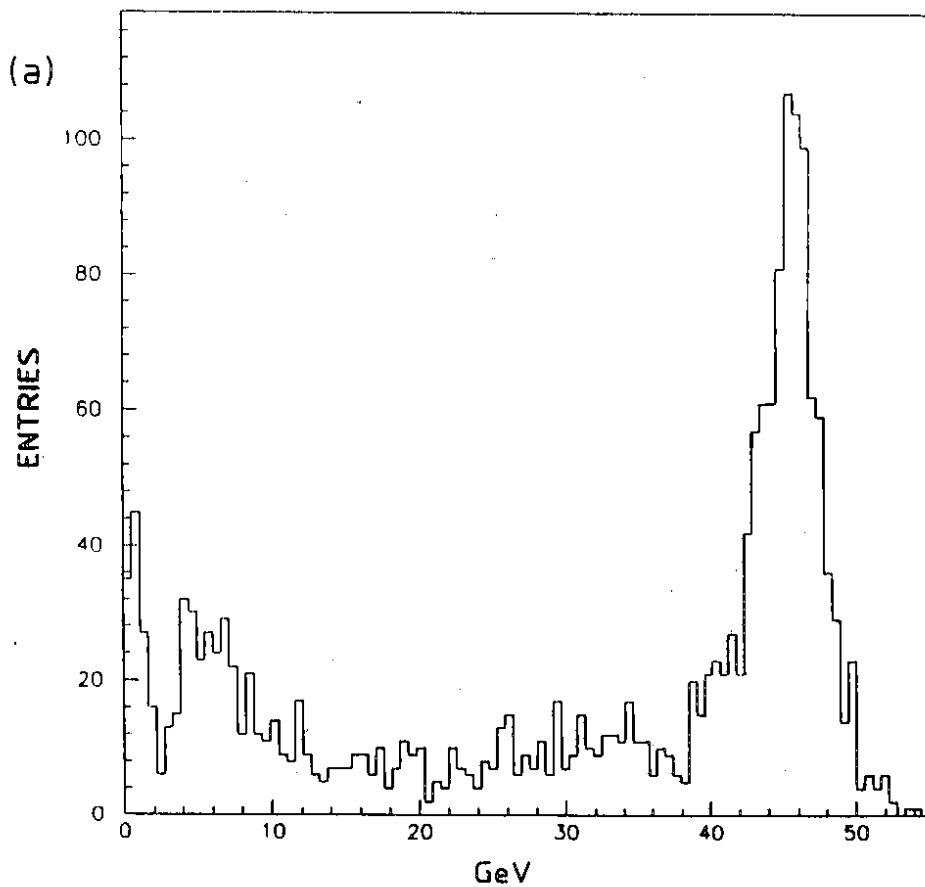
TYPE 2



LEAD GLASS BLOCKS

Fig. 24

DELPHI F EMC



DELPHI F EMC

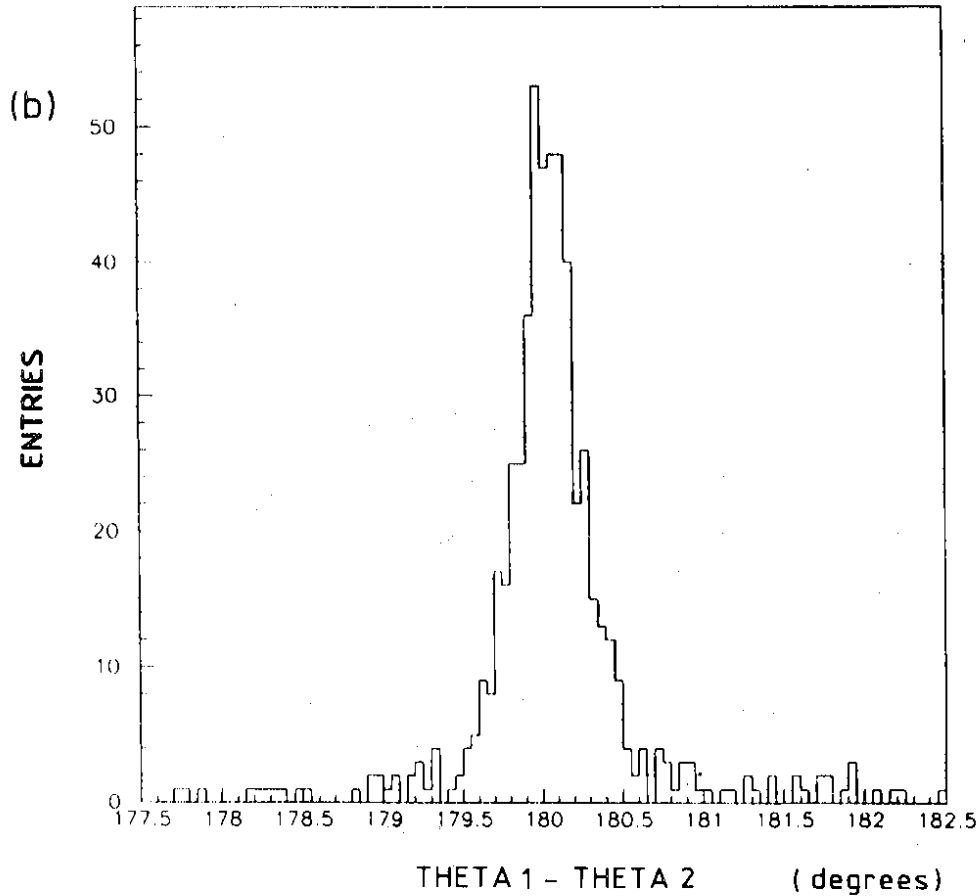


Fig. 25

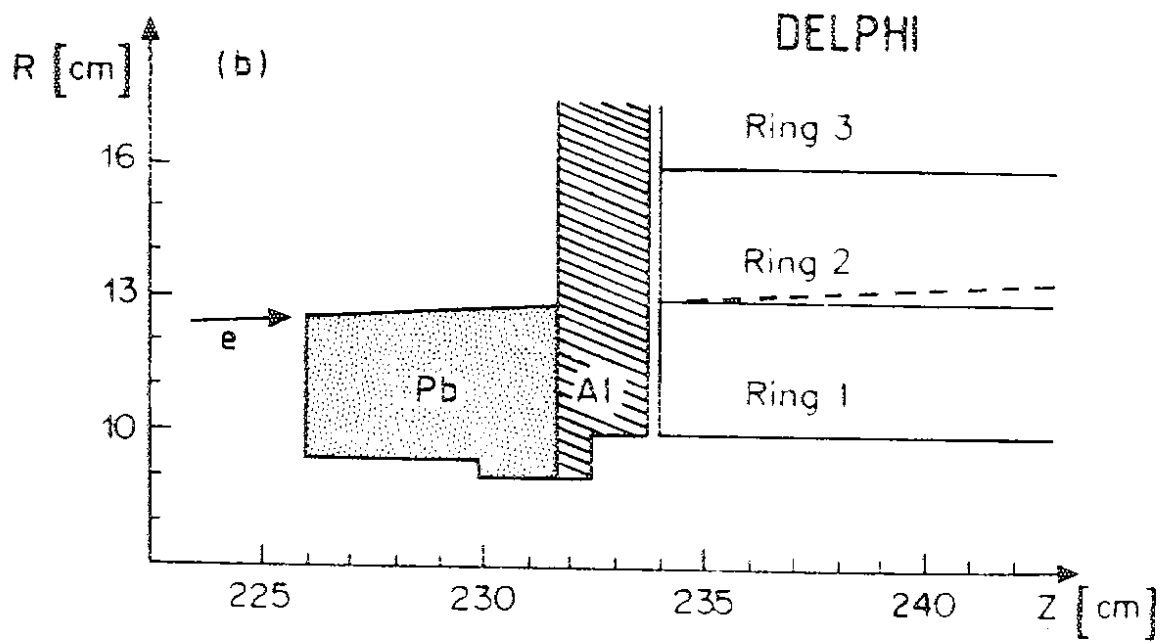
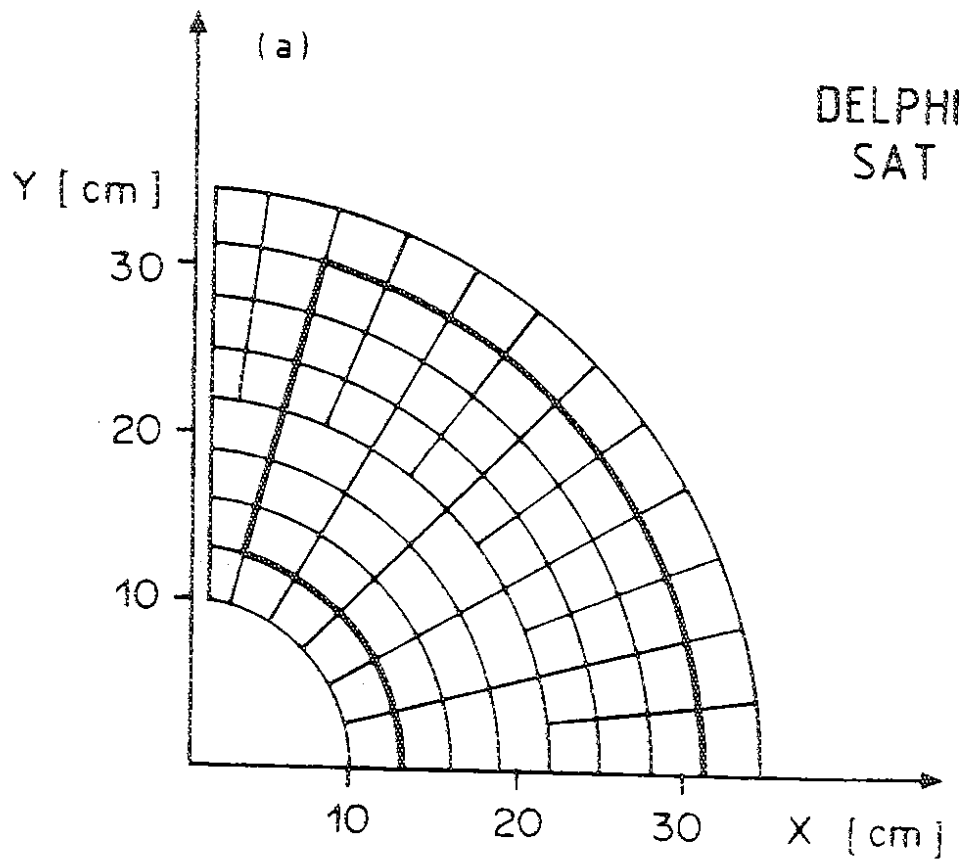


Fig. 26



DELPHI SMALL ANGLE TAGGER

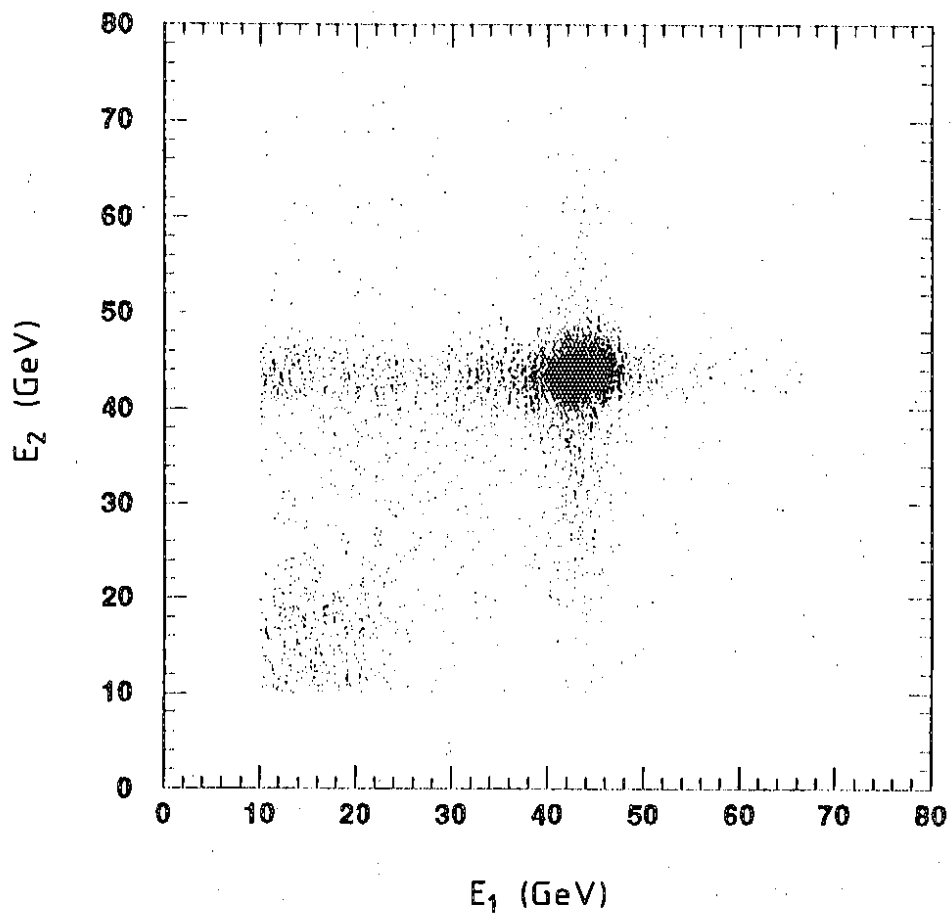


Fig. 27

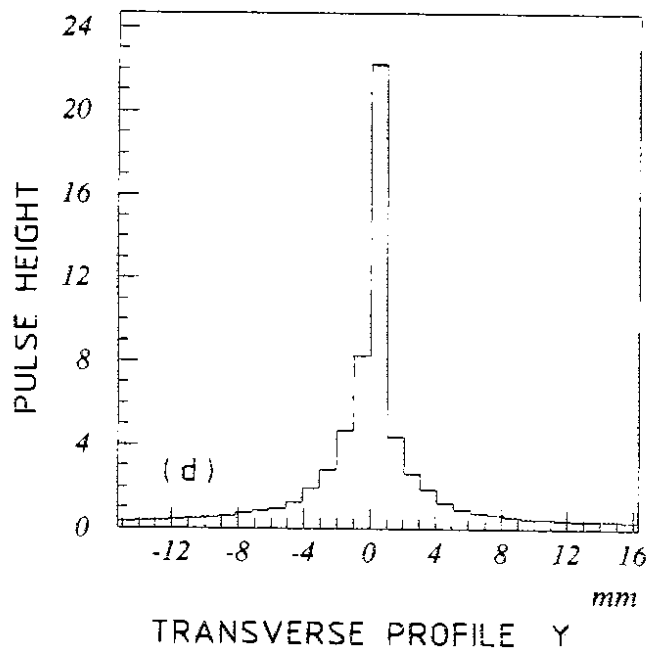
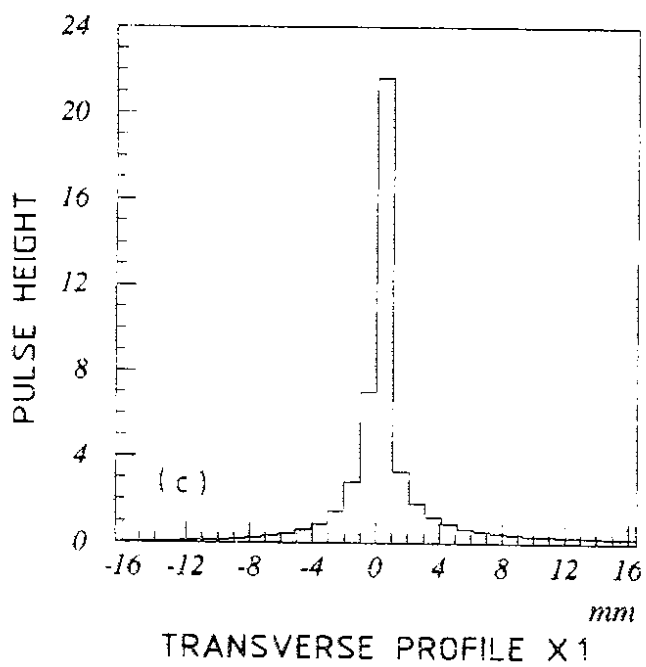
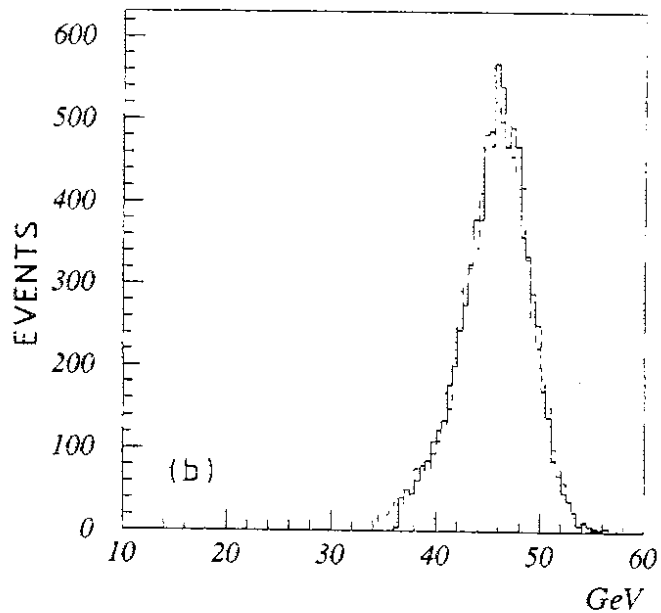
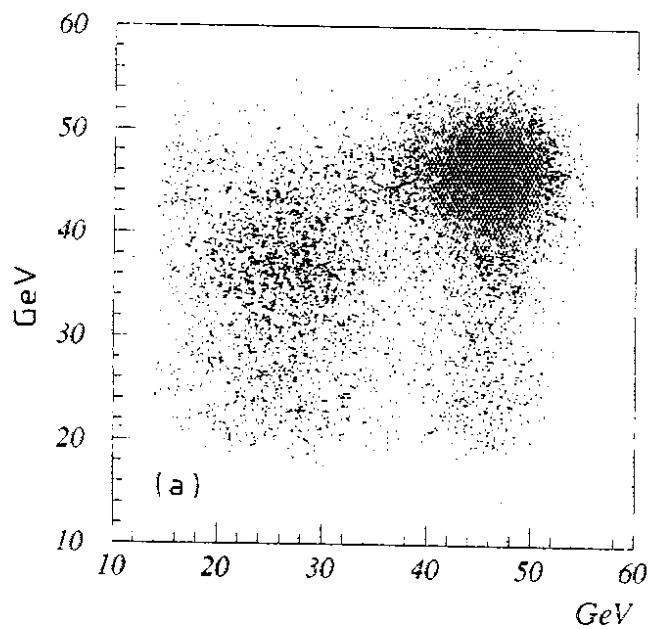


Fig. 28

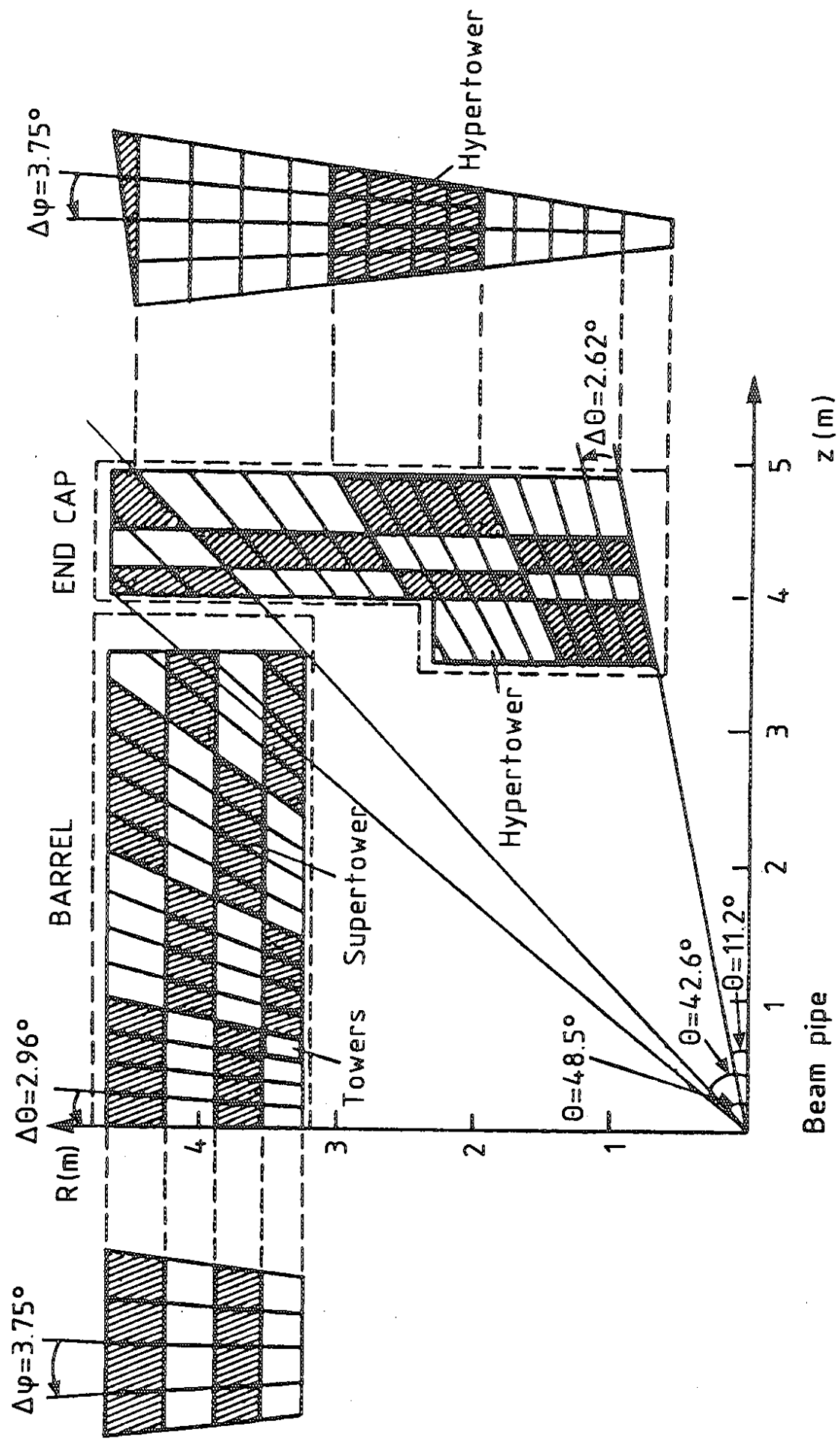


Fig. 29

# DELPHI HCAL

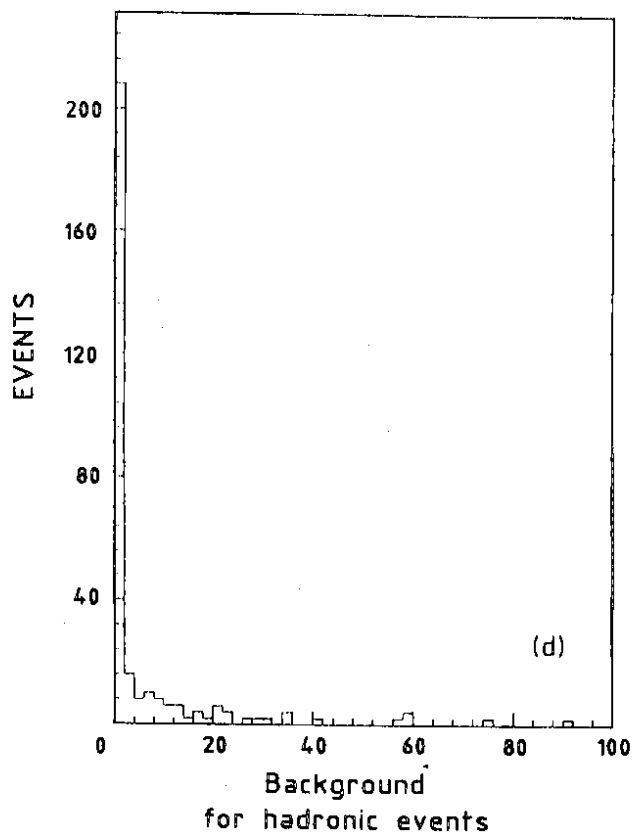
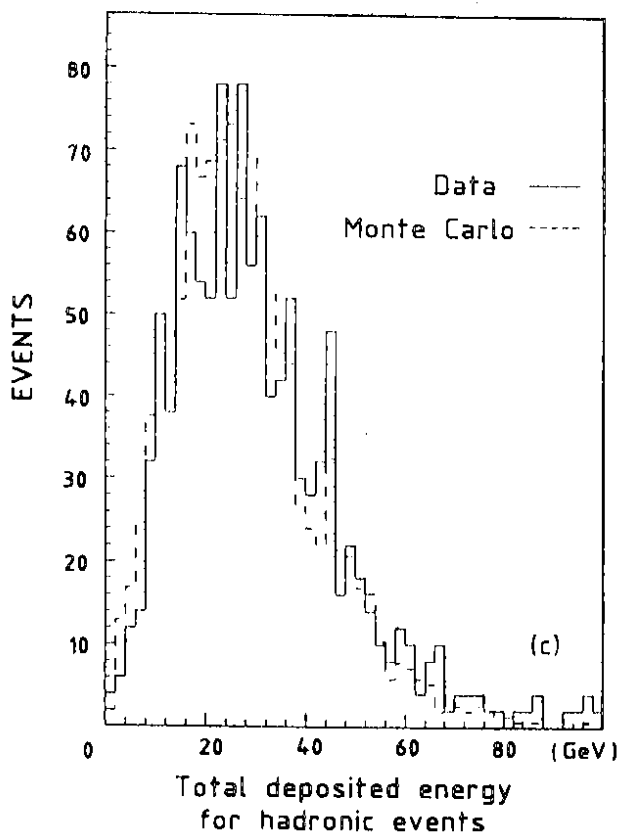
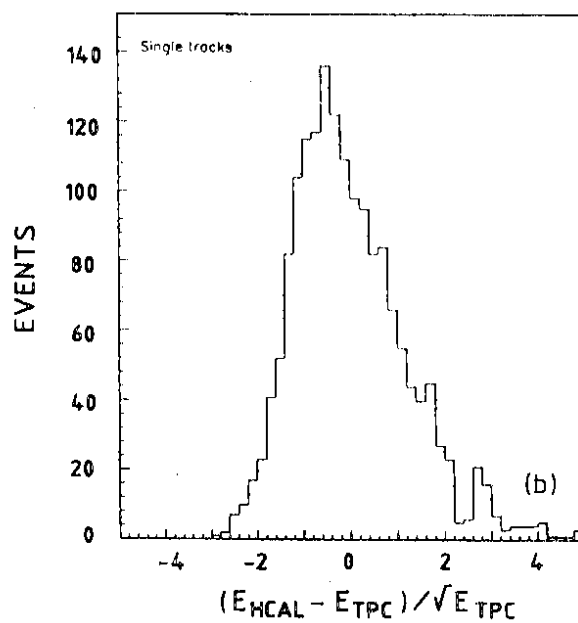
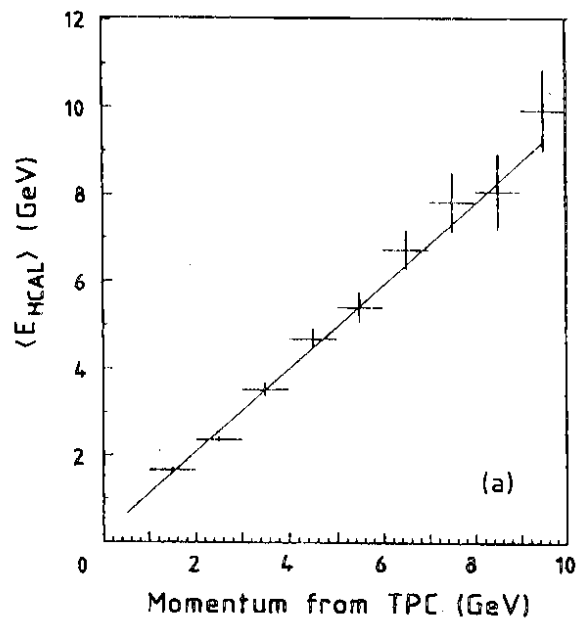


Fig. 30

# DELPHI BARREL-RICH

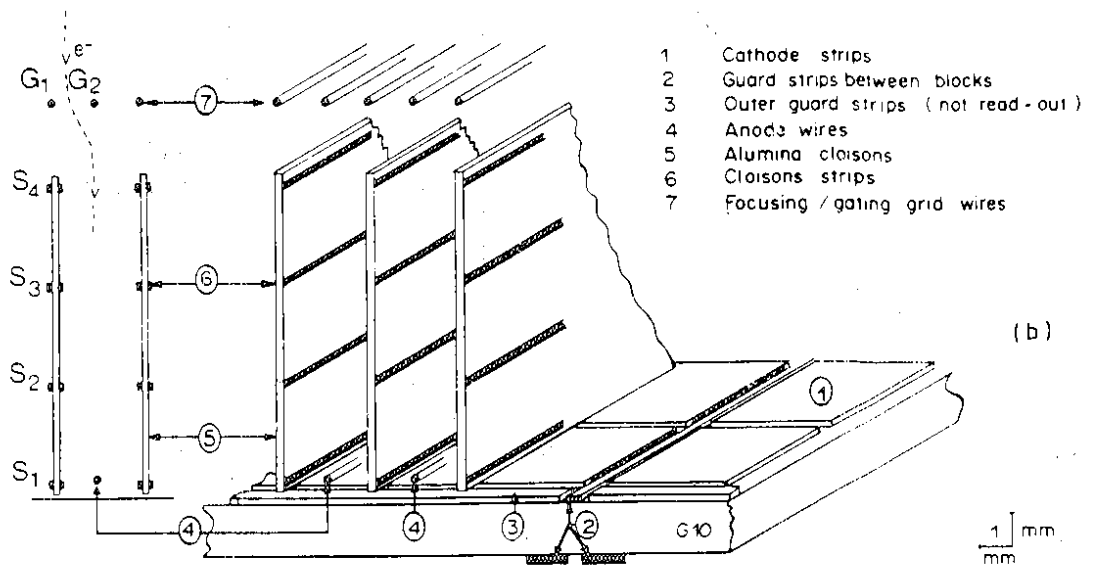
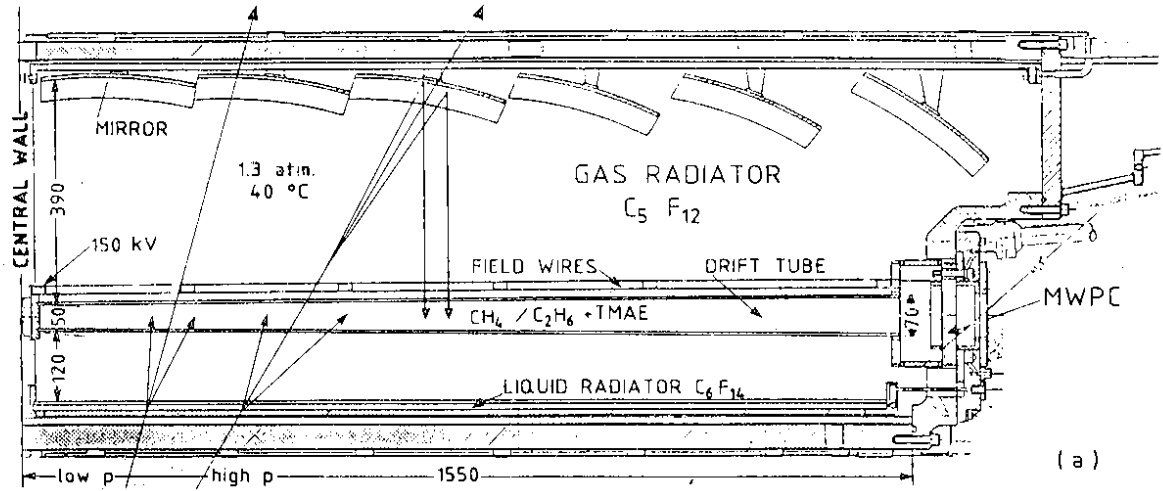


Fig. 31

DELPHI BARREL - RICH

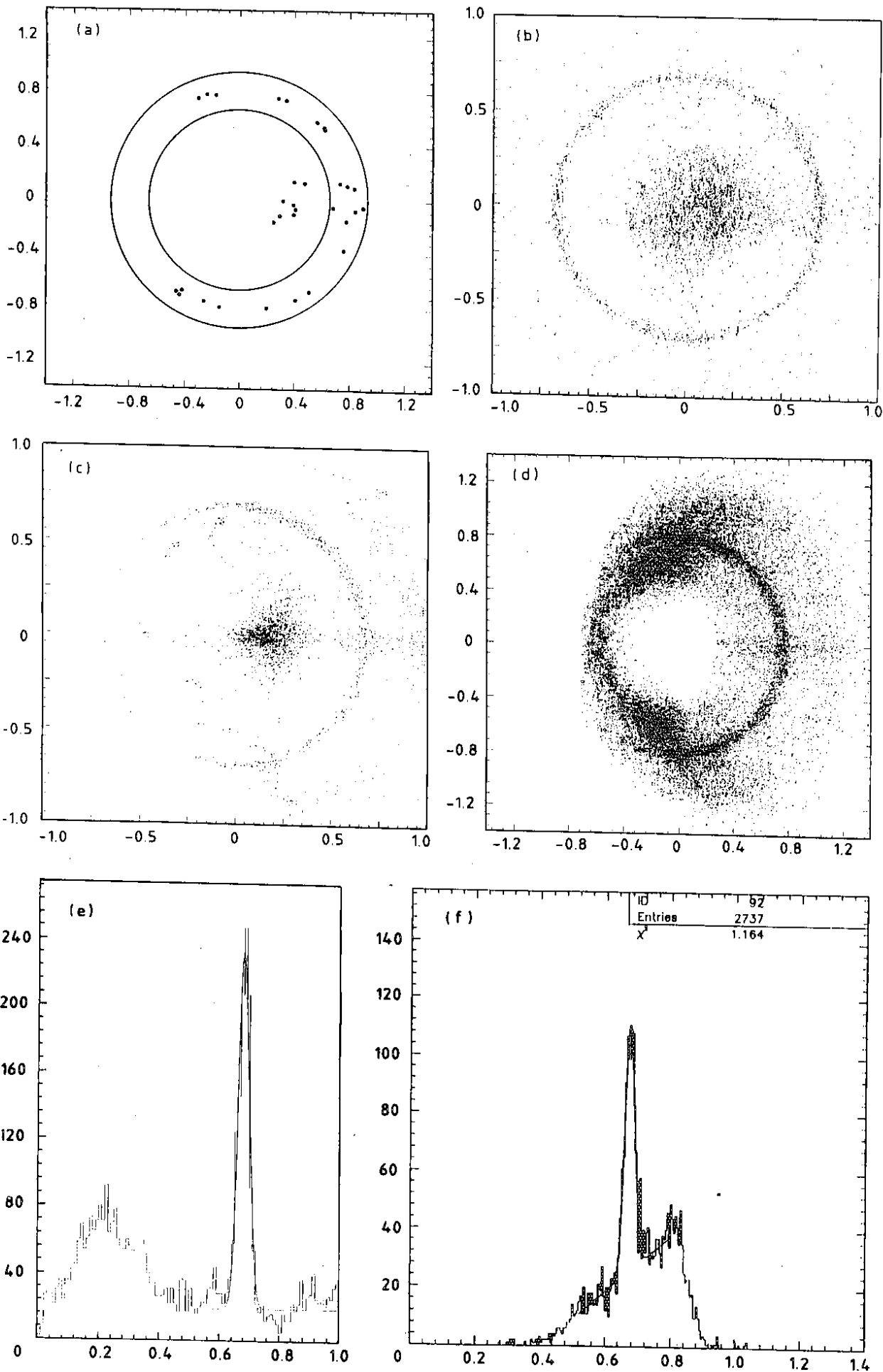


Fig. 32

# DELPHI FORWARD RICH

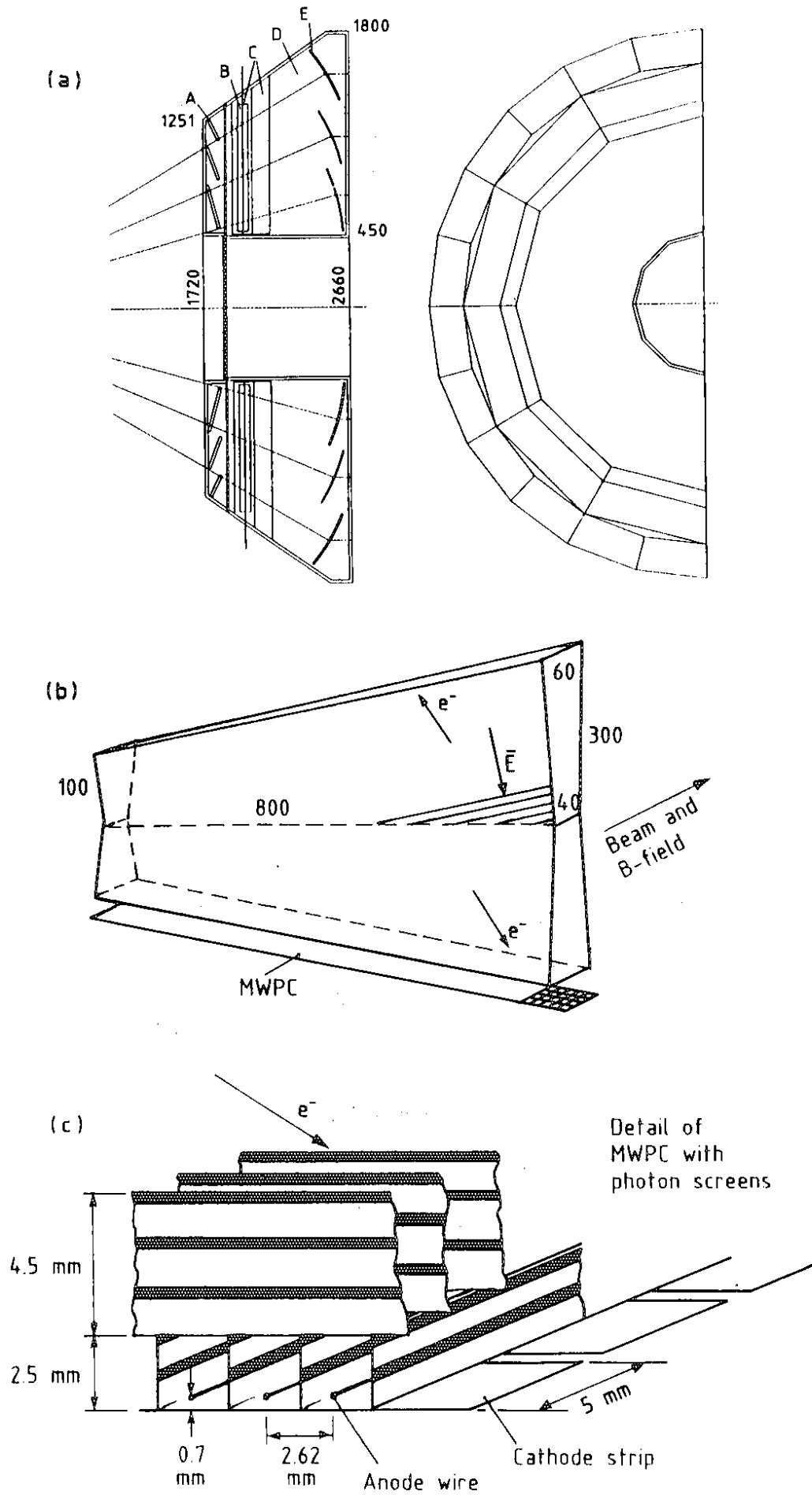


Fig. 33

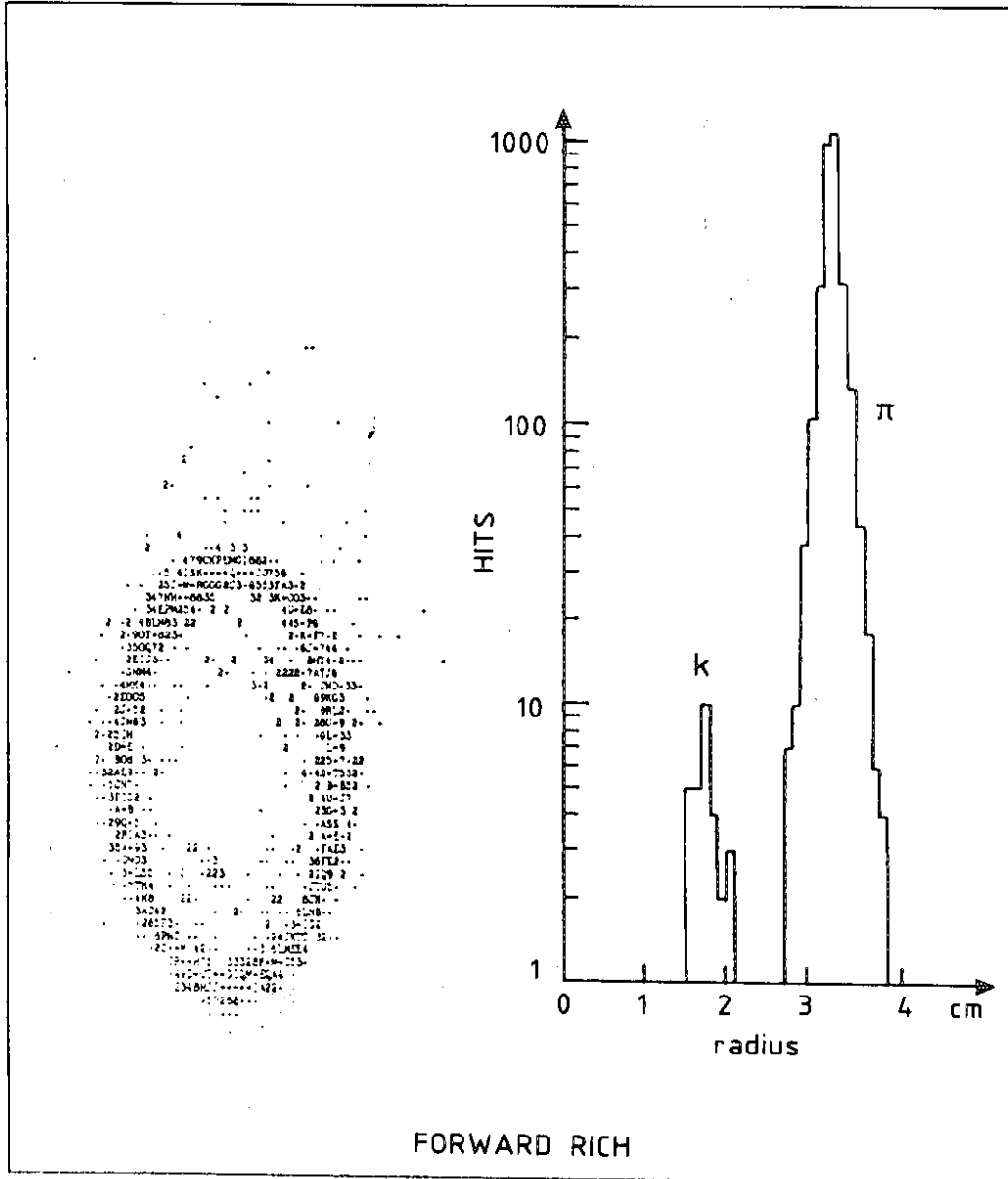
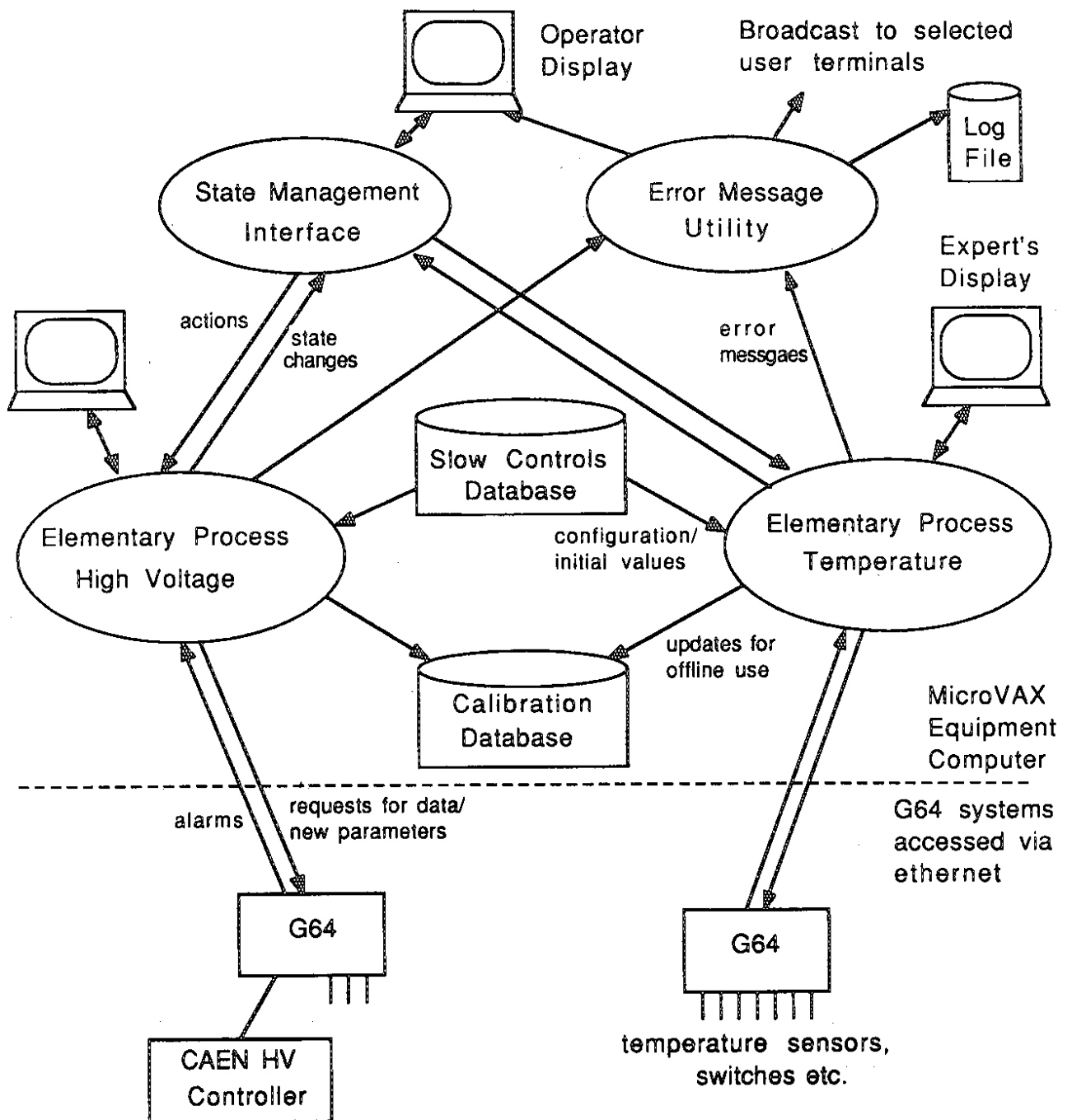


Fig. 34





DELPHI SLOW CONTROLS SYSTEM

Fig. 35

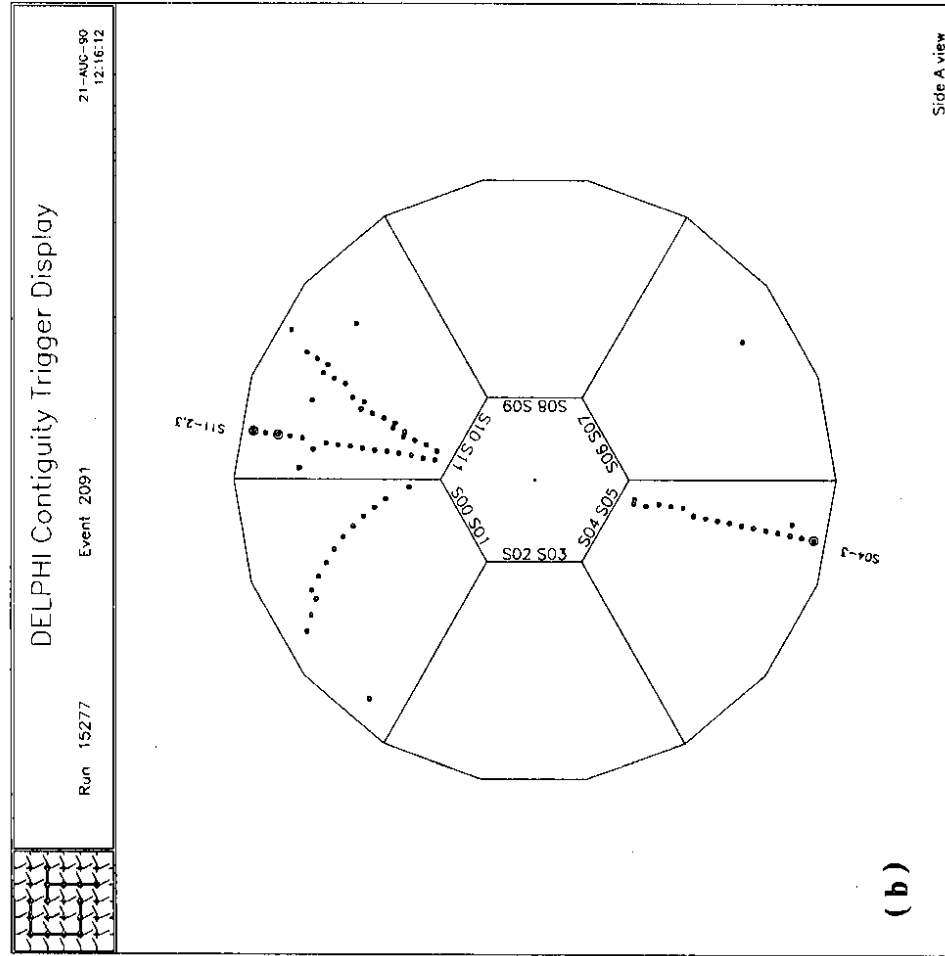
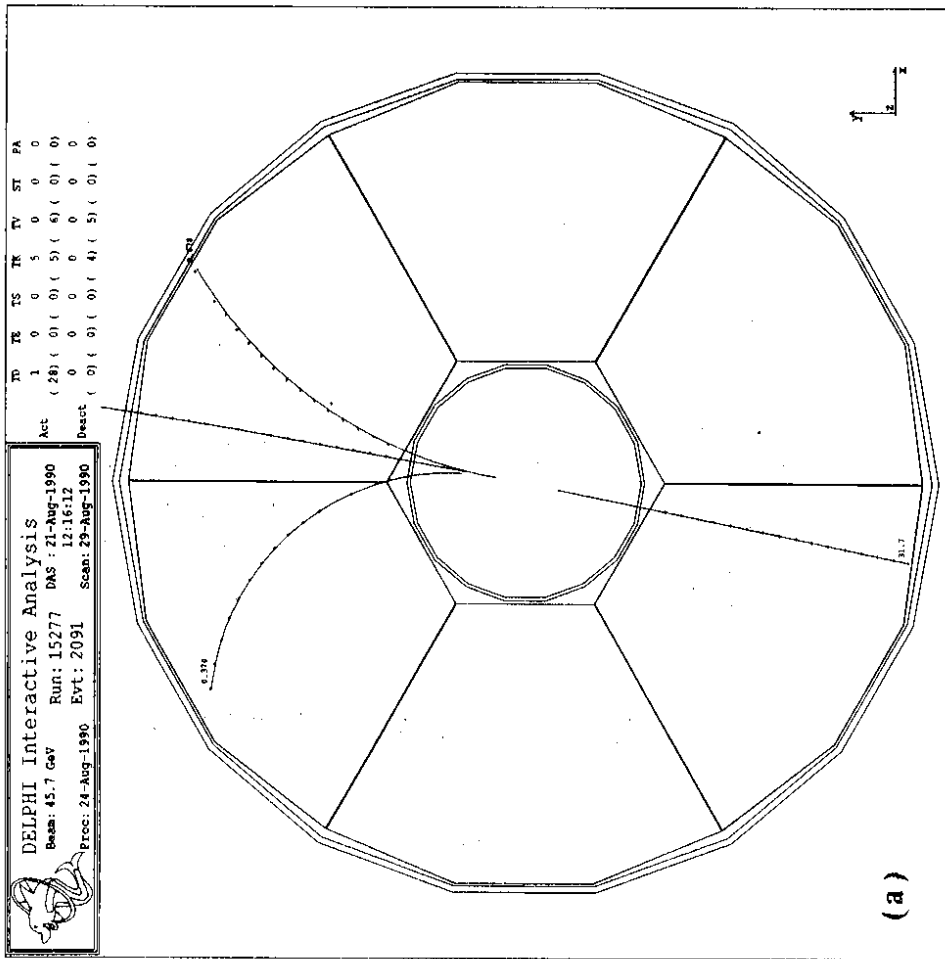


Fig. 36

# TRIGGER EFFICIENCY

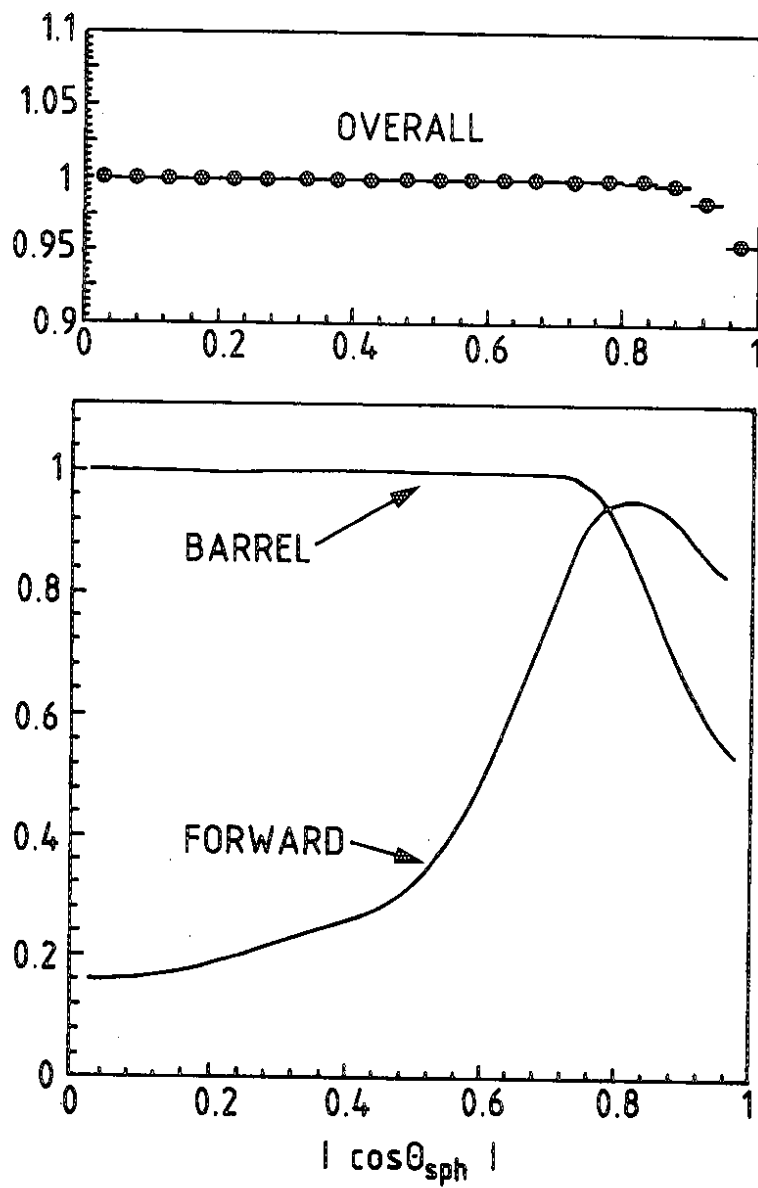


Fig. 37

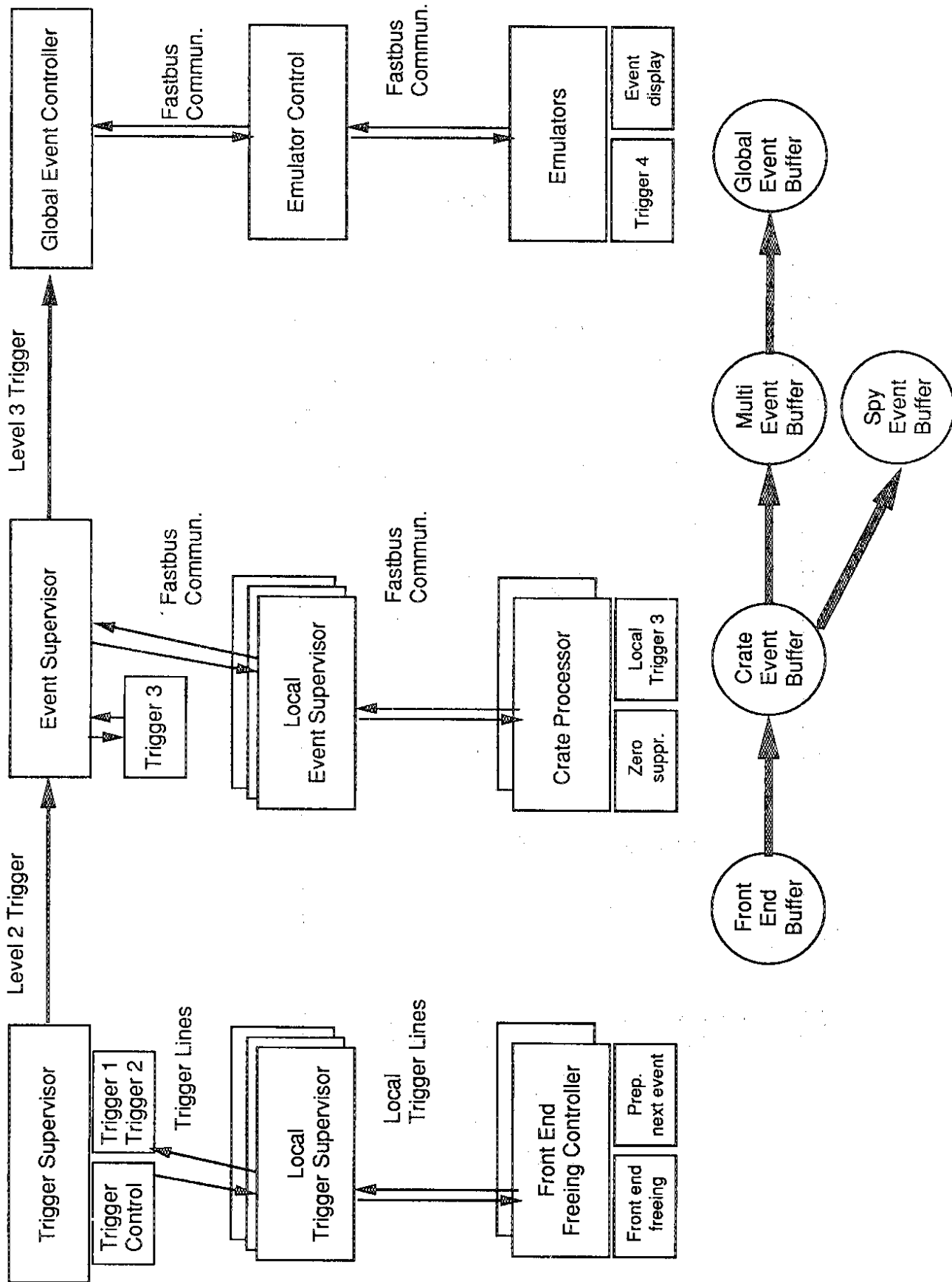


Fig. 38